Sede Amministrativa: Università degli Studi di Padova
Dipartimento di Fisica "Galileo Galilei"

Dottorato di Ricerca in Fisica

Ciclo XIII

A Run II Trigger Design for Higgs Boson Search at CDF

Coordinatore: Ch.mo Prof. Attilio Stella

Supervisore: Ch.mo Prof. Giovanni Busetto

Dottorando: Dott. Mario Paolo Giordani

31 dicembre 2000

A Run II Trigger Design for Higgs Boson Search at CDF

Mario Paolo Giordani

31 dicembre 2000

Acknowledgements

The first person I would like to thank is Patrizia, for all the support she has given me during the last year of my work; not only that: to her I owe much of the experience I have now achieved on particle physics analysis (and on Scotch whiskies).

I would also thank all members of the CDF Padova group and, in particular, Matteo, who helped me moving my first steps in the tangle of the CDF software (not only that, actually), Nicola, for his 'fatherly' presence, Giovanni, my supervisor, whose experience I have not profited enough (but – who knows – tomorrow is another day...), and Tommaso, for the useful physics discussions.

I need to thank three friends of mine: Cristiano, my *alter ego*, Gian Carlo, with whom I shared many nights at the Department of Physics of Padova in the attempt of completing our Ph.D. theses, and Pietro, my trusted theoretician.

Special mention to Sergio e Marisa, my parents, whose support, in good and bad times, has proven to be once more invaluable.

And remembering the past three years, I cannot forget two really special persons: Bruna, my grandmother, who would still be my fondest fan; in fact I am sure she still is. And Monica (how could I forget you?), whose love and patience I hope I will be able to reciprocate. This thesis is dedicated to them.

A final consideration: was Eric Clapton thinking of the multijet Higgs while writing the lyrics *"Sad, so sad, there is no easy way round..."*?

Contents

Introduction

The work described in this thesis has to be considered within the framework of Run II, the new phase that FERMILAB and CDF are about to start. One of the main goals for this new period of data taking is the search for the Higgs boson, whose existence would provide an answer to the problem of introducing fermion and boson masses in the Standard Model; conversely, its exclusion would open new frontiers in both theoretical and experimental physics (**Chapter 1**).

During the last few years, TEVATRON and CDF have undergone major upgrades (**Chapter 2**) aimed at increasing sensitivity with respect to signals whose statistical relevance is seriously endangered by the presence of many competing processes, often characterized by orders of magnitude larger cross sections.

This introduces the necessity of controlling data acquisition by means of a trigger system, *id est* a processor capable of selecting only events which present the characteristic signatures of interesting processes; detector and accelerator upgrades required the redesign of many trigger components, allowing, at the same time, the definition of new trigger primitives (**Chapter 3**).

Trigger efficiency and rate rejection are essential features for studying processes characterized by a limited cross section, such as in the case of the Higgs boson production. Although at $\sqrt{s} = 2$ TeV Higgs production is dominated by gluon fusion, the associated production with a vector boson is a much more promising channel to study, since the vector boson reconstruction provides effective handles to control the QCD backgrounds. For light Higgs masses, the dominant decay channel leads to the production of a $b\overline{b}$ pair, while, from the experimental point of view, the most promising signatures correspond to the vector boson decaying leptonically, since high P_T leptons can provide a good trigger. In spite of their cleaner signatures, these channels are affected by a low branching ratio.

The goal of this work is the design of a trigger aimed at selecting the fully hadronic final states emerging from the decay of a Higgs boson produced in association with a vector boson (**Chapter 4**); this channel is characterized by a high branching ratio (47%), but suffers from high QCD backgrounds. The main signatures of this process are the heavy flavour content due to Higgs decay (but also vector bosons can contribute) and a multijet topology. While the latter can be exploited by means of suitable calorimetric requirements, the former needs some form of b-tagging. Two independent approaches can be followed: tagging the soft leptons (e or μ) produced in the $b \to \ell \nu_\ell X$ and $c \to \ell \nu_\ell X$ decays or identifying the secondary vertices that characterize heavy flavour decays. The first procedure relies on a well tested algorithm (SLT), which was developed during Run I for the offline $t\bar{t}$ analysis; its implementation at trigger level is the object of this thesis. The second procedure, on the other hand, searches for secondary vertices by identifying displaced tracks; this method (SVT), relying on the new silicon vertex detector, has been

designed for low multiplicity $b\bar{b}$ events and its performances in a dense environment are still being studied.

Finally, a characterization in terms of kinematics and heavy flavour content of the events collected by the SLT-multijet trigger is given (**Chapter 5**) in view of a future analysis.

Chapter 1

Theory and phenomenology of the Standard Model

In this chapter a brief review of the Standard Model (SM) focused onto the the problem of introducing masses for both vector bosons and fermions will be presented. This will introduce the issue of Higgs physics, which will be dealt with by a theoretical perspective aimed at describing in detail the Higgs mechanism and the alternatives proposed by the SM extensions; finally, the experimental results so far achieved by the searches devoted to the Higgs boson itself will be preceded by a phenomenological introduction which will review the dominant H^0 production processes at hadronic colliders and decay modes as predicted by the SM.

1.1 Introduction to the Standard Model

1.1.1 Towards a unified electroweak theory

The first approach to weak interactions finds its origins in 1934, when Fermi [1] proposed a theory able to account for the nuclear β-decay process (see fig. 1.1), which, in terms of partons, can be expressed as:

$$d \longrightarrow u + e^- + \overline{\nu}_e \ .$$

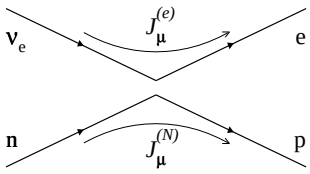

Figure 1.1: $n \to p e^- \overline{\nu}_e$

Driven from experimental observations, suggesting for weak decays longer lifetimes than in electromagnetic processes, Fermi's idea consisted of treating weak interactions as 'point-like' electromagnetic interactions; in order to make such an analogy clear, the electromagnetic scattering of an electron off a proton (see fig. 1.2) can be considered:

$$e + q \longrightarrow e + q \quad (q = u, d).$$

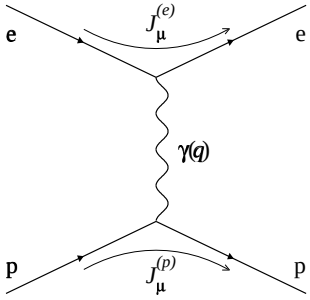

Figure 1.2: $ep \to ep$

Due to the fact that lepton and baryon numbers are conserved, this process can be thought as the interaction of two currents (indicated in figure 1.2 as J_μ) via a single (virtual) photon exchange, which leads to the

scattering amplitude:

$$\mathcal{M} \propto \overline{\mathrm{u}}\,\gamma^{\mu}\,\mathrm{u}\,\frac{e^2}{q^2}\,\overline{\mathrm{e}}\,\gamma_{\mu}\,\mathrm{e}\ ,$$

where q is the momentum transfer; for the cross-section, QED predicts:

$$\sigma \sim |\mathcal{M}|^2 \sim \frac{e^4}{s}\ , \tag{1.1}$$

where s is the square of the center of mass energy of the $\mathrm{e}-\mathrm{p}$ system.

By analogy, Fermi supposed that weak processes, such as the β-decay, could be described in a similar way; the requirement of 'contact' interaction leads to the amplitude:

$$\mathcal{M} \propto G_F\,(\overline{\mathrm{e}}\,\Gamma^{\mu}\,\nu_{\mathrm{e}})(\overline{\mathrm{u}}\,\Gamma_{\mu}\,\mathrm{d})\ ,$$

where the form of Γ^{μ} has been determined to be $\gamma^{\mu}(1-\gamma_5)/2$, in order to account for parity and charge conjugation violations which characterize weak interactions[1]. The numerical value of the Fermi's constant G_F has been estimated by comparison of the theoretical prediction for the β-decay rate with the empirical measurement to be $1.16639(1)\times 10^{-5}\mathrm{GeV}^{-2}$. Now, if the weak process:

$$\nu_{\mathrm{e}} + \mathrm{d} \longrightarrow \mathrm{e} + \mathrm{u},$$

which is still described by the diagram depicted in fig. 1.1, or any other weak scattering process, is considered, the Fermi theory predicts a cross-section:

$$\sigma \sim G_F^2 s\ . \tag{1.2}$$

For weak processes at high energies, this relation states that the cross-section is divergent with s; this goes against the S-matrix unitarity. In other words, expression (1.2) is a symptom of the sickness affecting the Fermi theory: non-renormalizability.

A possible solution to this problem consists in forcing the analogy between weak and electromagnetic processes by removing Fermi's assumption of 'contact' interaction in favour of a vector boson mediated weak interaction[2] (see fig. 1.3).

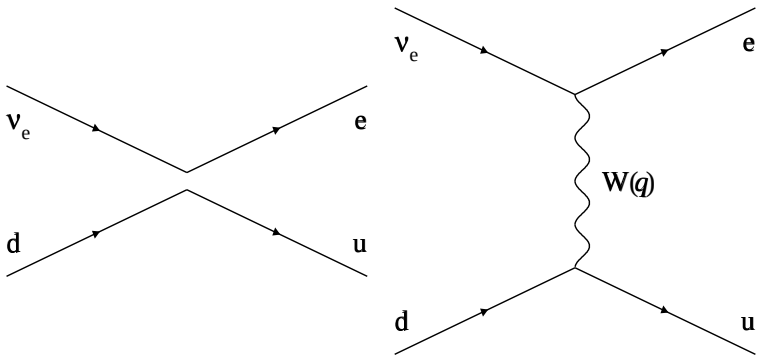

Figure 1.3: $\mathrm{e}-\nu_{\mathrm{e}}$ *elastic scattering as seen by Fermi and* IVB *theories.*

[1]For a definition of the Dirac matrices γ^{μ}, γ_5, see for example [2], Appendix A, § A.8.

[2]This approach is known as IVB (Intermediate Vector Boson) theory.

In order to preserve the short-range characteristic of the weak interactions, the intermediate boson (the so called $W^{\pm}$ particle) has to be massive. This has the immediate consequence of introducing a massive vector boson propagator:

$$\frac{g^{\mu\nu} - \frac{q^{\mu}q^{\nu}}{M_W^2}}{q^2 - M_W^2} \tag{1.3}$$

into the amplitude of the considered process.

Although the IVB theory reproduces Fermi's results in the low energy limit, removing at the same time the unitarity violations that appear at tree-level, it presents some difficulties that affect heavily its predictability:

- ◇ the IVB theory cannot describe some processes at tree-level. This is the case, for instance, of $e + \nu_\mu \rightarrow e + \nu_\mu$;
- ◇ unitarity violations still emerge at tree-level in processes like $e^+e^- \rightarrow W^+W^-$, where the total amplitude is the result of the interference of a weak and an electromagnetic contribution (see fig. 1.4).

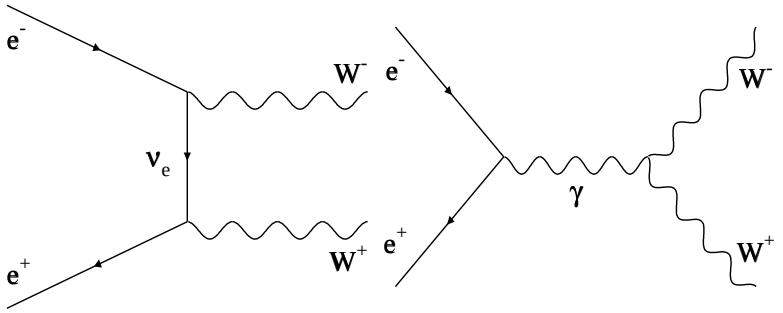

Figure 1.4: IVB *theory contributions to* $e^+e^- \rightarrow W^+W^-$

These signals seem to suggest that the IVB theory is not complete; the simplest and most logical way of addressing the problem consists in the introduction of a further vector boson (Z^0) with the following properties:

- ◇ it must be neutral, in order to enable neutral currents[3] at tree-level (see fig. 1.5);
- ◇ as the $W^{\pm}$, it must interact 'electroweakly' in order to be able to interfere destructively both with the weak and the electromagnetic diagrams which concur to a given process when these are simultaneously divergent; in the case of the process $e^+e^- \rightarrow W^+W^-$, the additional contribution is shown in fig. 1.6.

[3] As opposed to the currents involving the emission or absorption of a charged vector boson, which are indicated as 'charged currents'. In agreement with observations, neutral currents do not change the fermion flavour.

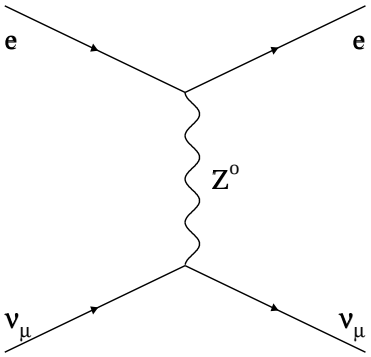

Figure 1.5: $e\nu_\mu \to e\nu_\mu$

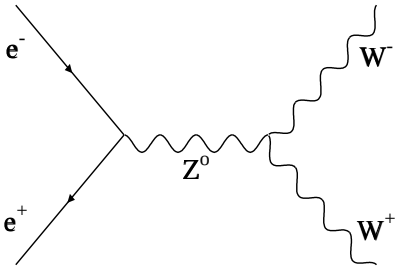

Figure 1.6: Z^0 *contribution to* $e^+e^- \to W^+W^-$ *(see fig. 1.4)*

This solution solves all the model diseases mentioned above[4], but the care works at tree-level only: higher-order calculations are still not possible; the reason this happens can be studied by considering the cross-section of the simple box diagram shown in fig. 1.7, where the (divergent) contribution of the loop integral is put in evidence (the divergence arises when the limit $\Lambda(\text{cutoff value}) \to \infty$ is taken).

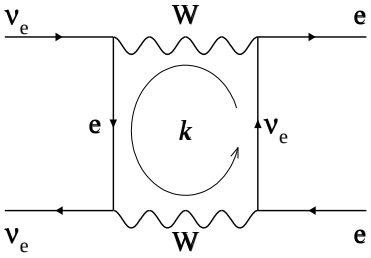

$$\Longrightarrow \qquad \int^{\Lambda} \mathrm{d}^4 k \frac{1}{k}\frac{1}{k} \sim \Lambda^2$$

Figure 1.7: *Box diagram for the electroweak theory.*

Since the effect evidenced in fig. 1.7 becomes progressively more severe as the perturbative order increases, it is clear that predictions beyond the tree level are not possible.
Interesting conclusions can be drawn at this point by the comparison with the behaviour exhibited by QED in an analogous situation (depicted in fig.1.8):

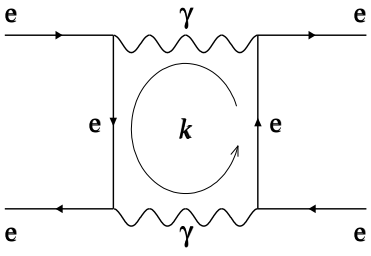

$$\Longrightarrow \qquad \int \mathrm{d}^4 k \frac{1}{k}\frac{1}{k}\frac{1}{k^2}\frac{1}{k^2}$$

Figure 1.8: *Box diagram for* QED.

[4] At least in the limit of massless fermions; see for example [3], § 21.2.

It is then clear that all problems are originated by the behaviour of the vector boson propagator in case of massive bosons V – see expression (1.3): in this case, the term $q^\mu q^\nu / M_V^2$ at high energies causes the suppression of the $1/q^2$ factor from the denominator, and, consequently, of the two $1/k^2$ factors which enable converging results in the cross-section of QED processes (where $M_\gamma = 0$).

1.1.2 The Standard Model of electroweak interactions

The previous paragraph has put in evidence the difficulty of formulating a renormalizable theory capable of describing the reality of electroweak interactions in terms of processes characterized by massive bosons exchanges.

At the same time, the origin of QED renormalizability comes from its intermediate boson being massless; this can be understood in terms of an underlying local symmetry obeyed by the theory: the Lagrangian density $\mathcal{L}$ of a system interacting electromagnetically has to be invariant under the field transformation:

$$\psi(x) \longrightarrow e^{iQ\theta(x)}\psi(x) \ ,$$

where Q – the generator of the transformation – is the electric charge operator. The symmetry group which describes such a transformation is an U(1) group, which is indicated as $\mathrm{U}(1)_{em}$ in order to remind the nature of the generator; the locality of the transformation is ensured by the space-time dependence of the transformation parameter θ.
On one hand the invariance under $\mathrm{U}(1)_{em}$ guarantees that electric charge conservation holds, while, on the other, a new vector field A^μ – which can be associated to the γ intermediate boson – has to be introduced in $\mathcal{L}$ through an interaction term with fermion fields. Although a kinetic term for A^μ is allowed by the overall symmetry, this does not hold true for a mass term, which imply necessarily that $M_\gamma = 0$. In other words, $M_\gamma = 0$ is a signal that the $\mathrm{U}(1)_{em}$ symmetry is not violated, which in turn implies that electric charge conservation.

The attempt of obtaining a renormalizable theory of electroweak interactions consists in providing the electroweak theory with a gauge[5] symmetry capable of reproducing the characteristic weak current left-right asymmetry responsible of parity and charge conjugation violations; in order to identify the local group, the weak charged current (see pag. 4):

$$J^\mu = \overline{\nu}_\ell \frac{1}{2}\gamma^\mu(1-\gamma_5)\ell$$

can be written as:

$$J^\mu = \overline{\mathrm{L}}\gamma^\mu\tau^+\mathrm{L} \ , \tag{1.4}$$

with:

$$\mathrm{L} = \tfrac{1}{2}(1-\gamma_5)\begin{pmatrix} \nu_\ell \\ \ell \end{pmatrix} \equiv \begin{pmatrix} \nu_\ell \\ \ell \end{pmatrix}_L$$
$$\tau^+ = \tfrac{1}{2}(\tau_1 + i\tau_2) \ ,$$

[5] *Id est* local.

where τ_a stand for the usual Pauli matrices[6]. Note that writing (1.4) forces the fermion fields $\psi = \ell, \nu_\ell$ to be assigned to some multiplet representation of the underlying (unknown) gauge group, of which τ^+ will be one of the generators; in other words, this procedure is aimed at pointing out an explicit sign of the gauge group by simple phenomenological considerations.
In the same way, the hermitian conjugate current $J^{\mu\dagger}$:

$$J^{\mu\dagger} = \overline{\mathrm{L}}\gamma^\mu\tau^-\mathrm{L} \ ,$$

with:

$$\tau^- = \frac{1}{2}(\tau_1 - i\tau_2) \ ,$$

has to be considered, since it is involved into the interaction as much as J^μ is.
Since gauge bosons and currents are in one-to-one correspondence with the generators of the symmetry group, and since these, in turn, form a closed set with respect to the commutation operation:

$$\overline{\mathrm{L}}\gamma^\mu \left[\tau^+, \tau^-\right] \mathrm{L} = \overline{\mathrm{L}}\gamma^\mu\tau_3\mathrm{L} \equiv J_3^\mu$$

describes an other admissible weak current; in particular, it represents the weak neutral current whose existence has been anticipated on the basis of phenomenological considerations (see pag. 5). No more weak currents – independent from $J^\mu, J^{\mu\dagger}, J_3^\mu$ – can be introduced in this way, since $[\tau_3, \tau^\pm] = 2\tau^\pm$.

Therefore, weak currents have been written in a form that points out a SU(2)-symmetric structure of weak interactions, since SU(2) is the group generated by the Pauli matrices; however, it should be noted that only left-handed fermions have been arranged in this scenario[7]. Since right-handed fermions, such as $\nu_{\ell R}$ and ℓ_R, do not participate in weak processes involving charged currents, one can suppose of arranging them into $\mathrm{SU}(2)_L$ singlets.

As previously mentioned, gauge bosons are in one-to-one correspondence to group generators of local symmetries; therefore, a vector boson field $\mathrm{W}_\mathrm{i}^\mu$ has to be associated to each of $\mathrm{SU}(2)_L$ generator τ_i. While the structure of the charged currents $J^\mu, J^{\mu\dagger}$ suggests that a suitable combination of the $\mathrm{W}_\mathrm{i}^\mu$ fields (precisely $(\mathrm{W}_1^\mu \mp \mathrm{iW}_2^\mu)/\sqrt{2}$) should be considered for representing the $\mathrm{W}^\pm$ bosons, it is immediately clear that the neutral current J_3^μ and, consequently, W_3^μ, cannot be identified with the electromagnetic current and its intermediate boson (γ) respectively. Two reasons support this conclusion: first, electromagnetic currents do not couple electrically neutral objects, such as neutrinos; secondly, electromagnetic currents do not exhibit parity or charge conjugation violations: in fact, they are characterized by a vector Lorentz bilinear (*id est* $\overline{\ell}\gamma^\mu\ell$ – see pag. 4), allowing both left and right-handed fermions to be involved in the electromagnetic interaction.
However, from the comparison between the weak neutral current:

$$J_3^\mu = \left(\overline{\nu}_{\ell L}\gamma^\mu\nu_{\ell L} - \overline{\ell}_L\gamma^\mu\ell_L\right) \qquad (1.5)$$

[6]Note that the subscript *'L'* to the lepton doublet reminds the action of the operator $(1-\gamma_5)/2$, which selects the left-hand helicity projection of a fermion field.

[7]This is the reason why this symmetry group is usually indicated as $\mathrm{SU}(2)_L$.

and the electromagnetic current:

$$J^{\mu}_{em} = -\left(\overline{\ell}_R \gamma^{\mu} \ell_R + \overline{\ell}_L \gamma^{\mu} \ell_L\right) \ , \tag{1.6}$$

it can be noted that the the last term in the right-hand side of (1.5) is part of the electromagnetic current (1.6) as well. This suggests that the electromagnetic current can be expressed in terms of the weak neutral current J^{μ}_3 and a new neutral current, indicated as 'weak hypercharge' current J^{μ}_Y associated to an *ad hoc* neutral generator Y of a gauge U(1) symmetry[8] which corresponds to a neutral gauge boson, B^{μ}. The simultaneous gauge-invariance under $\mathrm{SU(2)}_L$ and $\mathrm{U(1)}_{em}$ can therefore be expressed in terms of gauge-invariance under the $\mathrm{SU(2)}_L \times \mathrm{U(1)}_Y$ group, where $\mathrm{U(1)}_Y$ is the Abelian group generated by Y.

In this way, not only has the gauge symmetry group of the electroweak sector of the Standard Model been identified in $\mathrm{SU(2)}_L \times \mathrm{U(1)}_Y$, but also the interactions between gauge bosons and fermions ($g J^{\mu} \mathrm{W}^-_{\mu}$, $g J^{\mu\dagger} \mathrm{W}^+_{\mu}$, $g J^{\mu}_3 \mathrm{W}_{3\mu}$ and $g' J^{\mu}_Y \mathrm{B}_{\mu}$, where g, g' – the so-called 'coupling constants' – describe the strength of the weak and hypercharge current interactions) have been established in a very natural way according to symmetry considerations. As anticipated for leptons, left-handed fermionic fields participating in this picture are arranged into 'weak isospin' doublets:

$$\mathrm{L} = \begin{pmatrix} \nu_\ell \\ \ell \end{pmatrix}_L \begin{array}{l} \longrightarrow \ q = 0 \\ \longrightarrow \ q = -1 \end{array} \ , \ \ell = \mathrm{e}, \mu, \tau$$

$$\mathrm{Q} = \begin{pmatrix} u \\ d \end{pmatrix}_L \begin{array}{l} \longrightarrow \ q = 2/3 \\ \longrightarrow \ q = -1/3 \end{array} \ , \ \begin{array}{l} u = \mathrm{u}, \mathrm{c}, \mathrm{t} \\ d = \mathrm{d}, \mathrm{s}, \mathrm{b} \end{array} \ ,$$

where:

$$\begin{pmatrix} \cdot \\ \cdot \end{pmatrix}_L \begin{array}{l} \longrightarrow \ i_3 = 1/2 \\ \longrightarrow \ i_3 = -1/2 \end{array} \ ,$$

while their right-handed partners are $\mathrm{SU(2)}_L$ singlets (*id est* with $i_3 = 0$)[9]:

$$\begin{array}{ll} \mathrm{E} = \ell_R, & \ell = \mathrm{e}, \mu, \tau \\ \mathrm{U} = u_R, & u = \mathrm{u}, \mathrm{c}, \mathrm{t} \\ \mathrm{D} = d_R, & d = \mathrm{d}, \mathrm{s}, \mathrm{b} \end{array} \ .$$

Hence, the model of electroweak interactions has been provided with a non-Abelian gauge invariance; theories which exhibit this behaviour are known as Yang-Mills (YM) theories [4]. Their peculiarity consists in being renormalizable unless mass terms – which provide an explicit breaking of the gauge symmetry[10] – are introduced. Apparently, no step forward has been made with respect to the extension of the IVB theory; however, the mere essence of YM theories (symmetry), enables to exploit a mechanism that gives mass to both gauge bosons and fermions without an explicit violation of the gauge symmetry [5, 6, 7] nor the renormalizability [8].

[8] By definition, the relation between the neutral generators is:

$$Q \equiv I_3 + Y \ , \tag{1.7}$$

where $I_3 = \tau_3/2$ is called 'weak isospin'; the corresponding eigenvalues will be indicated by q, i_3 and y.

[9] Being $Q(\nu_{\ell R}) = 0$, $I_3(\nu_{\ell R}) = 0$ and, consequently, $Y(\nu_{\ell R}) = 0$, $\nu_{\ell R}$ states do not undergo electroweak interactions and, therefore, do not take part in the electroweak picture.

[10] Exactly as for QED, mass terms for gauge bosons are not allowed by symmetry requirements; the same holds true for fermion masses.

The Higgs mechanism

The breaking of a continuous symmetry can be achieved in two ways:

explicit: the Lagrangian density $\mathcal{L}$ contains terms which violate the gauge symmetry;

spontaneous: the Lagrangian density $\mathcal{L}$ is invariant under a given symmetry, while the vacuum state (ground state) is not.

As previously mentioned, explicit symmetry breakings lead to non-renormalizable models, in the following we will consider the aspects of spontaneously broken symmetries.

For a spontaneous symmetry breaking (SSB) to happen within the gauge theory of electroweak interactions, a pair of (complex) scalar fields has to be introduced into the model; in order to be eligible for a SSB mechanism, these fields must exhibit non-trivial transformations properties under the gauge groups they are meant to break. The simplest way of doing this consists in arranging the two scalar fields into a SU(2) doublet:

$$\phi = \begin{pmatrix} \varphi^+ \\ \varphi^0 \end{pmatrix} = \frac{1}{\sqrt{2}} \begin{pmatrix} \varphi_1 + i\varphi_2 \\ \varphi_3 + i\varphi_4 \end{pmatrix} \ .$$

According to gauge invariance and renormalizability, the most general term of self-interaction for the scalar fields is described by the potential:

$$V(\phi) = \mu^2 \phi^\dagger \phi + \lambda (\phi^\dagger \phi)^2 \ , \tag{1.8}$$

which, for $\lambda \geqslant 0$ and $\mu^2 < 0$ [11], has a minimum for:

$$|\phi|^2 = \frac{1}{2} \left[\varphi_1^2 + \varphi_2^2 + \varphi_3^2 + \varphi_4^2 \right] = -\frac{\mu^2}{2\lambda} \equiv \frac{v^2}{2} \ . \tag{1.9}$$

The spontaneous breaking of the $\mathrm{SU}(2)_L$ symmetry takes place in the act of choosing a particular vacuum state from the multitude defined by (1.9); if the situation where:

$$\varphi_1 = \varphi_2 = \varphi_4 = 0 \ , \ \varphi_3 = \sqrt{-\frac{\mu^2}{\lambda}} = v$$

is chosen, the vacuum expectation value (VEV) is:

$$\phi_0 = \frac{1}{\sqrt{2}} \begin{pmatrix} 0 \\ v \end{pmatrix} \tag{1.10}$$

and the ϕ field variations around the minimum $\phi_0 = \phi(0)$ can be always written as:

$$\phi(x) = \frac{1}{\sqrt{2}} e^{i\epsilon_i(x)\tau_i/v} \begin{pmatrix} 0 \\ v + h(x) \end{pmatrix} \tag{1.11}$$

by adjusting the value of the scalar fields $\epsilon_i(x)$. The number of these fields, which play the same rôle of the Goldstone bosons in the case of spontaneously broken global symmetries, corresponds to the number of broken generators. They are known as '*would-be* Goldstone'

[11] The first condition ensures the existence of a lower bound for V, while the second selects a degenerate vacuum.

bosons since, in virtue of the SU(2)-invariance exhibited by $V(\phi)$, they can be gauged away by the transformation $U(x)=e^{-i\epsilon_i(x)\tau_i/v}$; therefore[12]:

$$\phi(x)=\frac{1}{\sqrt{2}}\begin{pmatrix} 0 \\ v+h(x) \end{pmatrix} \tag{1.12}$$

This is essentially the core of the Higgs mechanism [9]: of the four degrees of freedom associated to the initial scalar fields φ_i, three are absorbed in the *would-be* Goldstone bosons gauging procedure, for being returned in terms of longitudinal degrees of freedom of three gauge bosons, which in this way acquire mass. The fourth degree of freedom is associated to $h(x)$ (the Higgs boson H^0) and represents the only physical scalar field of the model; its mass,

$$M_{\mathrm{H}}=\sqrt{2\lambda v^2}\ , \tag{1.13}$$

depends on the free parameter λ, and therefore is not predicted by theory. However, the renormalizability of the SM enables to set a range of admissible values of M_{H}; this can be done by solving the system of the one-loop renormalization group equations, which eventually describes the running of the quartic coupling constant λ in function of μ, the renormalization scale. The behaviour of $\lambda(\mu)$ for different initial conditions $\lambda(M_{\mathrm{Z}})$ – each related to a given value of M_{H} by the relation (1.13) – is depicted in fig. 1.9 (where the initial conditions $M_{\mathrm{H}}=60, 100, 130, 150, 190, 210\,\mathrm{GeV}/c^2$ have been used [10]). Upper and lower bounds can then be set on M_{H} by requiring that $\lambda \lesssim 1$ (perturbative regime condition) and at the same time $\lambda>0$ (*triviality* limit) up to a certain scale Λ which will define the upper limit of validity for the Higgs sector of the SM.

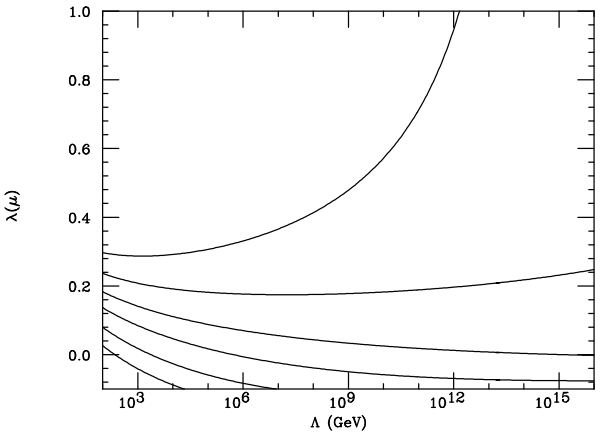

Figure 1.9: *Running of λ in function of energy scale Λ.*

The actual symmetry exhibited by $V(\phi)$ is larger than SU(2); indeed, $V(\phi)$ is left invariant by the action of the U(1) transformation:

$$\phi(x) \longrightarrow e^{i\alpha 1}\phi(x)\ ,$$

whose generator (1) is not a combination of the SU(2) generators. Therefore, the overall symmetry of $V(\phi)$ is $\mathrm{SU}(2)\times\mathrm{U}(1)$, the same as the electroweak gauge theory.
The vacuum state (1.10), violating the residual U(1) symmetry as well, leads to the spontaneous breaking of all four generators of the gauge symmetry. The possibility of giving mass to the photon, arising from the further *would-be* Goldstone boson implied by the U(1) breaking, is however ruled out since (1.10) preserves $(\tau_3+1)/2$, generator of $\mathrm{U}(1)_{em}$ (see (1.7)); since this is a combination of broken generators the violated gauge symmetry is partly recovered:

$$\mathrm{SU}(2)_L \times \mathrm{U}(1)_Y \longrightarrow \mathrm{U}(1)_{em}\ ,$$

[12] In the so-called unitary gauge.

and only three *would-be* Goldstone bosons are allowed.

Once the $\mathrm{SU}(2)_L \times \mathrm{U}(1)_Y$-gauge invariant Lagrangian density for the scalar field ϕ has been obtained:

$$\mathcal{L}_S = (D^\mu \phi)^\dagger (D_\mu \phi) - V(\phi) \ ,$$

where:

$$D^\mu = \partial^\mu + ig \mathrm{W}_a^\mu(x) \frac{\tau_a}{2} + ig' \mathrm{B}^\mu(x) \frac{1}{2}$$

(with $a = 1, 3$), the mass terms for the gauge bosons can be found by computing the kinetic term of $\mathcal{L}_S$ for $\phi = \phi_0$:

$$\frac{1}{8} v^2 g^2 \left(\mathrm{W}_1^\mu \mathrm{W}_{1\mu} + \mathrm{W}_2^\mu \mathrm{W}_{2\mu}\right) = \frac{1}{4} v^2 g^2 \mathrm{W}^{+\mu} \mathrm{W}_\mu^- \tag{1.14}$$

$$\begin{aligned} &\frac{1}{8} v^2 \left(g' \mathrm{B}^\mu - g \mathrm{W}_3^\mu\right) \left(g' \mathrm{B}_\mu - g \mathrm{W}_{3\mu}\right) = \\ &\quad = \frac{1}{8} v^2 \begin{pmatrix} \mathrm{W}_3^\mu & \mathrm{B}^\mu \end{pmatrix} \begin{pmatrix} g^2 & -gg' \\ -gg' & g'^2 \end{pmatrix} \begin{pmatrix} \mathrm{W}_{3\mu} \\ \mathrm{B}_\mu \end{pmatrix} \ . \end{aligned} \tag{1.15}$$

While (1.14) states that the combinations $\mathrm{W}^{\pm\mu} = (\mathrm{W}_1^\mu \mp \mathrm{W}_2^\mu)/2$, which can be interpreted in terms of $\mathrm{W}^\pm$ bosons, acquire a mass of:

$$M_\mathrm{W} = \frac{1}{2} v g \ ,$$

expression (1.15) predicts the mass eigenvalues $M_{1,2} = (v/2)\sqrt{g^2 + g'^2}$, 0 for the neutral bosons mass eigenstates:

$$\begin{pmatrix} \mathrm{Z}^\mu \\ \mathrm{A}^\mu \end{pmatrix} = \begin{pmatrix} \cos\theta_W & -\sin\theta_W \\ \sin\theta_W & \cos\theta_W \end{pmatrix} \begin{pmatrix} \mathrm{W}_3^\mu \\ \mathrm{B}^\mu \end{pmatrix} \ ,$$

where θ_W (Weinberg angle) is defined by the diagonalization condition $\tan\theta_W = g'/g$ for the mass matrix contained in (1.15). Once A^μ, the massless eigenstate associated to the unbroken generator Q, is identified with the photon field γ, the remaining field Z^μ will represent the neutral boson Z^0; in this way, Z^0 will be given the mass:

$$M_\mathrm{Z} = \frac{1}{2} \frac{vg}{\cos\theta_W} \ .$$

The rotation in the space of neutral boson fields modifies the couplings of the neutral currents to the corresponding gauge bosons:

$$\begin{aligned} \mathrm{Z}^0 \mathrm{f}\bar{\mathrm{f}} &\sim \left(I_3 - \sin^2\theta_W Q\right) g/\cos\theta_W \\ \gamma \mathrm{f}\bar{\mathrm{f}} &\sim g \sin\theta_W Q \end{aligned} \ ,$$

expressions that establish a formal relationship between weak and electromagnetic interactions; in particular, the latter suggests that:

$$e = g \sin\theta_W \ ,$$

which in turn – together with the diagonalization requirement ($\tan\theta_W = g'/g$) – implies:

$$e = g'\cos\theta_W \ .$$

The interaction of H^0 with the gauge bosons can be found by following a similar procedure: the kinetic term of $\mathcal{L}_S$ this time has to be expanded in terms of (1.12). Neglecting the kinetic term for h, one obtains:

$$(D^\mu\phi)^\dagger(D_\mu\phi) \supset \left(M_{\mathrm{W}}^2\mathrm{W}^{+\mu}\mathrm{W}^-_\mu + \frac{1}{2}M_{\mathrm{Z}}^2\mathrm{Z}^\mu\mathrm{Z}_\mu\right)\left(1+\frac{h}{v}\right)^2 \ ,$$

expression which describes, besides the gauge bosons mass terms, the interaction vertices:

$$\begin{array}{rcl} h\mathrm{Z}^0_\mu\mathrm{Z}^0_\nu & \sim & M_{\mathrm{Z}}^2 g_{\mu\nu}/v \\ h\mathrm{W}^+_\mu\mathrm{W}^-_\nu & \sim & M_{\mathrm{W}}^2 g_{\mu\nu}/v \\ hh\mathrm{Z}^0_\mu\mathrm{Z}^0_\nu & \sim & M_{\mathrm{Z}}^2 g_{\mu\nu}/(2v^2) \\ hh\mathrm{W}^+_\mu\mathrm{W}^-_\nu & \sim & M_{\mathrm{W}}^2 g_{\mu\nu}/(2v^2) \end{array} \ . \qquad (1.16)$$

As previously mentioned, explicit fermion mass terms are forbidden by the electroweak gauge symmetry; however, fermion masses can be generated by the Higgs boson VEV if the Lagrangian density of the model includes a $\mathrm{SU}(2)_L \times \mathrm{U}(1)_Y$-symmetric term which describes the interactions between fermions and H^0 in terms of Yukawa couplings:

$$\mathcal{L}_{Yuk} = -(\overline{\mathrm{L}}\phi h_{\mathrm{E}}\mathrm{E}) - (\overline{\mathrm{Q}}\phi h_{\mathrm{D}}\mathrm{D} + \overline{\mathrm{Q}}\tilde{\phi}h_{\mathrm{U}}\mathrm{U}) + h.c. \ , \qquad (1.17)$$

where $\tilde{\phi}$ is defined as the charge conjugate of ϕ [13]:

$$\tilde{\phi} \equiv i\tau_2\phi^* = \begin{pmatrix} \varphi^{0*} \\ -\varphi^- \end{pmatrix}$$

and h_{E}, h_{D} and h_{U} are generic $n \times n$ matrices in the generation space[14], since $\mathrm{SU}(2)_L$ singlets and doublets carry the same quantum numbers across fermion generations.

Fermion masses and couplings with H^0 emerge explicitly when expression (1.17) is evaluated in the unitary gauge (*id est* in terms of (1.12) and (1.18)):

$$\mathcal{L}_{Yuk} = -\frac{1}{\sqrt{2}}(v+h)\left[(\overline{\ell}_L h_{\mathrm{E}}\ell_R) + (\overline{d}_L h_{\mathrm{D}} d_R + \overline{u}_L h_{\mathrm{U}} u_R)\right] + h.c. \ . \qquad (1.19)$$

If quarks are considered, the determination of u and d-type quark masses corresponds to diagonalizing the matrices h_{D} and h_{U}; this can be done introducing the mass eigenstates u^0, d^0 connected to the interaction eigenstates u, d by two biunitary transformations:

$$\begin{array}{ll} u_L = U_L u^0_L \ , & u_R = U_R u^0_R \\ d_L = V_L d^0_L \ , & d_R = V_R d^0_R \end{array} \ , \qquad (1.20)$$

[13] $\tilde{\phi}$ has the same transformation properties of ϕ under $\mathrm{SU}(2)_L$; furthermore, the fluctuations around its VEV $\tilde{\phi}_0$ can be written as:

$$\tilde{\phi}(x) = \frac{1}{\sqrt{2}}\begin{pmatrix} v+h(x) \\ 0 \end{pmatrix} \ . \qquad (1.18)$$

[14] As of this writing, $n = 3$.

where the hermitian U_L, U_R, V_L, V_R matrices are chosen so that:

$$U_L^\dagger h_{\rm U} U_R = diag(h_{\rm U}^1, h_{\rm U}^2, \dots, h_{\rm U}^n)$$
$$V_L^\dagger h_{\rm D} V_R = diag(h_{\rm D}^1, h_{\rm D}^2, \dots, h_{\rm D}^n)$$

with $h^f_{\rm U,D}$ real and non-negative. In this way, the hadronic sector of (1.19) can be written in the form:

$$\mathcal{L}^{had}_{Yuk} = -\frac{1}{\sqrt{2}}(v+h)\sum_{f=1}^{n}\left(\overline{d}^0_{fL} h^f_{\rm D} d^0_{fR} + \overline{u}^0_{fL} h^f_{\rm U} u^0_{fR}\right) + h.c.\ ,$$

which puts in evidence both quark masses:

$$m^f_{\rm U} = \frac{h^f_{\rm U} v}{\sqrt{2}}\ ,\ \ m^f_{\rm D} = \frac{h^f_{\rm D} v}{\sqrt{2}}$$

and quark couplings to $\rm H^0$:

$$\rm H^0 q\overline{q} \sim \frac{m_q}{v}\ . \tag{1.21}$$

However, the rotation in the generation space induced by (1.20) affects the charged hadronic current; in fact, recalling (1.4):

$$J^\mu = \overline{\rm Q}\gamma^\mu \tau^+ {\rm Q} = \overline{u}_L \gamma^\mu d_L = \overline{u}^0_L U_L^\dagger \gamma^\mu V_L d^0_L = \overline{u}^0_L \gamma^\mu U_L^\dagger V_L d^0_L \equiv \overline{u}^0_L \gamma^\mu V_{CKM} d^0_L\ ;$$

V_{CKM} is known as Cabibbo-Kobayashi-Maskawa matrix and describes the mixing amplitude in flavour changing currents[15] [12, 13].

A different behaviour is on the other hand predicted for leptons; the difference is essentially due to the $\nu_{\ell R}$ carrying no electroweak quantum numbers, therefore forbidding any Yukawa coupling involving $\tilde{\phi}$. This implies the existence of only one mass matrix, $h_{\rm E}$, which can be diagonalized by the biunitary transformation:

$$V_L^{\ell\dagger} h_{\rm E} V_R^\ell = diag(h_{\rm E}^1, h_{\rm E}^2, \dots, h_{\rm E}^n)$$

(where $h^f_{\rm E}$ are required to be real and non-negative), which identifies the leptonic mass eigenstates:

$$\ell_L = V_L^\ell \ell^0_L\ ,\quad \ell_R = V_R^\ell \ell^0_R\ ;$$

at the same time, assuming ν_ℓ massless, the same transformation holds for the left-handed neutrino:

$$\nu_{\ell L} = V_L^\ell \nu^0_{\ell L}\ .$$

This makes the leptonic term in (1.19):

$$\mathcal{L}^{lept}_{Yuk} = -\frac{1}{\sqrt{2}}(v+h)\sum_{f=1}^{n}\left(\overline{\ell}^0_{fL} h^f_{\rm E} \ell^0_{fR}\right) + h.c.$$

[15] At tree-level, these processes can be described by charged current phenomena only; in fact, the detected suppression of flavour changing neutral currents (FCNC) led to quark $SU(2)$ doublets through the GIM mechanism [11].

clearly diagonal, while leaving weak charged currents unaffected:

$$J^\mu = \overline{\mathrm{L}}\gamma^\mu\tau^+\mathrm{L} = \overline{\nu}_{\ell L}\gamma^\mu\ell_L = \overline{\nu}^0_{\ell L}V_L^\dagger\gamma^\mu V_L\ell^0_L = \overline{\nu}^0_{\ell L}\gamma^\mu V_L^\dagger V_L\ell^0_L = \overline{\nu}^0_{\ell L}\gamma^\mu\ell^0_L \ .$$

Similarly to quarks, charged leptons masses are:

$$m^f_\ell = \frac{h^f_{\mathrm{E}}v}{\sqrt{2}} \ ,$$

in terms of which their couplings to H^0 can be expressed:

$$\mathrm{H}^0\overline{\ell}\ell \sim \frac{m_\ell}{v} \ . \tag{1.22}$$

1.1.3 Gauge theory of strong interactions: QCD

The electroweak model so far discussed can be completed by a description of strong interactions, which are responsible for the stability of hadronic matter.

The initial studies about strong processes – based only on hadron spectroscopy – suggested a model[16] in which hadrons were to be considered bound states of two or three elementary constituents, called *quarks*, with fractional electric charge and obeying a Fermi-Dirac statistics. In order to account for the stability of the Δ^{++} baryonic state, a new quantum number, *colour*, had to be assigned to quarks.

These hypotheses were confirmed by new experiments, aimed at probing the hadron structure at high energies by means of electrons scattering off hydrogen nuclei [14]; rising the energy of the electron beam above a certain scale (empirically determined in $\sim 0.71\,\mathrm{GeV}$), the electron-proton scattering was observed to behave inelastically, determining the onset of the so-called deep inelastic scattering (DIS) regime. The experimental data could be successfully interpreted on the basis of a new hadron model (the 'Parton model', proposed by Feynman [15]), according to which the interacting proton can be considered as a loosely-bound state of constituents[17], and, consequently, the e-p collision is interpreted as an interaction taking place between the electron and one of the proton's charged partons. The kinematics of these processes can be completely taken into account by two variables only: x (Bjorken x), describing the fraction of the proton's 4-momentum carried by the struck parton (quark), and y, the fraction of the incident electron's energy transferred to the hadronic system. When the DIS differential cross section, expressed in terms of the dimensionless parameters x and y, is considered in the limit of high energies, the x and y-dependencies factorize and one obtains:

$$\frac{\mathrm{d}^2\sigma}{\mathrm{d}x\mathrm{d}y} \propto \frac{1}{Q^2} \ ,$$

that is, the DIS differential cross section scales with the process energy[18].

Since this *scaling* effect reproduces the typical behaviour of a renormalizable field theory, it was noted that a description of strong (*hard*) processes could be achieved by

[16] Known as the 'Quark model'.

[17] These elementary constituents, called *partons*, include the fermionic, electrically charged states (like quarks), but also possibly other neutral species taking part in the strong interaction.

[18] In fact $Q^2 = -q^2$, where q is the 4-momentum exchanged during the collision.

means of a gauge theory. At the same time, however, it was clear that the new gauge theory had to account for a weak coupling at high energies (which is an implicit assumption of Feynman's Parton model); this ruled out Abelian symmetries. When it was discovered that gauge theories based on non-Abelian symmetries were characterized by asymptotic freedom[19] [4], a tentative description of strong phenomena by means of a SU(3) gauge theory coupled to the colour quantum number was quite natural; such a theory was therefore named Quantum ChromoDynamics (QCD) and its gauge group indicated as $SU(3)_C$. According to QCD, each quark can be thought in terms of an object having three colour states, therefore transforming as a triplet under $SU(3)_C$, while the corresponding bosons (the so-called *gluons*) can be considered as carrying all possible combinations of colour-anticolour: after removing the colour singlet arising from $R\overline{R}+G\overline{G}+B\overline{B}$, eight gluons are defined.

Furthermore, not only can the $SU(3)_C$ gauge theory account for high energy processes as DIS, but also low energy effects – such as hadron spectroscopy – can be explained; in fact, asymptotic freedom establishes a colour confinement regime at low energy, where the coupling constant becomes strong. This implies that in this region colour singlets are the only admissible (*id est* stable) states with finite energy predicted by QCD if the $SU(3)_C$ gauge is not broken. Since neither colour nor fractional electric charges have been ever observed, one can claim that the $SU(3)_C$ symmetry must not be violated; as a direct consequence of this, gluons must be massless.

Finally, QCD can be integrated into the picture of the electroweak theory, giving rise to the Standard Model of strong and electroweak interactions, whose gauge group is:

$$SU(3)_C \times SU(2)_L \times U(1)_Y \ ;$$

since leptons do not undergo strong interactions, both L and E (*id est* the left and right-handed leptonic components) must transform as singlets under $SU(3)_C$.

1.1.4 Beyond the Standard Model

Despite the many successes, culminated eventually in the discoveries of the $W^{\pm}$, Z^0 bosons [16, 17, 18] and of the top quark [19], and although no significative discrepancies have been detected with respect to the theoretical predictions [20, 21, 22], the Standard Model cannot be considered the ultimate theory of elementary particles.

Among the suggestions supporting this hypothesis, the *unification* and *flavour* problems: the former is related to the gauge interactions, whose symmetry pattern appears to be complicated and, in some way, arbitrary; the latter, on the other hand, is raised by the Yukawa interactions, which add further free parameters to those already introduced by the gauge structure of the theory.

Among the reasons which definitely relegate the Standard Model to a rôle of effective theory[20], its incapability of accounting for gravitational interactions (which are not at all included in the model) and the fact that some of the gauge couplings (specifically, all except the strong coupling) are not asymptotically free.

Given that the SM has to be considered an effective theory, the scale Λ above which the model looses validity needs to be determined. Two alternative scenarios are possible [23, 24]:

[19] *Id est* a situation describing a decreasing coupling constant for increasing energies.

[20] *Id est*, a theory whose validity is restricted to a certain energy range.

1. $\Lambda \sim \Lambda_{Planck} \sim 10^{18}\,\mathrm{GeV}$, as suggested by the asymptotic behaviour of the SM coupling constants, pointing towards the unification of electroweak and strong forces at $M_{GUT} \sim 10^{14} \div 10^{16}\,\mathrm{GeV}$;

2. $\Lambda \sim \Lambda_{Fermi} \sim \mu \sim 250\,\mathrm{GeV}$, as suggested by the assumption of new physics associated with the electroweak symmetry breaking.

A strong criticism to the first scenario can be found in the so-called *hierarchy* problem, related to the naturalness of the Higgs mass: although the internal consistency of the SM (see pag. 11) requires that $55\,\mathrm{GeV} \lesssim \mathrm{M_H} \lesssim 700\,\mathrm{GeV}$ (hence $M_\mathrm{H} \sim \mu$) [25], quadratically divergent contributions to M_H^2 are predicted by the SM (see fig. 1.10).

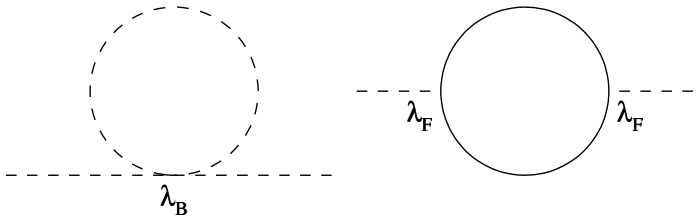

Figure 1.10: *One-loop contributions to scalar masses within the* SM.

Indicating with λ_B, λ_F the quartic scalar coupling and the Yukawa coupling respectively, one finds:

$$\delta M_\mathrm{H}^2 \sim (\lambda_B - \lambda_F^2)\Lambda^2 \ . \tag{1.23}$$

The hierarchy problem, then, is related to the difficulty of reconciling a scalar mass of the order of Λ_{Fermi} with unnaturally divergent contributions, which are expected to be proportional to $\Lambda \gg \Lambda_{Fermi}$. The same problem does not arise when fermion masses are considered: in this case, the chiral symmetry[21] protects the theory from undesirable divergences.

While no consistent way of overcoming the naturalness problem in the first scenario has yet been found, two possible solutions are being studied within the second scenario; one of these, aimed at investigating the possibility of substituting the Higgs mechanism by means of a dynamical breaking of the electroweak symmetry, has been inspired by the chiral symmetry breaking induced by quark condensates within the QCD framework. Models based on this idea, known as 'Technicolour' models, require the introduction of new generations of fermions undergoing a new strong interaction at a scale $\gtrsim \Lambda_{Fermi}$; however, their capability to formulate realistic predictions is still limited.

The other solution to the naturalness problem consists in embedding the SM within a theory characterized by broken supersymmetry (SUSY); in this case, the naturalness problem is solved by means of a symmetry which connects fermion fields with boson fields, establishing in this way a relation between the λ_F and λ_B couplings of (1.23). The simplest supersymmetric extension of the SM is the Minimal Supersymmetric Standard Model (MSSM), in which a global supersymmetry associated to a single fermionic generator ($N=1$ supersymmetry) is explicitly broken by Lagrangian terms introducing at most logarithmic divergences in loop corrections. A supersymmetric Higgs mechanism is invoked also in the

[21] *Id est* the $\mathrm{SU(2)}_L \times \mathrm{SU(2)}_R$ (global) which is established in $\mathcal{L}_{SM}$ in the limit of massless fermions.

MSSM, but in this case two Higgs doublets are required to give mass to all fermions and, at the same time, to prevent the theory from anomalies; at the end of the spontaneous $SU(2)_L \times U(1)_Y$ symmetry breaking, of the eight degrees of freedom initially associated to the Higgs doublets, three (the *would-be* Goldstone bosons) have been absorbed as the longitudinal degrees of freedom of the $W^{\pm}$, Z^0 gauge bosons. Therefore, five physical states are expected in the Higgs sector of MSSM:

$$H^{\pm} \quad h^0 \quad H^0 \quad A^0 \ ,$$

where h^0, H^0 are CP even and A^0 is CP odd; the tree-level predictions on their masses lead to the following relations:

$$\begin{array}{c} M_{H^{\pm}} = M_W + M_A \\ M_h \leqslant M_Z, \, M_A \leqslant M_H \end{array} \ .$$

Having the mass of the lightest Higgs boson an upper bound at M_Z and being h^0 not yet discovered, if the tree-level expectation were confirmed by higher-order corrections, the MSSM would have already been ruled out. However, the model is rescued by radiative corrections, which enable to raise the upper bound for m_h up to $\sim 130\,\mathrm{GeV}$.

Since over a significant region of the MSSM parameter space[22] the search for h^0 is equivalent to the search of the SM H^0 [23], the Higgs boson mass – if observed – would be a key parameter for getting some knowledge about the order of magnitude of the scale Λ at which the SM breaks down (which can be done using the information of fig. 1.11, obtained by interpolating the lower and upper bound values set by the procedure described at pag. 1.9).

Three interesting ranges for the lightest neutral Higgs boson are considered:

1. $110 \div 130\,\mathrm{GeV}$
2. $130 \div 190\,\mathrm{GeV}$
3. $190 \div 215\,\mathrm{GeV}$

($M_H \gtrsim 215\,\mathrm{GeV}/c^2$ is excluded by indirect measurements, $M_H \lesssim 110\,\mathrm{GeV}/c^2$ by direct searches – see § 1.2.2). Ranges 1 and 3 are accessible only if $\Lambda < \Lambda_{Planck}$; in this case, the second scenario of pag. 16 is favoured. The upper bound on the lightest neutral Higgs boson set by the MSSM (*id est* $130\,\mathrm{GeV}$) states that mass range 1 is preferred by the MSSM. Range 2, on the other hand, does not allow any conclusion on Λ, except for the fact that the hypothesis $\Lambda \sim \Lambda_{Planck}$ is not excluded any longer.

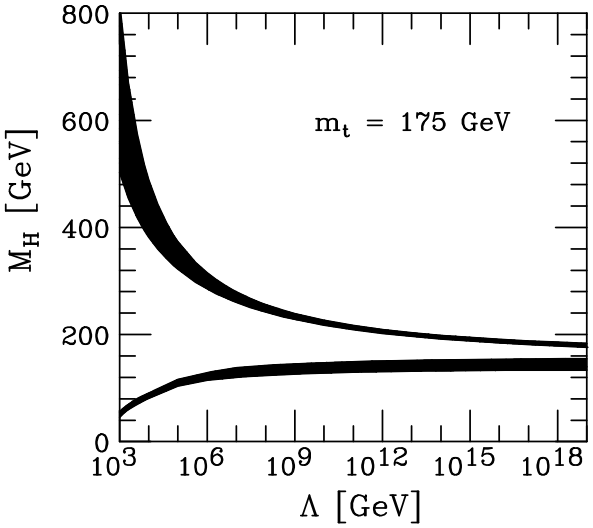

Figure 1.11: *Upper and lower bounds for* M_H *(*SM*) as functions of* SM *scale* Λ.

[22] Corresponding to the so-called *decoupling regime*, where:

$$\cos^2(\beta - \alpha) \equiv \frac{M_h^2 (M_Z^2 - M_h^2)}{M_A^2 (M_H^2 - M_h^2)} = 0 \ .$$

[23] This is quite a general result, that is, consistent also with models which assume less minimal Higgs sectors [26].

1.2 Higgs Phenomenology

Even if the SM has to be considered as an effective theory, probing the Higgs sector by searching for a neutral spin-zero particle is a crucial test for the consistency of a description of the electroweak interactions in terms of a quantum field theory; above all, the arguments presented in § 1.1.4 put in evidence the enormous impact an eventual discovery of a Higgs boson would have on further developments of the theory.

In the following sections, a phenomenological description of the dominant production mechanisms for a SM H^0 will be discussed in the framework of a hadronic collider running at $\sqrt{s} = 2\,\text{TeV}$, which represents the situation that will be faced in the Run II of the TEVATRON; indications on the most promising search channels will be drawn after H^0 decay modes have been taken into account. This review will in turn be followed by a summary of the current status of the Higgs searches performed at LEP and at TEVATRON.

1.2.1 H^0 Production and Decay

Production of SM H^0 at hadronic colliders proceeds through several processes; the cross sections for the most relevant ones are shown in fig. 1.12, where the Run II running conditions for TEVATRON are assumed.

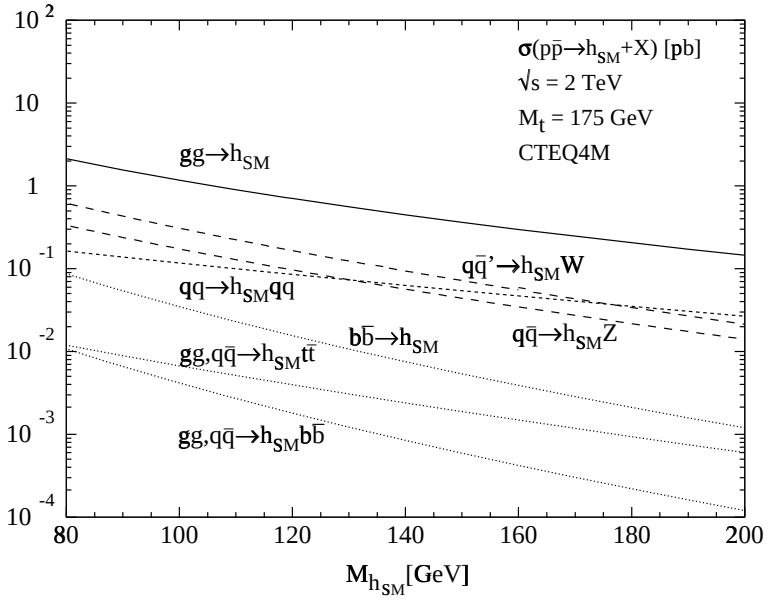

Figure 1.12: *SM Higgs production cross sections at* TEVATRON *as functions of* M_H*;* NLO QCD *corrections are included for all channels [26].*

As evidenced by the picture above, the leading processes throughout the whole admissible H^0 mass spectrum[24] are gluon fusion, Higgs*strahlung* (that is, radiation of a scalar field from a vector boson) and vector boson fusion; the three processes are depicted in fig. 1.13, while their cross sections, computed for different values of M_H (in the hypothesis of a light Higgs), are reported in table 1.1.

[24]Extending essentially from a lower bound established by experimental exclusion to an upper bound set by internal consistency of the electroweak theory.

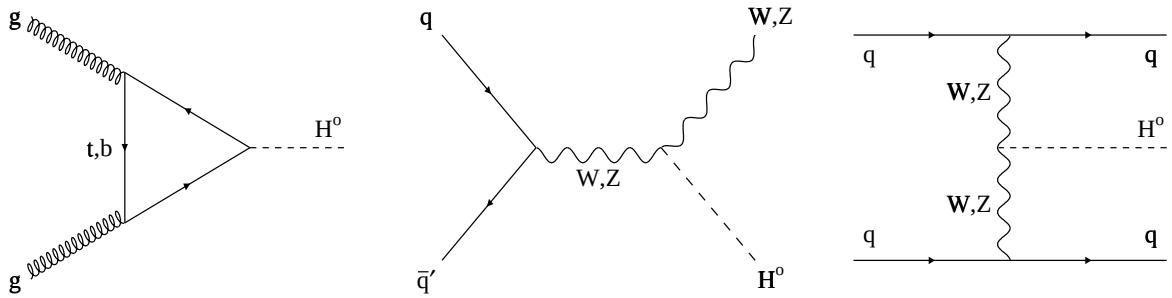

Figure 1.13: *SM Higgs dominant production processes at* TEVATRON*: from left to right, gluon fusion, Higgs*strahlung *and vector boson fusion. The loop in the left-hand diagram can be run by any fermion; however, the* $H^0 f\bar{f}$ *coupling, proportional to* m_f *(see expressions (1.21) and (1.22)), ensures that the loop contribution is by far dominated by heavy flavours.*

M_H [GeV/c^2]	Production cross sections [fb]			
	$gg \to H^0$	$q\bar{q}' \to W^{\pm}H^0$	$q\bar{q} \to Z^0H^0$	$qq \to H^0qq$
110	900	224	128	100
120	704	165	97	85.4
130	558	124	74	73.2

Table 1.1: *Cross sections for dominant* H^0 *production processes.*

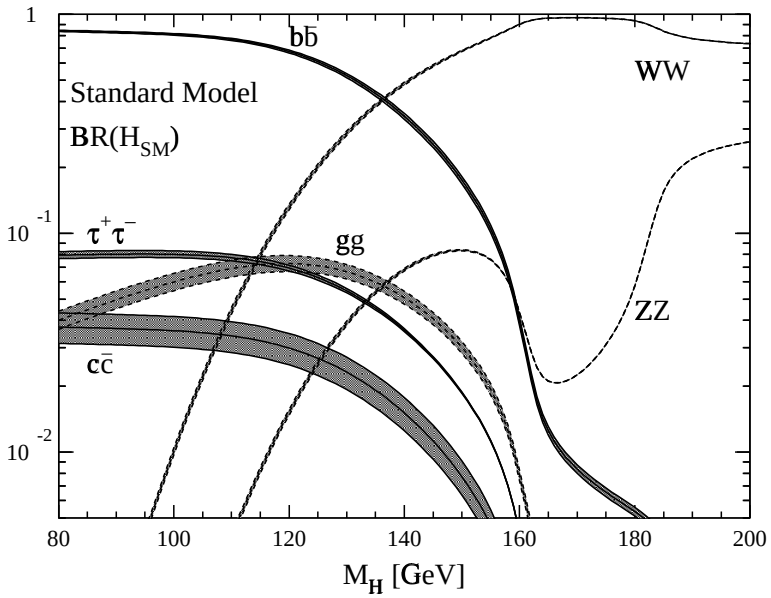

Figure 1.14: *SM Higgs branching ratios expressed as functions of* M_H*;* NLO QCD *corrections are included [27], while shaded bands result from the uncertainties on input parameters (*α_S*,* m_b*,* m_c*,* m_t*).*

The possible H^0 decay modes essentially are $H^0 \to f\bar{f}$ and $H^0 \to VV$ (where $VV = W^+W^-, Z^0Z^0$); in the first case, couplings are proportional to m_f (see (1.16) and (1.22)), while in the latter they depends on m_V^2 (see first two relations in (1.16)). This implies

that, if in the low mass range (up to $\sim 130\,\mathrm{GeV}/c^2$) decay channels into heavy fermion pairs are preferred, when the kinematical limit for producing a VV* pair is approached, the corresponding decay amplitude is enhanced. As a result, H^0 decays mostly into $\mathrm{VV}^{(*)}$ in the high mass spectrum; at the same time, the opening of the VV decay modes appears as a broadening of Γ_{H^0} when the threshold of $\sim 130\,\mathrm{GeV}/c^2$ is reached (see 1.15). The branching ratios behaviour as function of M_{H} is shown in fig. 1.14, while table 1.2 reports the values of the branching ratios for the most significant decay processes in a light Higgs boson scenario. Two observations need to be done; the first one is concerned with the $\mathrm{H}^0 \to \mathrm{gg}$, $\gamma\gamma$ decays. Their coupling to H^0 is mediated by a loop, described by diagrams formally identical to the gluon fusion (where the external gluon legs are eventually substituted by photons, in which case the loop can be run by $\mathrm{W}^{\pm}$ as well as heavy flavours). The latter, although being characterized by a very neat signature, is strongly suppressed ($B.R. \lesssim 2 \times 10^{-3}$).

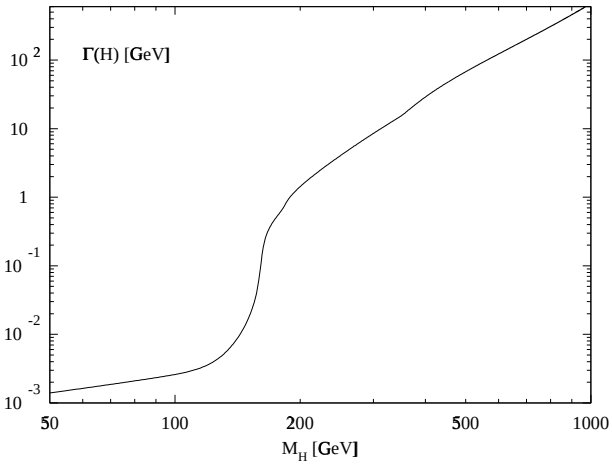

Figure 1.15: *Total width* Γ_{H^0} *as a function of* M_{H}.

The second observation has to do with the QCD corrections applied in fig. 1.14: although the process $\mathrm{H}^0 \to \mathrm{c\bar{c}}$ is colour enhanced, the running of the QCD coupling constant (α_S) produces a decrease in m_{c}, suppressing the channel below the $\mathrm{H}^0 \to \tau^+\tau^-$ limit.

M_{H}	Branching ratios		
$[\mathrm{GeV}/c^2]$	$\mathrm{H}^0 \to \mathrm{b\bar{b}}$	$\mathrm{H}^0 \to \tau^+\tau^-$	$\mathrm{H}^0 \to \mathrm{W}^+\mathrm{W}^-$
110	77%	8%	5%
120	68%	7%	13%
130	53%	5%	29%

Table 1.2: *Branching ratios for dominant* H^0 *decay channels.*

The combination of the information coming from the production of H^0 can then be merged with that regarding its decay modes; in this way, one can study *a priori* the most promising signatures which are expected within a given framework. For the purpose, two scenarios can be outlined:

Light Higgs scenario, corresponding to $M_{\mathrm{H}} \lesssim 130\,\mathrm{GeV}/c^2$; in this regime, the dominant decay mode of H^0 is $\mathrm{b\bar{b}}$. Although the process $\mathrm{gg} \to \mathrm{H}^0 \to \mathrm{b\bar{b}}$ is largely dominant on the others, its signature in this context is probably too weak to be distinguished by the overwhelming $\mathrm{b\bar{b}}$ background, coming essentially from direct production, flavour excitation and gluon splitting [28]. One possible handle for exploiting the potentiality of this channel could be offered by an improved $\mathrm{b\bar{b}}$ mass resolution[25], given the fact that for a light Higgs, the width of H^0 is of the order of 10 MeV (see fig. 1.15).

A more concrete opportunity could be offered by $\mathrm{gg} \to \mathrm{H}^0 \to \tau^+\tau^-$, even if in this case the

[25] Presently, a mass resolution of $\sim 10\%$ is achievable in the range of $\sim 100\,\mathrm{GeV}/c^2$.

necessary detector $\not\!\!E_T$ resolution could go beyond the capabilities of the CDF[26] detector. The limited production cross section, on the other hand, suppresses channels proceeding through vector boson fusion; in this case, the signature would consists of a $b\bar{b}$ pair from H^0 and two forward jets. This process has not been investigated during Run I; simulations of the new physics conditions and of upgraded detector expected for Run II, however, show that this channel is unlikely to give a substantial contribution in the Higgs search [26].
The most promising process for discovering a light SM Higgs boson is the associated production of H^0 with a vector boson V, where $H^0 \to b\bar{b}$. If, on one hand, the (semi)leptonic decay of V could provide an effective handle for QCD background rejection, on the other the hadronic decay of V provides a much higher event rate. In fact, assuming M_H=120 GeV/c^2:

$$B.R.\begin{pmatrix} H^0Z \to b\bar{b}\ell\bar{\ell}, \nu_\ell\bar{\nu}_\ell \\ H^0W \to b\bar{b}\ell\bar{\nu}_\ell \end{pmatrix} = \begin{cases} 6.87\%, 13.6\% \\ 21.9\% \end{cases} \longrightarrow \begin{matrix} 20 \text{ evts fb}^{-1} \\ 36 \text{ evts fb}^{-1} \end{matrix} \simeq 56 \text{ evts fb}^{-1}$$

$$B.R.\begin{pmatrix} H^0Z \to b\bar{b}q\bar{q} \\ H^0W \to b\bar{b}q\bar{q}' \end{pmatrix} = \begin{cases} 47.5\% \\ 46.1\% \end{cases} \longrightarrow \begin{matrix} 46 \text{ evts fb}^{-1} \\ 76 \text{ evts fb}^{-1} \end{matrix} \simeq 122 \text{ evts fb}^{-1}$$

At the same time, however, the fully hadronic decays of HV are affected by huge irreducible backgrounds (mostly coming from QCD $b\bar{b}$ production); the possibility of exploiting the higher statistics of these channels will be studied in chapter 4 and developed in the following sections. Within the MSSM framework, Higgs*strahlung* processes are in general suppressed by SUSY couplings; however, as previously anticipated (see pag. 18), this does not hold true in the decoupling limit of MSSM, where the light MSSM h exhibits SM Higgs behaviour. Therefore, SM Higgs searches through the HV channel are justified even within a MSSM framework when the decoupling limit is considered.
Heavy Higgs scenario, corresponding to $M_H \gtrsim 130\,\text{GeV}/c^2$; as previously pointed out, in this regime the decay channel $H^0 \to VV$ dominates on $b\bar{b}$. This has a positive relapse on the possible contributing production processes, since the decay products of the vector bosons help in background rejection even in the case of exclusive Higgs production.

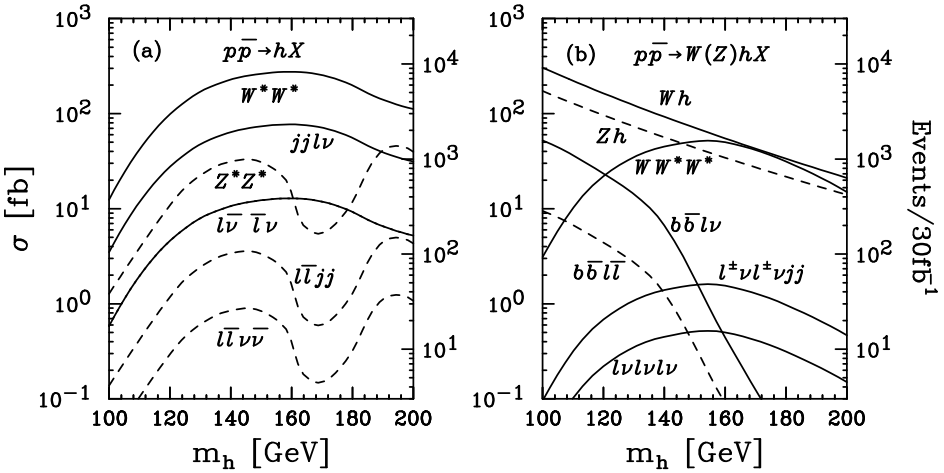

Figure 1.16: *Cross sections for* SM *Higgs production and subsequent decay modes in a heavy Higgs scenario for* $\sqrt{s} = 2\,\text{TeV}$*;* (a) $gg \to H^0 \to VV$ *and* (b) $q\bar{q}' \to H^0V$ *with* $H \to WW$. *Also shown* $H^0 \to b\bar{b}$ *with leptonic* V *decays.*

[26]The $\not\!\!E_T$ associated to the neutrinos from the τ decays is needed for estimating $m_{\tau\tau}$; Run I studies show that the resolution on this quantity is $\sim 25\,\text{GeV}/c^2$, which could not guarantee an appropriate H^0-Z^0 separation in the case of a light Higgs [29].

Fig. 1.16 shows the opportunities offered by this kind of mass range for H^0: $b\bar{b}$ modes are suppressed for rising M_H, while the processes:

$$\begin{aligned} H^0 &\rightarrow & WW &\rightarrow \ell\nu jj,\ \ell\nu\ell\nu \\ & & ZZ &\rightarrow \ell^+\ell^- jj,\ \ell^+\ell^-\nu\overline{\nu} \\ W^\pm H^0 &\rightarrow & \ell^\pm\nu WW &\rightarrow \ell\nu\ell\nu\ell\nu,\ \ell^\pm\nu\ell^\pm\nu jj \end{aligned}$$

(where j indicates a jet) supply clean signatures (*id est* high-P_T leptons) for the underlying Higgs production.

Furthermore, within a high-luminosity context and disregarding the Higgs mass, a possible neat signature can be offered by the process $qq, gg \rightarrow H^0 t\bar{t}$, whose predicted cross section is of the order of few pb in the considered Higgs mass range (see $qq, gg \rightarrow H^0 t\bar{t}$ in fig. 1.12). In this case the signature would consist of two high-P_T leptons coming from t quarks decaying semileptonically *plus* the observation of four b quarks in the final state, providing a powerful handle for background rejection.

1.2.2 Experimental results

The validity of the SM has been tested by a large variety of measurements performed on the various electroweak observables, providing in this way information on the fundamental parameters of the theory; the increased accuracy achieved on these measurements has required more precise theoretical calculations in order to enable more significative comparisons between theory and experimental results. The precision of the theoretical calculations is essentially related to the computation of higher-order corrections to tree-level processes, which take into account radiative phenomena. The convergence of such a procedure is guaranteed by the renormalizability of the SM.
As radiative corrections are taken into account, a quadratic dependence on m_t and a logarithmic dependence on M_H are exhibited by the electroweak observables [30, 31]; when the theoretical predictions are eventually compared to the corresponding measured observables, an 'indirect' measurement con be performed on M_H. This technique essentially consists of a fit on the experimental observables which returns the most likely value of M_H for reproducing what has been observed experimentally (see fig. 1.17); eventually, an upper bound can be set on at an M_H arbitrary confidence level ($C.L.$).
The logarithmic (and, therefore, weak) dependence from M_H, however, partially vanishes the power of such a technique and the constraints one can hope to set on M_H in this way are not very stringent:

$$M_H = 77^{+69}_{-39}\,\mathrm{GeV/c^2}\ ,\quad M_H < 215\,\mathrm{GeV/c^2}\ (95\%\,\mathrm{C.L.})\ ;$$

nevertheless, these results indicate that the low mass spectrum is preferred.

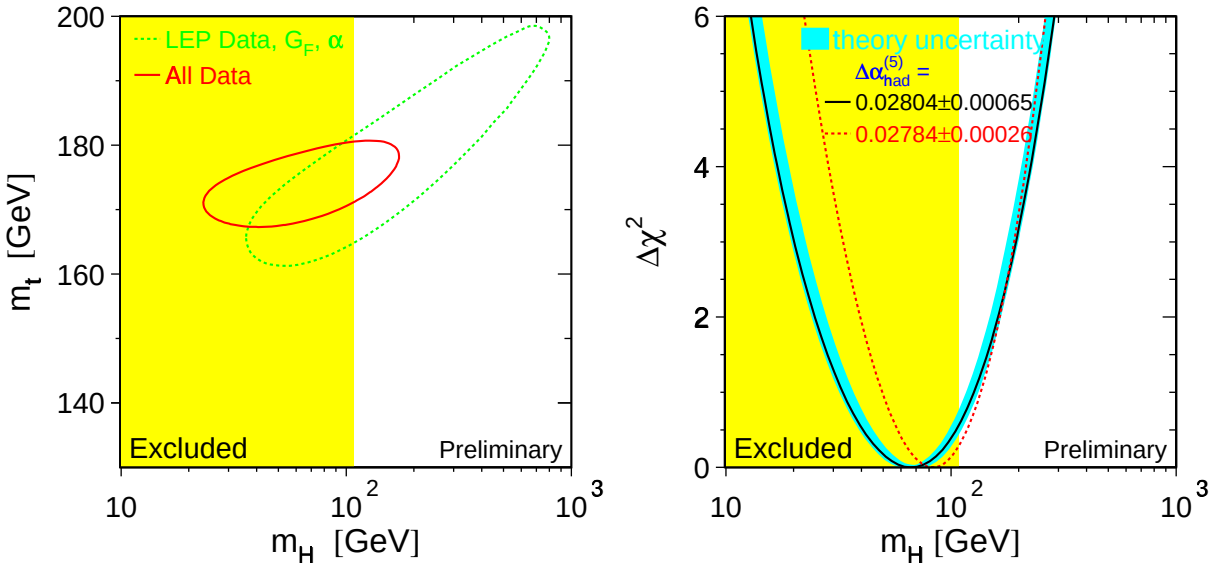

Figure 1.17: $1\sigma = 68\%$ *C.L. allowed region in the* m_t-M_H *plane (left).* $\Delta\chi^2 = \chi^2 - \chi^2_{min}$ *of fit to* M_H*; shaded light blue band represents theoretical uncertainty (right). Yellow bands indicate* 95% *C.L. exclusion region from direct measurement (see below) [31].*

In the following LEP final results of direct searches for H^0 (SM) will be presented; finally, the limits obtained by TEVATRON during Run I will be considered.

Searches at LEP

H^0 production processes at LEP are largely dominated by Higgs*strahlung* from a virtual Z^0; vector boson fusion contributions are also taken into account.

The searches performed by the four LEP experiments have been oriented to most of the final states arising from the Higgs*strahlung* process: all possible Z^0 decay modes have been considered in association with the leading H^0 decay channels ($b\bar{b}$, $\tau^+\tau^-$). In this way, the studied signatures include the four jets $H^0q\bar{q}$, the missing energy $H^0\nu\bar{\nu}$, the lepton pair $H^0\ell^+\ell^-$ (ℓ = e, μ) and the tau pair $H^0\tau^+\tau^-$, $H^0Z^0 \to \tau^+\tau^- q\bar{q}$. A classical cut-based analysis together as well as a neural network procedure have been used for selecting signal, background and observed events; the whole set of data has been used to test two hypotheses: the *background* (b) only, which assumes no signal, and the *signal+background* ($s+b$), where H^0 is assumed to be produced according to the SM. The experimental observation has then been classified as b-like or as $s+b$-like according to a negative log-likelihood ratio estimator defined as function of the H^0 mass hypothesis [32, 33]:

$$Q(M_H) = \frac{L_{s+b}(M_H)}{L_b(M_H)} = \frac{e^{-(s(M_H)+b)}}{e^{-b}} \prod_{j=1}^{n_{obs}} \frac{s(M_H)S(M_H; m_j^{rec}) + bB(m_j^{rec})}{bB(m_j^{rec})} , \qquad (1.24)$$

where $s(M_H)$, b and n_{obs} are the total number of signal, background and observed events, while $S(M_H; m_j^{rec})$, $B(m_j^{rec})$ are the probabilities of observing a signal or background event with a reconstructed mass m^{rec} for the H^0 candidate given a signal with mass M_H. Expression (1.24) has to be computed for each independent 'channel' i, where a channel uniquely identifies a contribution according to physical process, experiment and $\sqrt{s}$; then a combination of the various contributions can be obtained considering $Q(M_H) = \prod_i Q_i(M_H)$.

As a second test, the compatibility with background of the result is studied as a function of $M_{\rm H}$ by considering CL_b, the probability of observing an outcome more background-like (*id est*, with a lower value of Q) than the actually observed one for a given value of $M_{\rm H}$.

The analyses were performed on a sample collected at $\sqrt{s} \geqslant 206.5\,\mathrm{GeV}$ during the last year of running of LEP, corresponding to an integrated luminosity of $\sim 120\,\mathrm{pb}^{-1}$ per experiment.

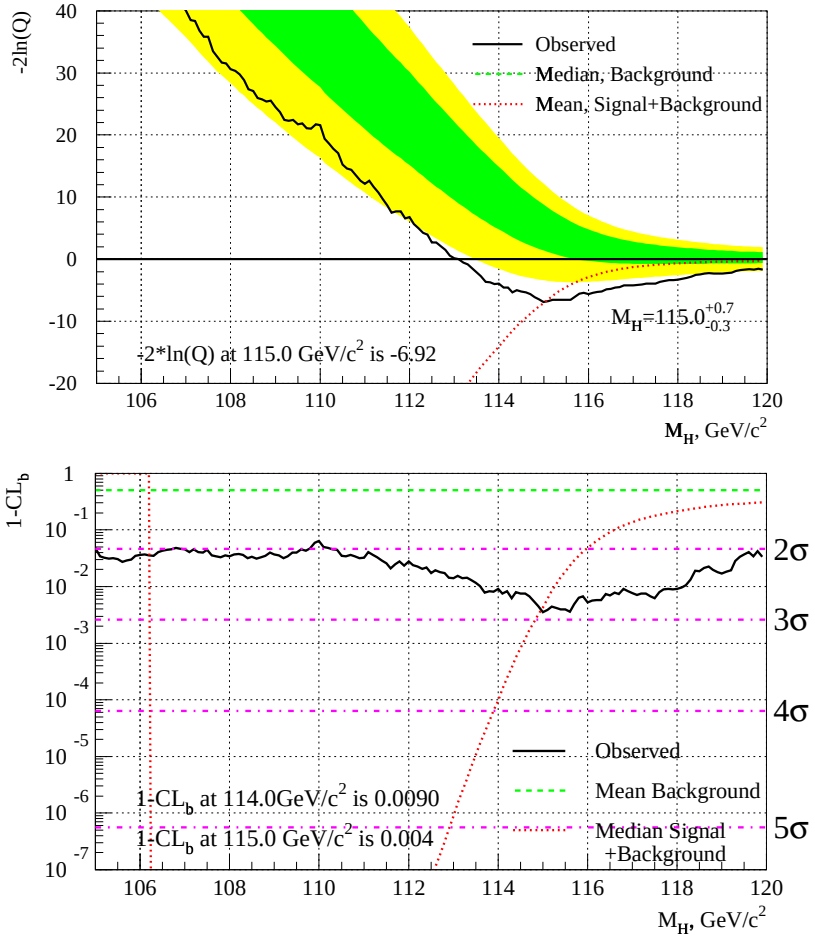

Figure 1.18: *Top: negative log-likelihood ratio as a function of $M_{\rm H}$; green and yellow bands correspond to 68 and 95% compatibility with the background only hypothesis. Bottom: $1-CL_b$ (solid curve) as a function of $M_{\rm H}$; excesses above the expected background are shown on the right axis. Both plots refer to* Y2K *data ($\sqrt{s} \geqslant 206.5\,\mathrm{GeV}$) collected by the four* LEP *experiments [34].*

The results of the two tests are shown in fig. 1.18; in both cases, the presence of signal is expected to show up as a dip in the observed curves for $-2\ln(Q)$ and $1-CL_b$. The best estimate for $M_{\rm H}$ is then found in correspondence to the minima. The collected data (20 high-purity events passed the selections) exhibit such a minimum for $M_{\rm H} = 115.0\,\mathrm{GeV}/c^2$, corresponding to a significance $(1-CL_b)$ of 2.9σ [34]; the previously quoted lower limit on $M_{\rm H}$ was $113.3\,\mathrm{GeV}/c^2$at 95% *C.L.* [32].

A claim for further statistics, necessary for eventually increasing the significance level of the evidence, has not been accorded by CERN, therefore remitting the final answer

concerning Higgs searches to future experiences at hadron colliders (TEVATRON and LHC).

Searches at TEVATRON

Direct searches of the SM Higgs boson have been performed at the TEVATRON collider during Run I.

The searches have been focused on the H^0 production process where a light Higgs boson is produced in association with an intermediate vector boson V, which, although being not the dominant production process for H^0, supplies some handles for background rejection (see pag. 21). Most decay channels of the intermediate vector bosons have been considered, while H^0 has been assumed to decay exclusively into a $b\bar{b}$ pair; in this way, searches have been concentrated onto four final states: $\ell^+\ell^- b\bar{b}$, $\nu_\ell\nu_\ell b\bar{b}$, $\ell\nu_\ell b\bar{b}$, $qqb\bar{b}$, where $\ell = e, \mu$. A brief prospectus reporting the guidelines of the four analyses is shown in table 1.2.2.

Channel	**Selection**	N_{exp}	N_{bgd}		N_{obs}
$\ell\nu_\ell b\bar{b}$	$P_T(\ell) > 20\,\text{GeV}/c$ $\not\!\!E_T > 20\,\text{GeV}$ 2 jets, $E_T > 10\,\text{GeV}$ 2(1) b−jets	0.11 (0.27)	3.8 (34)	QCD $t\bar{t}$	6 (36)
$\nu_\ell\nu_\ell b\bar{b}$	$\not\!\!E_T > 40\,\text{GeV}$ $\delta\phi(\not\!\!E_T)_{iso} > 1.0$ 2 or 3 jets, $E_T > 15\,\text{GeV}$ $\delta\phi(\textit{leading jets}) > 2.6$ 2(1) b−jets	0.13 (0.19)	4.9 (43)	Z + h.f. ZZ, $t\bar{t}$	4 (40)
$\ell^+\ell^- b\bar{b}$	$P_T(\ell^\pm\ell^\mp) > 20, 10\,\text{GeV}/c$ $\lvert M_Z - M_{\ell\ell}\rvert < 15\,\text{GeV}$ $\not\!\!E_T < 50\,\text{GeV}$ 2 or 3 jets, $E_T > 15\,\text{GeV}$ 2 b−jets	0.075	4.0	Z + h.f. ZZ, $t\bar{t}$	5
$qqb\bar{b}$	$\Sigma E_T > 125\,\text{GeV}$ $\geqslant 4$ jets, $E_T > 15\,\text{GeV}$ $\geqslant 2$ b−jets $P_T(b\bar{b}) \geqslant 50\,\text{GeV}/c$	0.70	474 QCD 120 other	QCD Z + h.f. $t\bar{t}$	589

Table 1.3: *Detailed list of* HV *search channels for* CDF*; the columns describe the investigated* HV *decay mode, the selection applied, the number of signal events expected for* $M_H = 110\,\text{GeV}/c^2$ *after selection in the channel, the number of expected background events (and their origin) and the number of observed events during Run I [35, 36, 37, 38, 39]. In brackets the results obtained with a single tag procedure.*

All decay processes included in the search rely on some b-tagging procedure, in order to identify one or two jets in each event as coming from a b quark; in any case, at least one jet has to be tagged tightly by means of an algorithm which identifies a jet as 'b-jet'

when it is compatible with a secondary vertex[27] fulfilling the requirement $L_{xy}/\sigma_{xy} > 3$, where L_{xy} and σ_{xy} are the measured value and uncertainty of its transverse displacement with respect to the beam axis. A second, looser b-tag, may be required on another jet; in this case, the tag may be supplied by two alternative procedures, which, instead of relying on secondary vertex reconstruction, exploit the B-hadrons decay tendency of producing displaced tracks and leptons characterized by a soft P_T spectrum. The first technique assigns to each jet a probability of coming from a b quark according to the impact parameter distribution of its tracks, while the latter returns a tag for those jets containing a track which has been tagged as a soft lepton.

Once the different topologies have been studied singularly, a combination of the obtained results has been performed and an answer in terms of minimum accessible cross section can be given for the signal as a function of $M_{\rm H}$. For this purpose, the two-jet[28] mass distribution has been used as the input for a binned maximum likelihood procedure [35]; the estimator:

$$L(M_{\rm H}) = \prod_{j}^{n_{bins}} \frac{\mu_j^{n_j}\, e^{-\mu_j}}{n_j!} \tag{1.25}$$

has been defined in terms of the unknown $\sigma_{\rm HV}$ and of n_j, the number of observed events in each bin of the dijet mass distribution; in order to gain information about the presence of signal, μ_j, the number of expected events (*signal+background*) in the j-th bin of the dijet mass distribution, is written as:

$$\mu_j = \sigma_{\rm HV} \mathcal{L}^j_{int} \epsilon_j s_j(M_{\rm H}) + \sum_k B_k b_k \ ,$$

with $s_j(M_{\rm H})$ and b_k relative signal and background weights biasing the number of signal and background events in the j-th bin (respectively $\sigma_{\rm HV}\mathcal{L}^j_{int}\epsilon_j$ and B_k – where k runs on all possible backgrounds for the considered channel). Expression (1.25) refers to a single physical process, say the i-th decay channel of HV; the total likelihood can therefore be obtained by considering $L(M_{\rm H}) = \prod_i L_i(M_{\rm H})$.
In order to keep into account possible sources of systematic errors, backgrounds (B_k), acceptances and luminosities are Gaussian constrained by means of a multiplicative factor $\mathcal{G}$ to the total likelihood function.

The analysis was performed on the data collected by CDF during Run I ($\sqrt{s} = 1.8\,\text{TeV}$) and correspond to an integrated luminosity $\mathcal{L}_{int}$ of $106\,\text{pb}^{-1}$.

The best estimate for $\sigma_{\rm HV}$ as a function of $M_{\rm H}$ can be obtained by means of a minimization procedure on $-\ln L(M_{\rm H})$, the negative log-likelihood for the combined search. More significative in the case of CDF are the 95% *C.L.* exclusion curves (shown in fig. 1.19); these are obtained by integrating the negative log-likelihood function expressed in terms of $\sigma_{\rm HV}$ only[29] from 0 to the value of $\sigma_{\rm HV}$ which encloses an area underneath the $-\ln L(M_{\rm H})$ curve equal to 0.95. The results, besides being shown in fig. 1.19, are reported in table 1.4.

[27] The compatibility of a jet with a secondary vertex is defined in terms of a minimum number (usually two or three) of displaced tracks extrapolating to the secondary vertex and contained in the considered jet.

[28] In case of double tag, the dijet system coincides with the b-tagged pair; when only one b-tagged jet is required, all possible combinations which includes the b-tagged jet are considered.

[29] *Id est* integrating out all other dependencies.

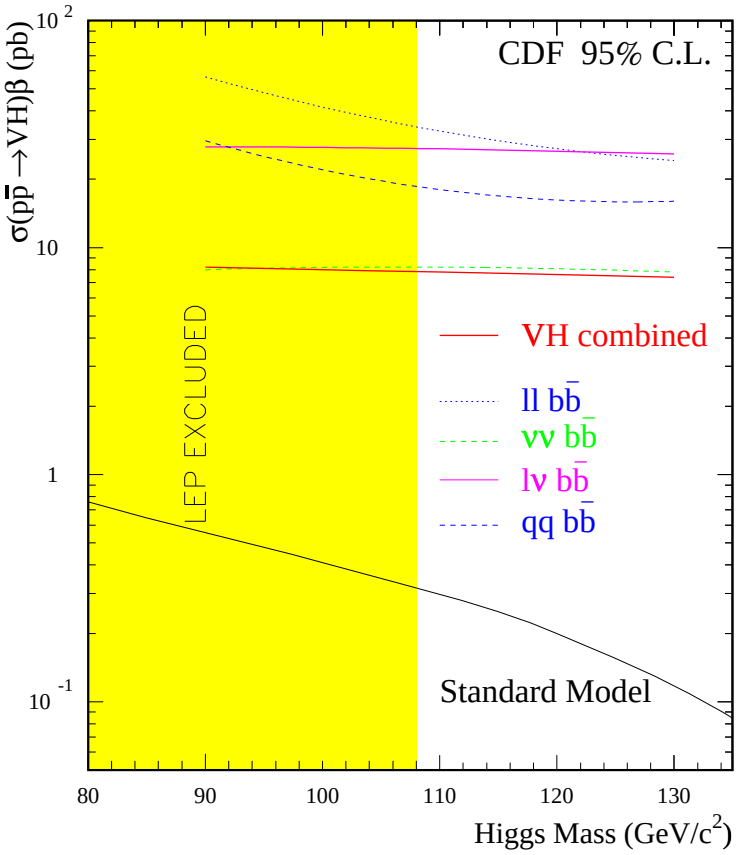

Figure 1.19: *95% C.L. limits on* $\sigma(p\overline{p}\rightarrow VH^0)\beta$ *set by* CDF*'s direct searches;* β *represents the branching ratio of each contributing channel, assuming* $H^0\rightarrow b\overline{b}$ *[35].*

M_H [GeV/c^2]	Cross sections [pb] Measured	SM Prediction
110	8.2	0.352
120	7.8	0.262
130	7.4	0.198

Table 1.4: *Measured and predicted (*SM*)* HV *production cross sections at* CDF *in a light Higgs boson scenario [35].*

The obtained results obtained by CDF show that the possibility of probing the electroweak breaking mechanism was out of reach for TEVATRON during Run I; the claim for an increased statistics and, more important, an enhanced sensibility towards new physics phenomena – like Higgs physics – are the basis for accelerator and detector improvements that will characterize the Run II and that will be described in the next chapter.

Bibliography

[1] E. Fermi, *Z. Physik* **88**, 161 (1934).

[2] F. Mandl, G. Shaw, *"Quantum Field Theory"*, John Wiley & Sons (1996).

[3] M. E. Peskin, D. V. Schroeder, *"An Introduction to Quantum Field Theory"*, Addison-Wesley (1997).

[4] C. N. Yang, R. L. Mills, *Phys. Rev.* **D 50**, 1173 (1954).

[5] S. Glashow, *Nucl. Phys.* **22**, 579 (1961).

[6] S. Weinberg, *Phys. Rev. Lett.* **19**, 1264 (1967).

[7] A. Salam, *Elementary Particle Theory: Relativistic Groups and Analicity*, Proc. of the 8th Nobel Symp., p. 367, ed. N. Svartholm, Almqvist and Wiksell, Sweden (1968).

[8] G. 't Hooft, *Nucl. Phys.* **B 33**, 167 (1971).

[9] P. W. Higgs, *Phys. Lett.* **12**, 132 (1964); *Phys. Lett.* **13**, 508 (1964).

[10] G. Ridolfi, *"An Introduction to the Standard Model of Electroweak Interactions"*, lecture notes.

[11] S. Glashow, J. Iliopoulos, L. Maiani, *Phys. Rev.* **D 2**, 1285 (1970).

[12] N. Cabibbo, *Phys. Rev. Lett.* **10**, 531 (1963).

[13] M. Kobayashi, K. Maskawa, *Progr. Theor. Phys.* **49**, 652 (1973).

[14] J. I. Friedman, H. W. Kendall, R. E. Taylor, *Rev. Mod. Phys.*, **63**, 573 (1991).

[15] R. P. Feynman, *Phys. Rev. Lett.* **23**, 1415 (1969).

[16] G. Arnison *et al.* (The UA1 Collaboration), *Phys. Lett.* **122 B**, 103 (1982).

[17] M. Banner *et al.* (The UA2 Collaboration), *Phys. Lett.* **122 B**, 476 (1982).

[18] C. Rubbia, Nobel Lecture, *Rev. Mod. Phys.* **57**, 699 (1985).

[19] F. Abe *et al.* (The CDF Collaboration), *Phys. Rev. Lett.* **74**, 2626 (1995).

[20] D. Abbaneo *et al.* (The ALEPH, DELPHI, L3 and OPAL Collaborations, LEP Electroweak Working Group, and SLD Heavy Flavour and Electroweak Groups), CERN-EP/99-15, 1999.

[21] M. Swartz, talk presented at the 1999 Lepton Photon Symposium, Stanford CA, USA, 9-14 August 1999.

[22] J. Mnich, talk presented at the 1999 International Europhysics Conference in High Energy Physics, Tampere, Finland, 14-21 July 1999.

[23] F. Zwirner, *"Beyond the Standard Model"*, DFPD 98/TH/17, April 1998.

[24] G. Altarelli, *"The Standard Electroweak Theory and Beyond"*, HEP-PH/0011078, Nov 2000.

[25] M. Spira, P. M. Zerwas, *"Electroweak Symmetry Breaking and Higgs Physics"*, HEP-PH/9803257, Dec 1997.

[26] M. Carena, J. S. Conway, H. E. Haber, J. D. Hobbs *et al.* (The Fermilab Higgs Working Group), *"Report of the Tevatron Higgs Working Group"*, HEP-PH/0010338, Oct 2000.

[27] M. Spira, *"Higgs Boson Production and Decay at the Tevatron"*, HEP-PH/9810289, Oct 1998.

[28] M. Paulini, *"*B *Lifetimes, Mixing and CP Violation at CDF"*, CDF internal note 4843, May 1999.

[29] A. Connolly, *"Studies for a Run I Search for a Directly Produced Higgs Decaying to Two Taus"*, CDF internal note 5307, May 2000.

[30] H. Spieseberger, M. Spira, P. M. Zerwas, *"The Standard Model: Physical Basis and Scattering Experiments*, HEP-PH/0011255, Nov 2000.

[31] The LEP Electroweak Working Group, `http::://lepewwg.web.cern.ch/LEPEWWG/`.

[32] The ALEPH, DELPHI, L3 and OPAL Collaborations (The LEP Higgs Working Group), *"Searches for Higgs bosons: Preliminary combined results using LEP data collected at energies up to 209* GeV/c^2*"*, contribution to ICHEP'2000, Osaka, Japan, July 27 - Aug 2, 2000.

[33] R. Barate *et al.* (The ALEPH Collaboration), *"Observation of an Excess in the Search for the Standard Model Higgs Boson at ALEPH"*, CERN-EP/2000-138, Nov 2000.

[34] The LEP Higgs Working Group, `http::://lepewwg.web.cern.ch/LEPHIGGS/`.

[35] M. Kruse, J. Valls, W. Yao (The CDF Higgs Working Group), *"Combined CDF* VH *production cross section limits for Run I"*, CDF internal note 4985, Apr 2000. Submitted to *Phys. Rev. Lett.*

[36] M. Kruse, W. Yao, *"Search for* $ZH \to \ell^+\ell^- b\bar{b}$ *in Run I"*, CDF internal note 4827, Jan 1999.

[37] W. Bokhari, C. Holck, W. Yao, *"Search for* $ZH \to \nu\bar{\nu}b\bar{b}$ *production"*, CDF internal note 4663, Apr 1999.

[38] F. Abe *et al.* (The CDF Collaboration), *"Search for New Particles Decaying into* $\mathrm{b\overline{b}}$ *and produced in Association with* W *Bosons Decaying into* $\mathrm{e}\nu$ *or* $\mu\nu$ *at the Tevatron"*, *Phys. Rev. Lett.* **79**, 3819 (1997).

[39] F. Abe *et al.* (The CDF Collaboration), *"Search for Higgs Bosons Produced in Association with* W *a Vector Boson in* $\mathrm{p\overline{p}}$ *Collisions at* $\sqrt{s}=1.8\,\mathrm{TeV}$*"*, *Phys. Rev. Lett.* **81**, 5748 (1998).

Chapter 2

Tevatron and CDF upgrades for Run II

With the shutdown of LEP, occurred at the beginning of November 2000, TEVATRON will be the only machine where collisions above the TeV-scale will be observable, making this accelerator the best candidate for new physics discoveries until the start of LHC.

However, the machine and detectors setup for Run I were not optimal for these kind of searches, leading to a low statistics for achieving enough sensitivity on processes (Higgs physics) whose limited production cross sections essentially reflect the smallness of the electroweak coupling constant and the high mass of the new particles involved. The ambitious physics goals that have been proposed for Run II therefore need specific upgrades of both the accelerator complex and detector components.

This chapter describes the upgrades that the TEVATRON accelerator and the CDF detector[1] have undergone, leaving to next chapter the discussion of the optimization of physics tools in terms of the new detector setup.

2.1 The accelerator upgrade

The number of events which are expected for a given process is given by the expression:

$$N_{evts} = \sigma \cdot \int \mathrm{d}t\mathcal{L} \ ,$$

where σ is the cross section of the considered process and $\mathcal{L}$ is the instantaneous luminosity achievable by the experiment; therefore, N_{evts} can be increased in three ways:

1. performing the experiment in the situation that maximizes σ;
2. augmenting the experiment instantaneous luminosity;
3. increasing the running time of the experiment.

Being aimed at pursuing a larger statistics, the proposed upgrades for TEVATRON, the accelerator facility at FERMILAB, essentially follow the previous scheme; steps 1 and 2 respectively translates into:

[1] Most of the information about the detector upgrades is contained in [1].

◇ increasing the center of mass energy of the $p\overline{p}$ collisions;

◇ increasing the luminosity of the accelerator.

Collision energy. As mentioned in the previous chapter, the Run II of TEVATRON will be characterized by a center of mass energy of $\sqrt{s} = 2\,\text{TeV}$, some 10% higher than in Run I; this will enhance production cross sections for signals which are within the physics goals of Run II: for instance, $t\overline{t}$ and H^0V production cross sections will be respectively $\sim$40% and $\sim$30% higher than in the Run I scenario.

Accelerator luminosity. While the collision energy influences the production cross section, the accelerator luminosity – related to the collision frequency – affects the datasets in the sense that determines the rate at which $p\overline{p}$ collisions occur; the instantaneous luminosity can be expressed in terms of:

$$\mathcal{L} \propto \frac{f B N_{\text{p}} N_{\overline{\text{p}}}}{2\pi\,(\sigma_{\text{p}}^2 + \sigma_{\overline{\text{p}}}^2)}\ ,$$

where:

f :	beam revolution frequency,
B :	number of proton/antiproton bunches,
$N_{\text{p},\overline{\text{p}}}$:	number of protons/antiprotons per bunch,
$\sigma_{\text{p},\overline{\text{p}}}$:	transverse proton/antiproton bunch dimension at interaction point,

while the proportionality is provided by a form factor depending on the beam longitudinal size and on its dispersion in phase space.

While maintaining the number of protons/antiprotons per bunch almost the same than in Run I, the most significant improvement towards high luminosities has been achieved by increasing the number of bunches from 6 to 36; this, together with reduced bunch sizes, is responsible for an expected instantaneous luminosity of $\sim 10^{32}\,\text{cm}^{-2}\text{s}^{-1}$ for Run II.

Two side-effects come as consequences of augmenting the number of bunches, affecting both detector working and consequent event reconstruction: first, a higher number of bunches reduces the time between collisions, which in turn implies a shorter time available for readout; according to the number of bunches, crossing time decreases from 3.5 μs (Run I, 6 bunches) to 396 and 132 ns in Run II for 36 and 108 bunches respectively. This has a strong consequence on readout and triggering procedures: events collected by the detector need to be piled up in memory and fed to the trigger boards through a pipeline in order to avoid readout latency during processing. Secondly, more than one hard or semi-hard scattering can occur in a beam cross; the average number $\overline{N}$ of interactions per beam cross is determined by the number of bunches and by the instantaneous luminosity (see fig. 2.1).

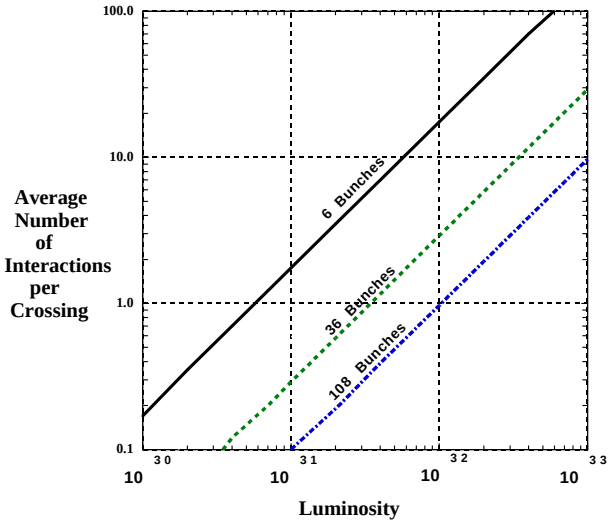

Figure 2.1: *Average number of interactions per beam cross for various beam conditions.*

In the following, a description of the various components of TEVATRON in Run II configuration is provided.

2.1.1 Proton production and Booster

The proton source at Fermilab is composed by a 400 MeV linear accelerator 150 m long, the Linac, which is fed with 750 keV negative hydrogen ions by a Cockcroft-Walton accelerator. Exiting from the Linac, the two electrons are stripped off the ions when the latter traverse a thin sheet of graphite; the so-obtained protons are injected into a small synchrotron having a diameter of 150 m, the Booster, which accelerates protons to an energy of 8 GeV. At the same time, the Booster collects the protons into bunches, part of which are destinated to antiproton production.

2.1.2 The Main Injector

The bunches of protons produced in the Booster are injected into the Main Injector, a 3 km proton syncrotron, whose main function is accelerating protons and antiprotons to an energy of 150 GeV, ready to be injected into the TEVATRON. Another feature of the Main Injector consists in its capability of decelerating antiprotons, a functionality which reveals very useful for recovering unused antiprotons when Tevatron is not in colliding mode.

The Main Injector replaces the Main Ring, in use during Run I, which, being initially planned for proton acceleration in fixed target experiments, was not optimal to be driven as an injector for the TEVATRON due to its low phase space acceptance.

2.1.3 Antiproton production and cooling

Antiprotons are produced by dumping a 120 GeV proton bunch from the Main Injector onto a nickel target; the antiprotons produced in the collision are collected by a lithium lens, from which they emerge with an energy of ~ 8 GeV. The pulses of antiprotons are fed into the Debuncher Ring, where they are collected as a continuum and stochastically cooled; further cooling proceeds in the Accumulator, into which they are moved from the Debuncher Ring. When a sufficiently high number of antiprotons is available, they are cooled into a bunch and this is injected into the Recycler Ring.

2.1.4 The Recycler Ring

The Recycler Ring serves as an antiproton accumulating ring and is located in the same cavity hosting the Main Injector; the purpose of this device – which did not exist at all during Run I – is electron-cooling and storing the bunches of antiprotons produced by the Accumulator or recovered by the Main Injector until they are used again. This enables an efficient management of the antiproton bunches: on one hand, at the end of a run they are not dumped (as it used to be during Run I), while on the other – thanks to the architecture of the Recycler Ring, based upon permanent magnets – they can be stored without the risk of loosing the beam as a consequence of power losses or surges. The importance of this device is related to the limiting power of the antiproton production

on the colliding procedure at FERMILAB: for this reason, the recycling of antiprotons can provide itself a factor two increase on the average integrated luminosity.

2.1.5 The Tevatron

The TEVATRON is a 6 km $p\overline{p}$ circular collider: oppositely charged beams are arranged to circulate in opposite directions within the same beam pipe. The energy of proton and antiproton bunches is raised from 150 GeV (*id est*, the nominal value of the beam energy on exiting the Main Injector) to 1 TeV before beams are crossed[2] and collisions take place.

Exploiting the upgrades developed specifically for each component of the accelerator chain, TEVATRON will be capable of producing $p\overline{p}$ collisions at $\sqrt{s}=2$ TeV with a luminosity that, after machine fine tuning, should reach the value of $\mathcal{L}\simeq 2\times 10^{32}\,\mathrm{cm}^{-2}\mathrm{s}^{-1}$, which would allow the delivery of a total integrated luminosity of $2\,\mathrm{fb}^{-1}$ in approximately two years.

2.1.6 The Tevatron Monitors

The quality of the beams provided by the TEVATRON needs to be constantly monitored in order to permit effective control of the physics processes taking place in the detectors; in particular, beam luminosity and loss, together with positioning and dispersion, need to be kept under control.

Luminosity monitor: although for Run II the instantaneous luminosity $\mathcal{L}$ will undergo a factor ten increase, the average luminosity per bunch will remain almost constant with respect to Run I; for this reason, a luminosity monitor based on the same technology used during Run I – that is, scintillator arrays placed on both sides of the interaction region – can be used in Run II. Luminosity will be defined by considering time-coincidences between particles (both in p and $\overline{\mathrm{p}}$ directions) leaving the interaction point, while an estimate of beam losses can be given in terms of another time-coincidence, fulfilled by particles moving through the interaction region in the proton *or* antiproton direction.

Beam position monitor: beam position and profile monitoring will essentially follow the scheme used in Run I. In this picture, the tracking devices of each detector will be engaged at the beginning of each data-taking fill for determining the beam average position, as well as their profiles and direction; this information will be made immediately available to the TEVATRON control room in order to optimize the accelerator performance.

2.2 The CDF II detector

The Collider Detector at Fermilab (CDF) has been upgraded in order to both accommodate the increased luminosity and reduced time-interval between consecutive bunches, which require faster readout and triggering.

[2] Of the twelve beam cross possible points, ten are avoided by means of electrostatic separators; the remaining two correspond to the CDF and D0 interaction points.

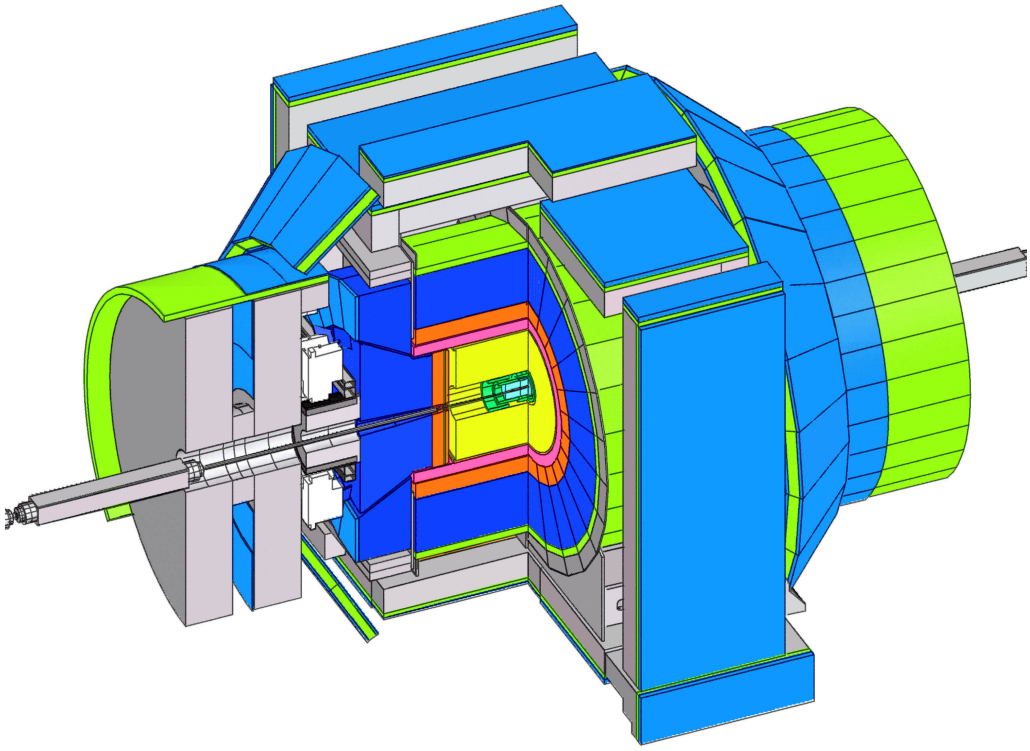

Figure 2.2: CDF II *detector section.*

For these reasons all tracking devices, which are concentrated in the inner part of CDF, have been redesigned. At the same time, new readout electronics has been provided to all detector subsystems.

Furthermore, the long period of machine development (started in 1996) has permitted the review of the whole detector in terms of an acceptance increase, which has mainly interested the tracking, the calorimeter and the muon systems (whose enlarged geometrical coverage can be appreciated in fig. 2.2).

Before giving a brief description of CDF II subdetectors, it is convenient to define the two currently used coordinate systems.

Cartesian system: the z axis is coincident with the beamline, its positive direction parallel to the motion of protons. The xy plane contains the nominal interaction point, which coincides with the center of CDF; the x axis is oriented horizontally towards the outer side of the accelerator ring, while the y axis remains defined by requiring (x, y, z) to a be right-handed system.

Polar system: the origin of the system is the same as in the Cartesian case. The azimuthal angle ϕ is measured in the xy plane starting from the x axis, being positive in the anti-clockwise direction; the polar angle θ is measured from the positive direction of the z axis. Finally, r defines the transverse distance from the z axis. The *pseudorapidity*, defined in terms of θ as:

$$\eta = -\ln\left(\tan(\theta/2)\right) \ ,$$

is particularly useful at hadron colliders, where events are boosted along the beamline[3],

[3]The longitudinal momenta of the colliding partons are distributed according to the Bjorken x (see § 1.1.3), therefore not leading to a complete cancellation of p_z in the collision.

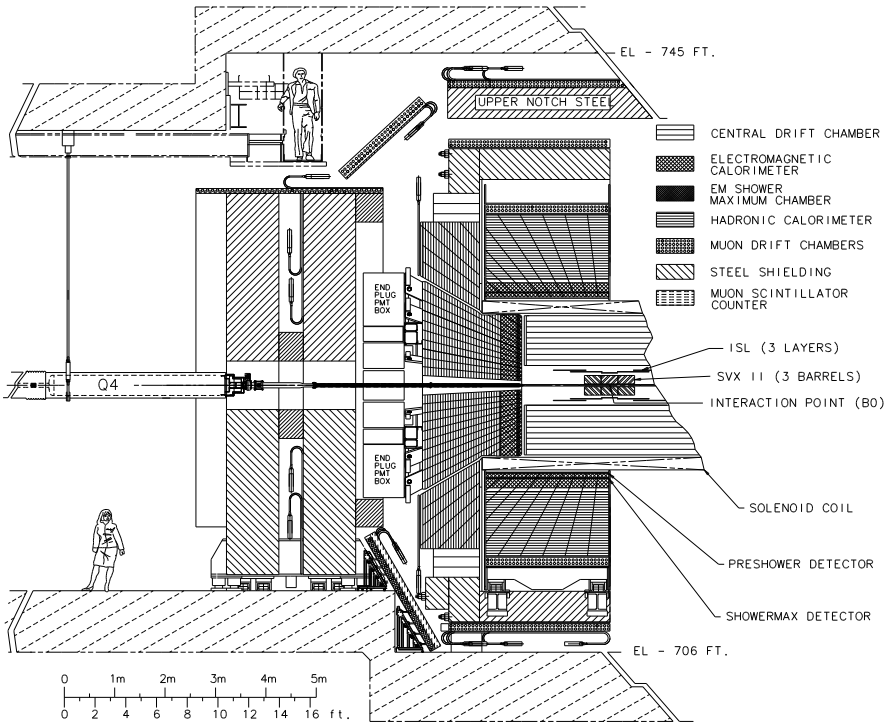

Figure 2.3: *$r-\phi$ view of the* CDF II *detector (half detector shown).*

since it transforms linearly under Lorentz-boosts:

$$\eta \longrightarrow \eta + \tanh^{-1}\beta$$

(having indicated with β the relative velocity associated to the boost). This implies that pseudorapidity gaps, $\Delta\eta$, are relativistic invariants, preserving in this way the average particle flux per unit of η. This fact has influenced the segmentation of the calorimetric apparatus.

2.2.1 The tracking system

The detector subsystems enclosed in a superconducting solenoid providing a uniform magnetic field[4] of 1.5 T are essentially dedicated to the reconstruction of the charged particles trajectories. The description of the each component of the tracking system is arranged according to an 'outside-in' scheme.

The Central Outer Tracker

The Central Outer Tracker (COT) is a new open-cell drift chamber, replacing the Central Tracking Chamber (CTC), that was unable to meet the necessary specifications needed for working in the typical Run II environment, where high occupancies and event rates are expected.

[4]The magnetic field produced by the CDF solenoid is parallel to the beamline; its uniformity refers to a cylindrical fiducial volume $\sim$3.5 m long and $\sim$2.8 m wide.

From the mechanical point of view, the problem of occupancy has been solved by reducing the physical dimensions of the cells; this has been done by increasing by a factor four the number of available cells. Each cell, containing an array of 12 sense wires, is tilted with respect to the radial direction (see fig. 2.4) by an angle which minimizes the drift time, which in the COT is ~ 5 times shorter than in the CTC; this result, obtained also by optimizing the gas mixture contained by the chamber volume, meets the necessity of completing the collection of showering electrons before the next bunch crossing.

The overall cell layout follows from the Run I configuration: cells are organized in eight *superlayers*, whose arrangement is visible in fig. 2.4; even-numbered superlayers, equipped with axial wires, provide $r-\phi$ information, while $r-z$ information comes from the odd-numbered superlayers, whose wires are assembled with a small stereo angle ($\pm 3^o$). Since all cells contain 12 sense wires, stereo sampling in the COT is double than in the Run I CTC.

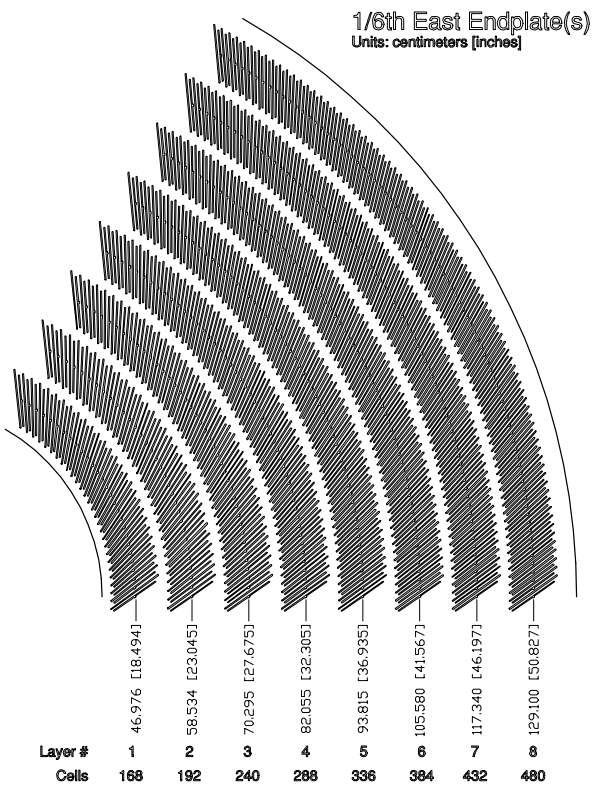

Figure 2.4: $\Delta\phi = 60^o$ *sector of* COT.

The COT, covering a radial region between 40 and 138 cm, is capable of tracking in the region with $|\eta| < 1$, provided that the track traversing its volume has $P_T \gtrsim 300\,\mathrm{MeV}/c$.

The Intermediate Silicon Layers

The Intermediate Silicon Layers (ISL) detector is based on double-sided silicon crystals: one side of each crystal provides an axial (*id est* pure $r-\phi$) measurement, while the other one has stereo microstrips supplying z information.
The structure of this detector varies according to the η range:

- $|\eta| < 1$**:** a single layer of silicon crystals is placed at an average radius of ~ 22 cm;
- $1 < |\eta| < 2$**:** two layers of silicon crystals are placed at average radii of ~ 20 and ~ 29 cm.

The number of layers in the ISL ranges between one and two according to η for ac-

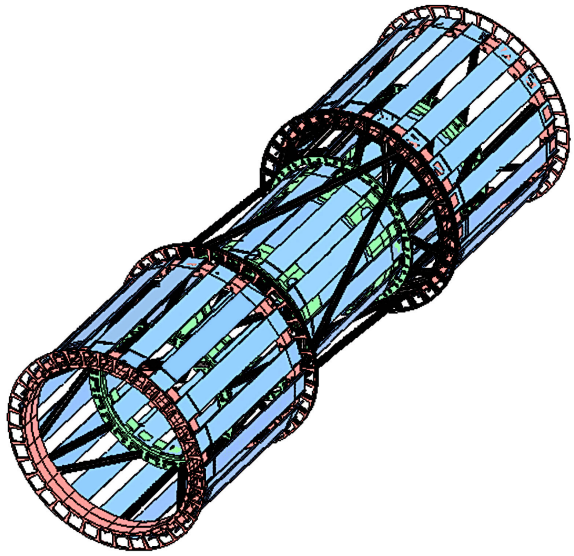

Figure 2.5: *Perspective view of* ISL.

commodating the possibility of stand-alone silicon tracking (in combination with SVX II – see next section and fig. 2.9) in the central region but also where COT information is incomplete or missing; in both cases, the contribution of ISL, thanks to its stereo sampling, enables a full three-dimensional reconstruction.

The Silicon Vertex Detector

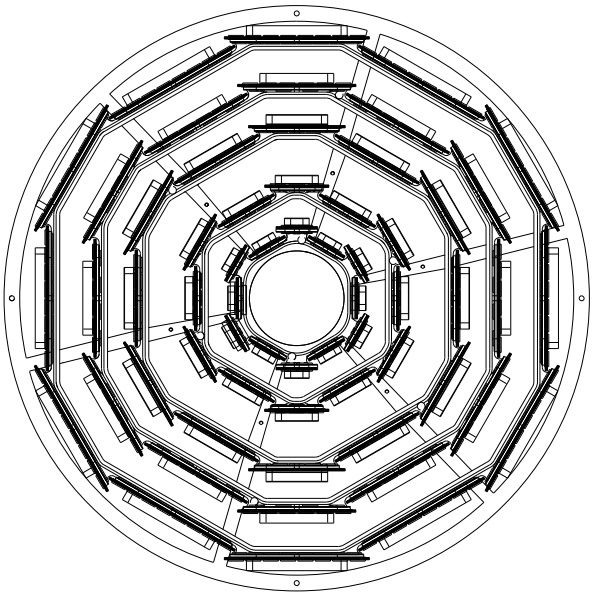

Figure 2.6: *$r-\phi$ view of* SVX II.

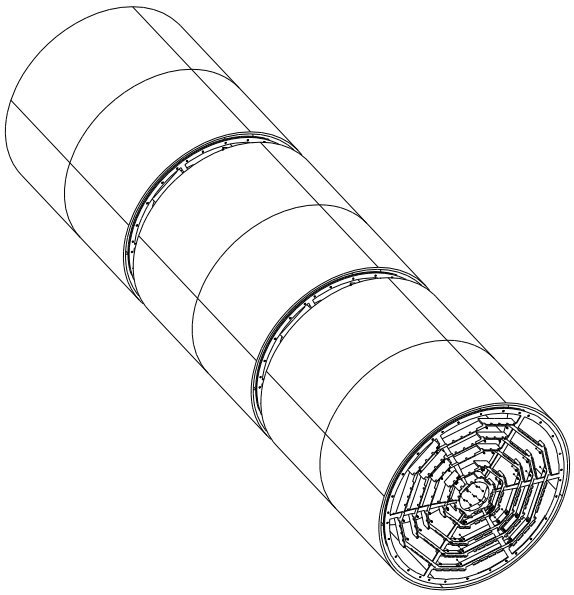

Figure 2.7: *Perspective view of* SVX II.

The Silicon Vertex Detector (SVX II) is a five-layer detector wrapped around the beam pipe: layers, grouped into 12 ϕ-wedges, are placed at radii ranging from 2.5 and 10.6 cm (see fig. 2.6, where outermost radius is 12.9 cm); each layer is assembled by means of double-sided silicon wafers. The detector is subdivided into three identical barrels, which are aligned along the beamline (see fig. 2.6), in order to provide adequate z coverage (± 45 cm from the nominal interaction point).

One side of all layers is characterized by axial microstrips, providing $r-\phi$ information; the other side of the layers, conversely, supplies $r-z$ information by means of stereo microstrips. Microstrips belonging to layers[5] 0, 1 and 3 have a 90° stereo angle; this angle reduces to 1.2° for the remaining layers.

SVX II provides information to a dedicated trigger system (SVT – see § 3.1.2), that performs a fast search for displaced tracks (*id est* tracks not originated in the primary vertex).

Layer 00

Layer 00 is a single-sided layer of silicon crystals placed on the outer side of the beam pipe at a radial distance of ~ 1.5 cm from the beamline (see figs. 2.8 and 2.9); it supplies $r-\phi$ information only, but its position makes of it the perfect tool for increasing the track impact parameter resolution of the tracking system.

[5]Layers are numbered from 0 to 4 according to an 'inside-out' order.

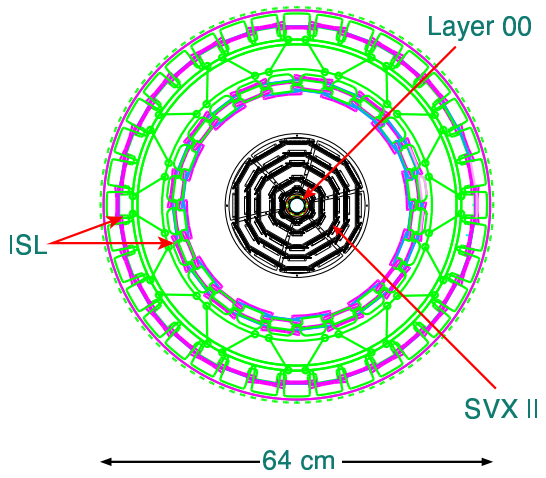

Figure 2.8: *r–φ view of silicon detectors.*

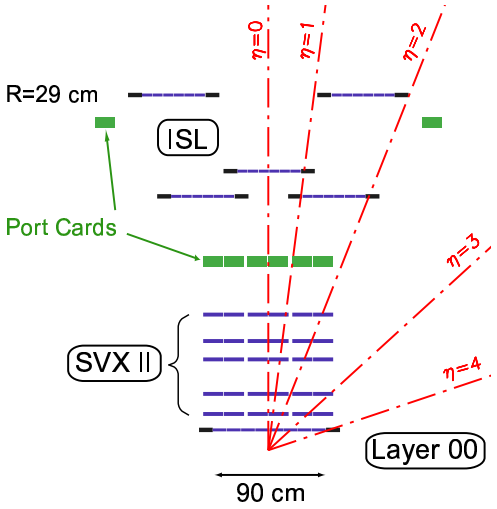

Figure 2.9: *r–z view of silicon detectors.*

2.2.2 The time of flight

Placed in the gap between the magnet and the outer wall of the COT, the detector for time of flight measurement [2] is essentially an array of scintillator bars $\sim 3\,\mathrm{m}$ long and $\sim 4\,\mathrm{cm}$ thick; their section is trapezoidal in shape, in order to better fit the cylindrical cavity they are supposed to fill, at the same time reducing the uninstrumented regions (*cracks*). Their average width, on the other hand, turned out to be $\sim 4\,\mathrm{cm}$ in order to accomplish occupancy requirements.

Scintillator bars are read at both ends by photomultiplier tubes, both providing a time of passing and a pulse-height; the comparison of the readings performed at each end provides an estimate of the z-coordinate of the charged particle that traversed the scintillating material, which is then used for matching the time of flight determination – leading to particle identification – to a track reconstructed by the tracking system. The time of flight estimation is performed computing the time interval between the interaction and the signal in the scintillators.

2.2.3 The calorimeters

The CDF calorimetry system consists of inner electromagnetic and outer hadronic sections, both segmented according to a common scheme which relies on azimuthal wedges ($\Delta\phi = 15^{o}$), each wedge corresponding to an array of towers projecting towards the geometrical center of the detector. The result is a cylindrical barrel providing almost full azimuthal acceptance and $|\eta| < 3.64$ coverage.

The purpose of calorimetry is performing measurements of the energy[6] depositions released by charged and neutral particles leaving the tracking and magnet regions, as well

[6]Although calorimetry measurements provide estimates of $E = E_L + E_T$ (where E_L, E_T are defined with respect to the z axis), only transverse energy components (E_T) are relevant at hadron colliders. This is because the total energy of hard scattering processes emerging from $p\overline{p}$ collisions is variable due to the Bjorken x-dependence carried by the energy of each colliding parton.

as providing information about the missing transverse energy; as will be explained in the next chapter, this detector is of crucial importance also for *cluster* and *jet* reconstruction.

The central and endwall calorimeters

The central and endwall calorimeters, providing acceptance in the $|\eta|<1.1$ region ($|\eta|<1.2$ for hadronic section), have been retained almost unchanged from Run I, the only major upgrades being related to readout electronics. Each tower, corresponding to $\Delta\eta\times\Delta\phi=0.11\times15^{o}$, is a an independent sampling system consisting of alternating layers of lead and scintillator, backed by an iron-scintillator sandwich. The former, contributing a total thickness of ~ 18 radiation lengths[7] (X_0), is dedicated to the electromagnetic energy component, while the latter, corresponding to ~ 5 interaction lengths (λ_0), provides a measure of the hadronic energy.

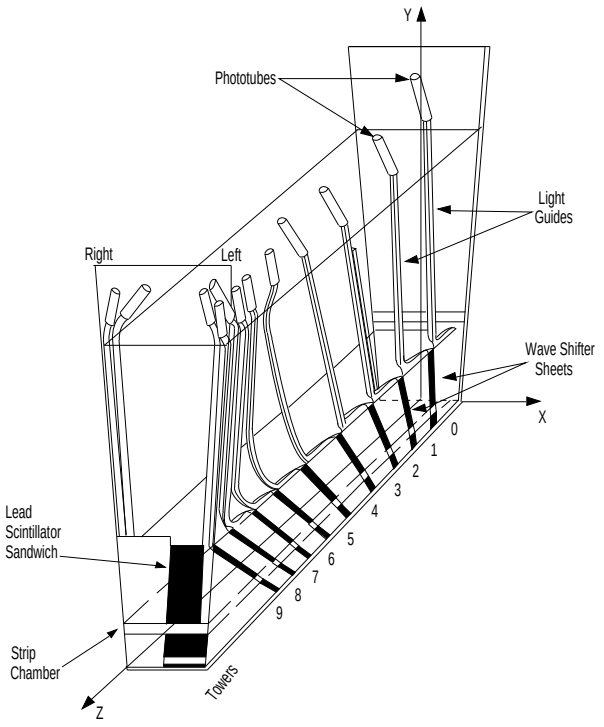

Figure 2.10: *Perspective view of central calorimeter half-wedge.*

Light pulses recorded in the various scintillator tiles are collected by wave length shifters and carried outside the detector volume by light guides, where they are read by photomultiplier tubes. A perspective view of a central calorimeter half-wedge ($\eta > 0$) is depicted in fig. 2.10, where both the arrangement in projective towers and the light-gathering system (only the electromagnetic system is sketched) are visible. Energy resolutions achievable by this detector are influenced by their mechanical structure (sampling) and by stochastic fluctuations due to the photomultipliers response; global estimates assign resolutions of $14\%/\sqrt{E_T[\mathrm{GeV}]}$ for electromagnetic and $75\%/\sqrt{E_T[\mathrm{GeV}]}$ for hadronic towers.

Two position detectors are included in each wedge of the central electromagnetic calorimeter:

Shower Maximum Detector: embedded within the lead-scintillator sandwich at a radial depth of $r=184\,\mathrm{cm}$ [8], in correspondence to maximum shower development, two-dimensional strip-wire chambers (CES, for Central Electromagnetic Strip chamber) provide position and pulse-height information about electromagnetic showers by measuring their charge deposition. Chamber geometry is usually described in terms of the local wedge-coordinate system defined in fig. 2.10: each half-wedge[9] hosts two CES modules, providing coverage in the $z=6.2\div121.2\,\mathrm{cm}$ and $z=121.2\div239.6\,\mathrm{cm}$ regions; chambers are segmented along the z direction in strips having an approximate pitch of 2 cm, leading

[7] Equivalent to $\sim$1 interaction length.

[8] Equivalent to $\sim 5.9X_0$ (including coil, which contributes by $\sim 1X_0$).

[9] As previously mentioned, a half-wedge subtends a $\Delta\phi=15^{o}$, $\eta\gtrless 0$ region.

to a total of 64 strip channels in each chamber module. A 32-wire array is coupled to each chamber module; wires, with a $\sim 2.5\,$cm spacing, are parallel to the z direction, providing in this way a 90^o reading of the charge deposition with respect to strips. As will be discussed in the next chapter, CES can contribute effectively to increase the purity of electromagnetic objects: besides providing a finer azimuthal segmentation than calorimeter towers, CES can reject early hadronic showers occurring in the outer portion of the electromagnetic towers.

Preradiator: (CPR) mounted in front of the innermost face of the electromagnetic towers, the preradiator consists of two wire chamber modules for each half-wedge; in practice, this device follows the same structure and wire arrangement provided to the CES wire chamber, the only difference being related to shorter wire spacing ($\sim 2.2\,$cm) to fit the projecting wedge profile and slightly reduced η-acceptance ($z = 7.14 \div 119.7\,$cm and $z = 123.5 \div 235.76\,$cm delimit the boundaries of active regions). The preradiator collects the charge depositions released by showers that initiate in the tracking or coil material; the information provided by this detector can be used for a further background rejection on selecting electrons or photons (which can be better separated from pions according to their average larger deposition in the CPR).

Although calorimeter response is fast enough to meet the tighter time requirements imposed by Run II, wire chambers associated to CES and CPR may need to undergo integration over several beam crossings; this, however, should not be a problem since the high granularity exhibited by these devices guarantees a low detector occupancy.

The plug calorimeters

The active material for the Run I plug calorimeter consisted of proportional tubes, whose time response could not be matched to the operational conditions of Run II; for this reason, this detector has been substituted by a new unit, whose r–ϕ section is depicted in fig. 2.11, which also shows its relative position within CDF. From a functional point of view, the upgraded plug calorimeters essentially follow the scheme of the central calorimeter, with both the electromagnetic and hadronic sections relying on alternating layers of absorbing material (lead and iron respectively) and scintillator tiles, leading to a thickness of $\sim 21 X_0$ ($\sim 1\lambda_0$) and $\sim 7\lambda_0$ in the two cases. As for the central calorimeter, scintillators are read out by photomultiplier tubes (placed on the outside of each end plug) receiving the light pulses through a complex of wave length shifters, which collect the signals from the tiles, and light guides.

The upgraded plug calorimeters provide an acceptance throughout the region $1.10 < |\eta| < 3.64$. While the central calorimeter is characterized by almost constant $\eta - \phi$ granularity, both η and ϕ segmentation of the plug are variable: according to increasing η, $\Delta\eta$ ranges from 0.10 to 0.64 on approaching the beamline; at the same time, the azimuthal segmentation decreases from 7.5^o to 15^o at the boundary between the fifth and the fourth highest η towers.

Also in this case, the energy resolutions are the result of limited sampling performed by scintillating tiles and stochastic fluctuations affecting the photomultipliers; electromagnetic and hadronic resolutions, respectively $16\%/\sqrt{E[\mathrm{GeV}]}$ and $80 \div 90\%/\sqrt{E[\mathrm{GeV}]}$, have been measured for single electrons and pions.

A **Shower Maximum Detector** (SMD) is embedded in correspondence of a radial depth of $\sim 6 X_0$; instead of relying on the wire-strip chamber technique used for the central

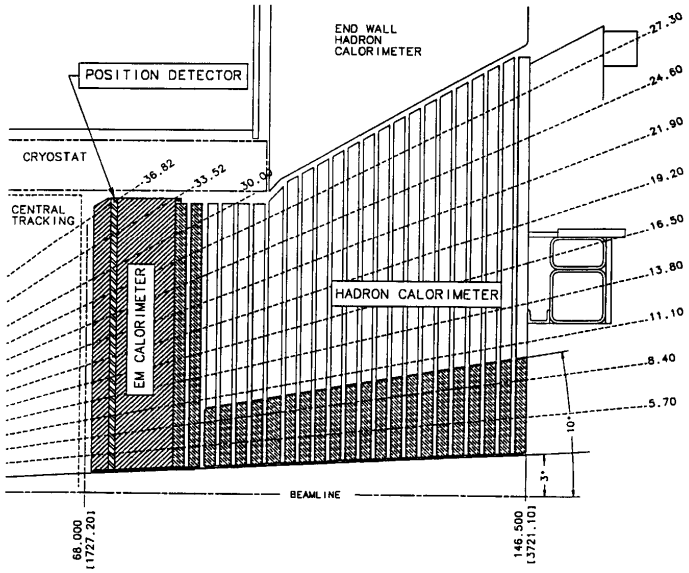

Figure 2.11: *r − z view of plug calorimeter system.*

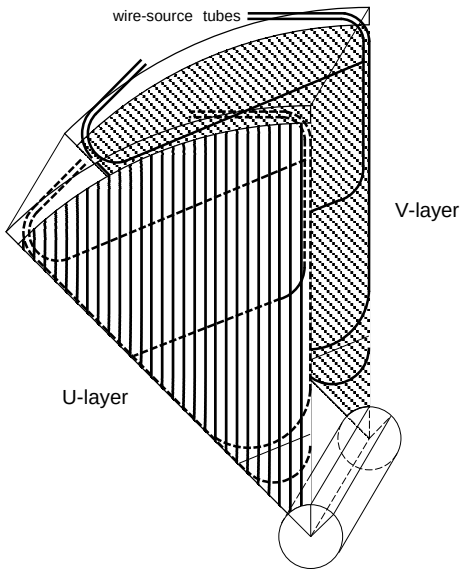

Figure 2.12: *Perspective view of plug shower maximum detector.*

calorimeter, in this case arrays of scintillating strips have been chosen. The SMD is divided in eight 45° azimuthal sectors[10], each consisting of two layers (named U and V) of 5 mm pitch scintillating strips; strips belonging to the same layer are oriented along a common direction coincident with one of the two sector radial boundaries (see fig. 2.12), in such a way that U and V strips form an angle of 45° among them, which enables two-dimensional position measurements. Furthermore, in order to reduce detector occupancy, on the basis of which the strip pitch has been optimized, a η segmentation is provided to strips (visible in fig. 2.12).
Light signals in this detector are collected by wave length shifter fibers embedded in the strips and read by means of photomultiplier tubes placed at the rear of the plug calorimeter.

2.2.4 The muon system

Muon detectors are arranged in such a way to enclose the whole CDF detector (see fig. 2.2); this arrangement is aimed at exploiting the fact that, being muons very penetrating particles, a natural separation from other charged tracks arises from inner detector shielding.

The CDF muon system has undergone two substantial upgrades for Run II: first, a global increase in the acceptance, essentially achieved by extending Run I coverage to uninstrumented regions (see fig. 2.13); second, the forward muon detection will rely on the improved tracking capabilities, which will allow momentum determinations based only on the central solenoidal field. For this reason, during Run II there will be no need for the toroidal fields: instead, the steel toroids will provide mechanical support for the new forward detectors as well as adequate shielding. Furthermore, toroids will be pushed towards the central detector for increasing the acceptance also in the forward regions.

[10] Sectors segmentation are matched to tower boundaries.

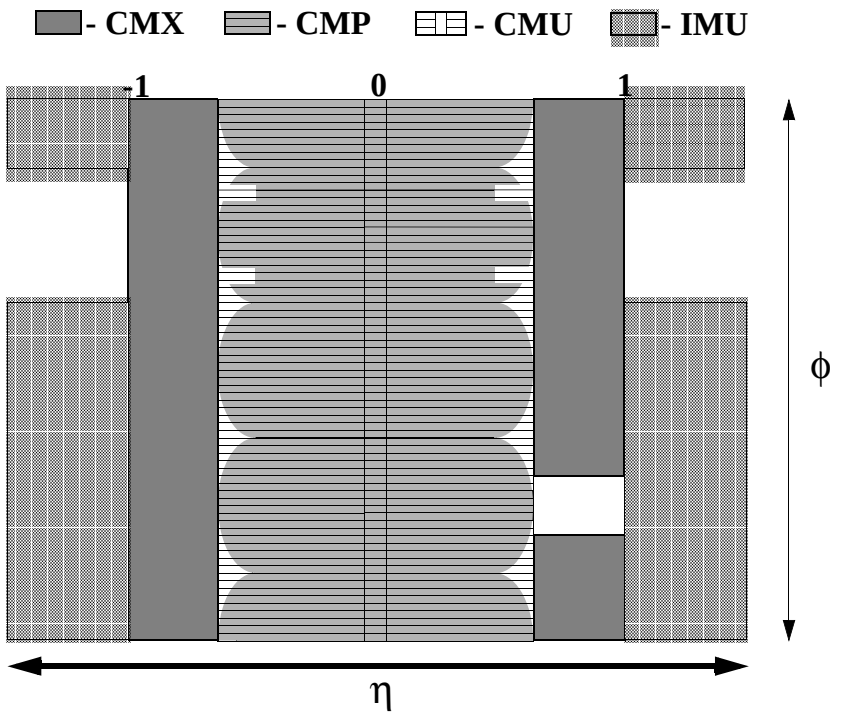

Figure 2.13: *Muon system $\eta-\phi$ map.*

The muon system consists of four subdetectors:

Central Muon Chambers (CMU), placed immediately outside the hadron calorimeter, will substantially remain unchanged from Run I: they consist of 144 modules each containing 16 6.35×2.68 cm rectangular drift cells stacked in four layers with a small azimuthal offset; three such modules cover a half-wedge of the calorimeter, providing a global $|\eta|\lesssim0.6$ coverage. Muons with $P_T\gtrsim1.5\,\mathrm{GeV}/c$ are able to traverse the whole calorimeter region and leave a signal in the CMU; their position can be determined by merging the information coming from drift times (supplying ϕ) with a z coordinate estimated on the basis of charge division. Drift tubes will be driven in proportional mode with a maximum drift time of 800 ns.

Central Muon Upgrade (CMP) consists of a second set of four staggered layers of 2.5×15 cm drift tubes arranged behind an additional 60 cm of steel[11] according to a rectangular geometry (*id est*, they form a box around the central detector); the mismatch between the inner cylindrical structure and the outer box results in a curved acceptance boundary, which is evidenced in fig. 2.13. Muons must have $P_T\gtrsim2.2\,\mathrm{GeV}/c$ for reaching the CMP. Similarly to CMU, drift tubes will be run in proportional mode (maximum drift time of $1.4\,\mu$s), but, on the contrary, they will not provide z information.

On the outer surface of CMP a layer of rectangular scintillator counters[12] is installed in such a way that each scintillator tile covers two drift cells in width and half a cell in length.

CMP acceptance has been increased by 17% for Run II.

Central Muon Extension (CMX) provides coverage in the $0.6\lesssim|\eta|\lesssim1$ by means of arrays of drift tubes arranged in conical sections, which are then positioned at each end of

[11] Provided by the magnetic field return yoke.

[12] These form the Central Scintillator Upgrade, or CSP.

the central detector; CMX array geometry follows the CMP scheme. Drift tubes are embedded within two layers of scintillator counters[13]; four scintillator tiles cover a $\Delta\phi = 15^o$ range, with tiles being staggered between them in the two layers. Drift tubes, achievable for muons with $P_T \gtrsim 1.4\,\mathrm{GeV}/c$, are operated in proportional mode with maximum drift time of $1.4\,\mu$s and provide ϕ information; z information, in the other hand, is obtained from scintillator timing.
CMX will benefit an improved acceptance by 45% in Run II.

Intermediate Muon Detectors (IMU) extend muon identification up to $|\eta| \leq 2$, providing at the same time trigger capabilities for $|\eta| \leq 1.5$; placed on the outer surface of each toroid, its main structure consists of a barrel of drift chambers (run in proportional mode with a maximum drift time of 800 ns) coupled with scintillator tiles; the arrangement follows the CMP/CSP scheme. These detectors are reachable by muons with $P_T \gtrsim 1.4 \div 2.0\,\mathrm{GeV}/c$.

The slow response of the muon system can be overcome by exploiting their high granularity, which, in principle, enables integration of signals collected by muon chambers over several beam crosses; this, however, is a feasible possibility only in case a strong reduction of the detector occupancy can be achieved. During Run I, it was observed that most ($\gtrsim 95\%$) of the ionization detected in the muon system was originated by the Main Ring rather than by $\mathrm{p\overline{p}}$ collisions and TEVATRON beam halo; in Run II, this situation is expected to be much better, since, having the Main Ring substituted by the Main Injector and provided stronger shielding from beam halo to the most exposed devices (CMX), should reduce the activity – and, therefore, the occupancy – of muon detectors. These side-improvements, together with the detector upgrades described above, are expected to produce an effective enhancement in the performances of the muon system in Run II.

2.2.5 The trigger system

The renewed characteristics of the detector, which – as described above – have been required by new running conditions of the TEVATRON, imply that also data acquisition (DAQ) and trigger systems need to undergo suitable upgrades.

As previously mentioned, the major change affecting data taking in Run II consists of reduced time between beam crossings; anticipating what will be described and discussed in the next chapter, a trigger system has to be employed whenever the operation of storing an event on tape requires a longer time than the time between two beam crossings. During Run I, this time interval, $3.5\,\mu$s, was long enough to permit a processing of the calorimetric signals, providing a Level 1 trigger decision before the occurrence of the next event. In the Run II scenario, where bunch spacing will be reduced down to 132 ns, this will not be possible. At the same time, the increased instantaneous luminosity regime will demand more sophisticated trigger primitives to provide effective rate reduction. The only solution compatible with the new operational conditions consists in storing every incoming event in a memory buffer, using the time recovered from fast rejections for providing adequate processing to the remaining events. Due to the fact that the Run I CDF configuration fails to match the operational conditions of the machine, the whole trigger and DAQ systems have to be entirely replaced for Run II.

[13] Central Scintillator Extension or CSX.

A simplified picture of the CDF trigger data flow is depicted in fig. 2.14, where the three-level architecture of the trigger system is evidenced. A Level 1 latency time of $5.5\,\mu$s has been chosen for allowing readout, data transmission and trigger processing to occur; the magnitude of this time interval defines the dimension of the memory buffers, which, for time saving, are located directly on the readout boards of the detector subsystems: given the beam spacing of 132 ns, a 42-event memory stack is required. Events passing the Level 1 trigger requirements are then pipelined into one of four onboard Level 2 buffers[14]; the expected average time for processing one event sets the Level 1 trigger bandwidth, *id est*, the maximum rate of events that can be accepted[15]. In order to keep dead-time within acceptable values ($\lesssim 10\%$), each separate Level 2 buffer is connected to a two-step pipeline, each step having a latency time of $10\,\mu$s [3]:

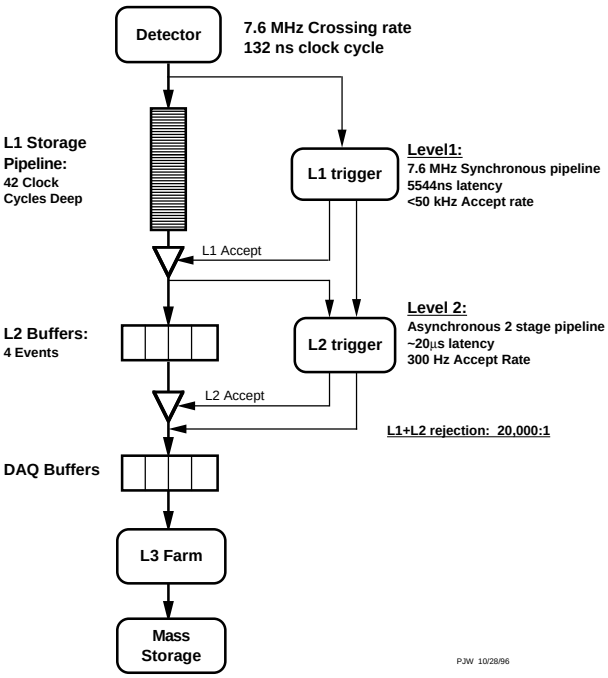

Figure 2.14: *Buffering and pipelining.*

step 1: single detectors responses are analyzed;

step 2: the combination of the outcome of step 1 are merged and trigger decisions are cast on a *whole-event* basis.

Events passing Level 2 are transmitted to a PC farm, where events are fully reconstructed; this happens at Level 3, after which, if an event is accepted, it is permanently stored.

[14]Note that at Level 2 processing is an asynchronous process, as opposed to Level 1, where events are analyzed in the same order as they occurred.

[15]Trigger bandwidths will be considered quantitatively in the next chapter.

Bibliography

[1] F. Abe *et al.* (The CDF II Collaboration), *"The CDF II Detector Technical Design Report"*, FERMILAB-PUB-96-390-E, Oct 1996.

[2] The CDF Collaboration, *"A Time of Flight System for CDF"*, CDF internal note 2573, Feb 1994.

[3] H. Frisch *et al.*, *"Conceptual Design of a Deadtimeless Trigger for the CDF Trigger Upgrade"*, CDF internal note 2038, Dec 1994.

Chapter 3

Event reconstruction

At $\sqrt{s}=2\,\mathrm{TeV}$, the inelastic cross section for $\mathrm{p\overline{p}}$ scattering is 56 mb, which, in terms of rate, means 5.6 millions collisions per second for a typical instantaneous luminosity of $10^{32}\,\mathrm{cm^{-2}s^{-1}}$ expected for Run II. This value has to be compared with the typical rate scale for processes of high interest at hadron colliders, respectively $8\times10^{-4}\,\mathrm{Hz}$ for top (corresponding to $\sigma=7.6\,\mathrm{pb}$ for $M_{\mathrm{t}}=175\,\mathrm{GeV}/c^2$ [1]) and $3\times10^{-5}\,\mathrm{Hz}$ for (SM) Higgs production (corresponding to $\sigma=0.262\,\mathrm{fb}$ for $M_{\mathrm{H}}=120\,\mathrm{GeV}/c^2$).

The overwhelming abundance of $\mathrm{p\overline{p}}$ collisions, therefore, requires data-taking at an hadron collider detector being controlled by a mechanism that filters out all events which do not present the characteristic signatures of the physical processes one is interested in. This mechanism is known as trigger system and essentially consists of a collection of specific hardware modules driven by speed-optimized software capable of performing a selection on the basis of pattern recognition and reconstruction.

Events which are selected by the trigger system are saved permanently on a mass storage and subsequently fully reconstructed offline.

3.1 Trigger primitives

The CDF trigger system is organized according to a three-level architecture; each level output is feeded as input into the next level. The underlying philosophy of this procedure consists essentially in reducing the rate at lower levels by means of very conservative requirements aimed mainly at reducing the dead time, enabling in this way more sophisticated selections to be performed at higher levels.

For each level, a set of primitives, essentially physics objects directly measured by the detector (such as energy depositions in the calorimeter) or obtained from them by running some algorithm (such as jets), is defined. According to the signal one wants to isolate, specific requirements are applied to a subset of primitives available at a given level; this sets the trigger for that level.

The maximum allowed rate for a given level (which is often referred to as 'bandwidth') reflects the hardware capability of buffering and, at Level 3, storing permanently the collected events in the unit time; table 3.1 summarizes some of the assumed boundary conditions relative to two different scenarios at Run II.

$\int \mathcal{L}dt$ regime	Medium	High
$\sqrt{s}$	2.0 TeV	2.0 TeV
$\mathcal{L}$ [$\mathrm{cm}^{-2}\mathrm{s}^{-1}$]	1×10^{32}	2×10^{32}
Number of bunches	36	108
Bunch-cross time [ns]	396	132
Mean interactions per crossing	2.3	1.5
Level 1 bandwidth	40 kHz (400 μb)	40 kHz (200 μb)
Level 2 bandwidth	300 Hz (3.0 μb)	300 Hz (1.5 μb)
Level 3 bandwidth	75 Hz (750 nb)	75 Hz (375 nb)

Table 3.1: *Run II nominal boundary conditions [2].*

Once triggers are built for each level, links across different levels are established by defining trigger paths; a trigger path identifies a unique combination of a Level 1, a Level 2 and a Level 3 trigger; in other words, a trigger path establishes a logic AND between selection procedures at different levels.

Datasets (or data streams) are then formed by merging the data samples collected via different trigger paths; hence, datasets are defined by a logic OR between trigger paths. This definition of dataset enables a monitoring of the cross section of individual triggers within the same trigger path in terms of luminosity variations and detector noise without loss of information, since for each event its 'trigger history' is recorded.

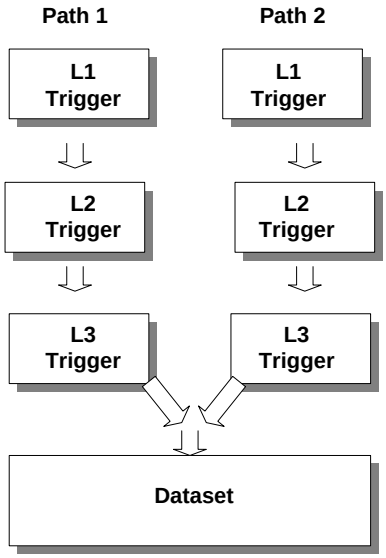

Figure 3.1: *Schematic diagram of trigger primitives, paths and datasets.*

A graphical representation of the CDF trigger layout is depicted in fig. 3.1; in the following, a list of CDF trigger primitives will be presented for each of the three trigger levels.

3.1.1 Level 1

Level 1 trigger primitives have been conceived on the basis of a very simple mechanism, aimed at minimizing the dead time required for making a decision: finding simple physics objects and, at most, counting them. The nominal dead time is $\sim$5.5 μs. They can be

divided into four categories, according to the detector the primitives are based on, and are completely hardware-based.

Calorimetry

Calorimetry primitives can be subdivided into two classes:

object primitives: energy deposits detected[1] in the central and plug calorimeter weighted by an appropriate $\sin\theta$ factor. Within Level 1, towers are not considered individually, but merged in pairs along η; the so defined primitives are addressed as 'trigger towers' and are $\Delta\eta \simeq 0.2 \times \Delta\phi = 15^{o}$ wide[2]; the result is a 24×24 $\eta - \phi$ map of the calorimeter region extending to $|\eta| < 3.6$. Electromagnetic (EM) and total (EM+HAD) contributions are treated independently;

global primitives: transverse energy (EM+HAD) deposits recorded in all trigger towers above a threshold[3] are involved into two different sum procedure:

- ◇ all $\eta - \phi$ towers are summed together into the definition of ΣE_T;
- ◇ each set of 24 modules corresponding to a ϕ-wedge are added together and the $\Sigma E_{Tx} = \Sigma E_T(\phi)\cos\phi$, $\Sigma E_{Ty} = \Sigma E_T(\phi)\sin\phi$ sums computed; from them, $\not\!\!E_T$ is obtained.

Correspondingly, object and global triggers can be defined; in both cases the trigger requires a comparison between a detected transverse energy (single trigger tower E_T and E_T^{had}/E_T^{em}, ΣE_T and $\not\!\!E_T$) and a threshold (EM and EM+HAD thresholds can be set independently). In the case of object triggers, the number of towers above threshold is counted; this is done by a 1-bit sum ($0, \geqslant 1$) for single-object triggers and by a 2-bit sum ($0, 1, 2, \geqslant 3$) for di-object triggers.

XFT

XFT is the acronym of eXtremely Fast Tracker and stands for a hardwired algorithm for track finding. A similar device (CFT, Central Fast Tracker) was in use during Run I for identifying high-momentum charged tracks in the CTC (Central Tracking Chamber). For Run II, a new fast track finder has been designed for the COT. The guiding idea, on the other hand, remains the same: performing a fast $r - \phi$ track-reconstruction and returning P_T, ϕ_0 (the azimuthal direction of the track at the point of minimum approach with respect to the beam axis) and extrapolated position at the outer layer of the CTC of the fitted track in case of success.

The XFT standards have been established in order to at least reach and possibly overcome the performances exhibited by the CFT; on this basis, the main design goals are[4]:

---

[1] Although calorimeter responses are digitized into 10-bit words, allowing a precision of 125 MeV, at Level 1 only a precision of 250 MeV is available.

[2] Except for the highest $|\eta|$ towers, whose coverage is $\Delta\eta \simeq 1$.

[3] A 1 GeV threshold has been set on the basis of efficiency maximization studies computed on a $W \to e\nu_e$ signal.

[4] The corresponding measured performances for CFT are reported in brackets for comparison.

- ◇ track-finding efficiency greater than 96% for tracks with $P_T > 1.5\,\mathrm{GeV}/c$ ($\sim$70% for tracks with $P_T \gtrsim 2.2\,\mathrm{GeV}/c$, $\sim$100% for $P_T \gtrsim 3.5\,\mathrm{GeV}/c$);
- ◇ $\delta P_T/P_T^2 < 2\%\ (\mathrm{GeV}/c)^{-1}$ ($\delta P_T/P_T^2 < 3.5\%\ (\mathrm{GeV}/c)^{-1}$);
- ◇ double fake-rate rejection with respect to the CFT.

A good resolution on the fitted track ϕ_0 ($\delta\phi_0 \lesssim 8\,\mathrm{mrad}$) is required if the XFT output is to be used as a seed for the Silicon Vertex Tracker, a Level 2 trigger algorithm that will be described later in this chapter.

The XFT works on the basis of a two-step procedure: first, track segments are identified in each axial superlayer of the COT (here numbered between 1 and 4); a track segment is searched for by a pattern recognition algorithm among all possible hit patterns achievable by a track with $P_T \geqslant 1.5\,\mathrm{GeV}/c$ in the 12 layers of sense wires of four adjacent COT cells (see fig. 3.2). Track segments (*pixels*) – defined by their ϕ position at superlayer 3 and slope[5] – are then linked together into tracks. The starting point of the linking procedure is a valid pixel in superlayer 3, corresponding to a 1.25°-wide COT slice (see fig. 3.3); starting from this pixel, all combinations of track segments (*roads*) compatible with a $P_T \geqslant 1.5\,\mathrm{GeV}/c$-track hypothesis are computed through different superlayers. Among all roads found in each 1.25° COT slice, the one with the greatest number of associated pixels[6] and highest P_T is returned by the algorithm together with its charge, P_T and ϕ at superlayer 3.

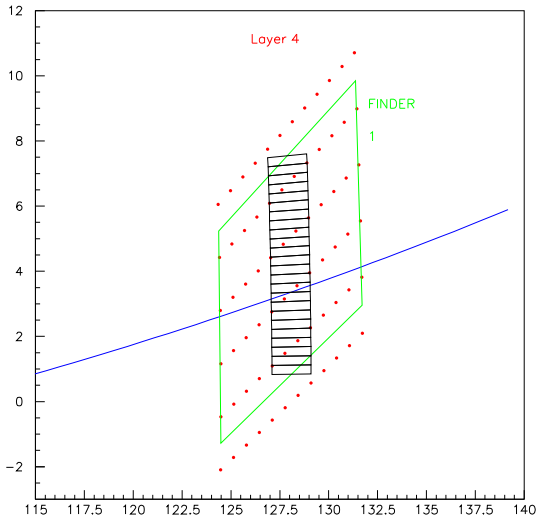

Figure 3.2: *Graphical representation of* XFT *track segment finder.*

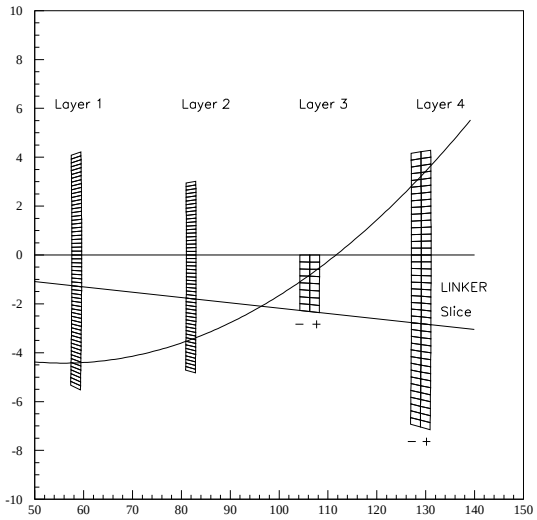

Figure 3.3: *Graphical representation of* XFT *track segment linker.*

Once the tracks have been found, their information is sent to the extrapolation unit (XTRP), whose task primarily consists in mapping the XFT tracks by means of lookup tables onto muon and electron primitives found by other Level 1 trigger processors; in other words, the XTRP provides an extrapolation of each XFT track to the central calorimeter

[5]Slope is determined by the two outer superlayers only.

[6]The possibility of a three-out-of-four match is permitted for 'short tracks', which do not reach the outer superlayer; large $|\eta|$ tracks are included into this definition.

wedges (15° wide) and to the muon system (CMU and CMX). At the same time, for each track, the ϕ, P_T information is made available to Level 2 processors, such as SVT.

Furthermore, the XTRP can generate itself a Level 1 trigger accept, according to number of tracks, their topology and P_T threshold.

Muons

The Level 1 muon trigger is aimed at providing single and dimuon objects for the Level 1 trigger decision; a Level 1 trigger muon object is obtained by matching a tracking primitive (*id est*, a XFT track) to a muon primitive.

The definition of muon primitive depends on the specific muon detector type; for scintillators (CSP, CSX), a muon primitive corresponds either to single-hits or to coincidences of hits. Differently, for wire chambers (CMU, CMP, CMX), a cluster of hits (*stub*) is searched for; in the case of CMU, CMX, a stub is defined whenever a coincidence, within a given time[7], is achieved between at least two hits collected in projective wires, *id est*, in wires belonging to different radial layers. For CMP, on the other hand, a pattern of hits in a tube stack consistent with a traversing track is required for stub definition. A further muon primitive is supplied by the hadron calorimeter, which is capable of signalling the passing of a minimum ionizing particle in each trigger tower.

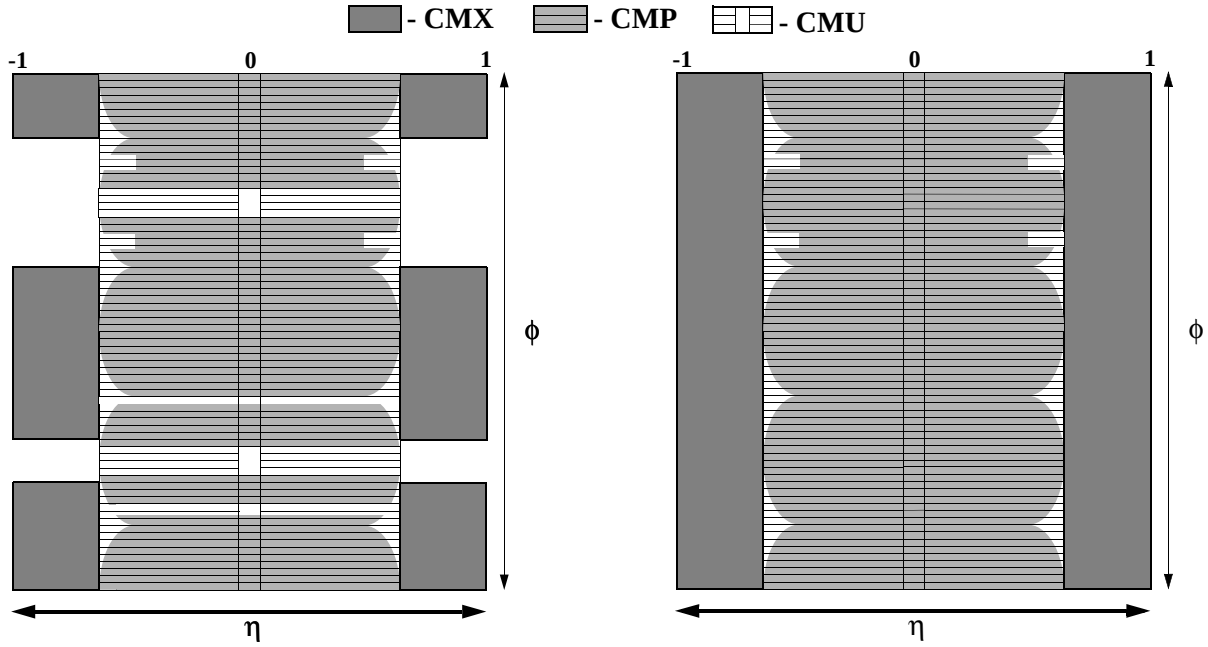

Figure 3.4: *Comparison between* CDF *central muon system* $\eta - \phi$ *map: Run I (left) and Run II (right) configurations.*

Two major improvements distinguish the Run II from the Run I muon trigger:

- ◇ an increased coverage for CMP (+17%) and CMX (+50%) – see fig. 3.4 –, which results both in an augmented purity of the sample collected by combining CMU and CMP primitives and in an enhanced global acceptance;

[7]The time interval is implicitly connected with a lower P_T bound; therefore, P_T requirements for stubs are achieved by adjusting the time window in the stub definition.

- ◇ central tracking information from the XFT-XTRP will be available already at Level 1, providing a more effective fake-rate rejection;

As previously mentioned, XFT tracks and muon stubs information can be merged into muon objects by means of a matching between trigger primitives; these procedures consists of a $r-\phi$ track-stub match, which at Level 2 exploits only half of the full detector azimuthal granularity[8] ($\sim 1.25^o$), and, eventually, of a P_T-based match, since independent thresholds can be set on the P_T of the track and of the stub[9]. In order to avoid a double-counting when considering dimuon objects, at least an empty $\Delta\phi = 2.5^o$ segment is required between stubs.

Electrons

Electron triggers are formed in the same way as for muons; in this case, however, the electron-oriented primitives achievable at Level 1 are essentially the calorimeter towers which have been described in detail on pag. 53. A Level 1 electron trigger can be obtained requiring a trigger tower with an electromagnetic energy content above a certain threshold to be matched to a XFT track fulfilling some P_T requirement. Rate constraints effectively influence the possibilities one can pursue in choosing thresholds: in particular, one can hope to lower the energy/momentum thresholds only by considering a two-electron topology in order to recover an acceptable trigger rate.

3.1.2 Level 2

Selection procedures at Level 2 become more sophisticated than at Level 1, in the sense that, while Level 1 is primarily devoted to rate reduction, at this point the less stringent time constraints ($\sim 20\,\mu$s) together with considerably lower rate, enable to concentrate on the true aim of a selection: the improvement of the signal to background ratio, a fundamental quantity for isolating a certain physical process.

If the core of the tools available at Level 2 is still given by hardwired procedures, a set of time-optimized software can be integrated in the trigger system.

Calorimetry

One of the most common features of high energy hadron collisions final states is jets: they originate from the hadronization of energetic partons, when, as a consequence of the Lorentz boost, the particles produced in such a process tend to be compressed into a narrow region of phase-space.

Since in general jets are not expected to be fully contained into a single trigger tower, the energy threshold for a Level 1 jet trigger requirements has to be be set at a considerably lower value than the typical jet energy in order not to loose efficiency. This, however, implies trigger rates which are too high to be fed directly into Level 3.

[8] The 2.5^o azimuthal resolution of the Level 1 track-stub match in Run II is twice the exploited resolution in Run I, thanks to the improved performances of XFT with respect to CFT.

[9] However, it should be kept in mind that the precision on the P_T measurement achieved by the differential timing in the muon chambers is lower than the corresponding quantity measured by the XTRP.

An effective rate reduction can be achieved at Level 2 by considering, instead of single trigger tower energies[10], the energy associated to clusters of contiguous trigger towers. The definition of clusters within an event requires an algorithm (*cluster finder*) whose working principle – essentially unchanged from Run I – can be explained in terms of four steps, a graphical representation of which can be found in fig. 3.5.

Step 1 Two energy thresholds must be fed to the cluster finder: the *seed* threshold will define which trigger towers have to be used as a starting point by the algorithm; the *shoulder* threshold, on the other hand, essentially establish the duration of a recursive procedure which will be described in the third step.

Step 2 All trigger towers with energy content above the seed threshold are identified and recorded as 'seed towers'; when all seed towers have been found, a second loop is performed on the remaining trigger towers in order to tag the 'shoulder towers', that is, the trigger towers whose energy exceeds the shoulder threshold.

Step 3 Iterative procedure starting from the seed tower that, among all seed towers with lowest η address (η_s), has the lowest ϕ address (ϕ_s): a signal is sent to the four $\eta = \eta_s \pm 1$ and $\phi = \phi_s \pm 1$ neighbouring trigger towers; if a signalled trigger tower is a shoulder tower[11], then, after being flagged as 'found', it signals in turn its three neighbouring trigger towers. The procedure is repeated until no more contiguous shoulder towers are found.

Step 4 Step 3 is repeated for all seed towers not being flagged as 'found' in previous iterations.

When the procedure comes to an end, clusters are identified with the groups of contiguous trigger tower that have developed around a seed tower; each cluster is assigned an energy equal to the sum of the energies[12] of all trigger towers belonging to the same group. The $\eta - \phi$ position of each cluster is then identified with the $\eta - \phi$ position of the seed tower which initiated the iterative procedure.

Within each event, the cluster finder procedure will be performed for each set of *seed, shoulder* thresholds (*pass*) that has been defined; in this way, within the same event, different topologies will be returned according to the typology of the clustering; the four passes that have been defined for Run II are:

- ◇ **type 1:** $E_T^{em}(seed) = 3.0\,\mathrm{GeV}$, $E_T^{em}(shoulder) = 1.0\,\mathrm{GeV}$ and $E_T^{had}(seed,shoulder) = \infty$ for low-P_T electron/photon;
- ◇ **type 2:** $E_T^{em}(seed) = 8.0\,\mathrm{GeV}$, $E_T^{em}(shoulder) = 7.5\,\mathrm{GeV}$ and $E_T^{had}(seed,shoulder) = \infty$ for high-P_T electron/photon;
- ◇ **type 3:** $E_T(seed) = 3.0\,\mathrm{GeV}$, $E_T(shoulder) = 1.0\,\mathrm{GeV}$ (both hadronic and electromagnetic components) for *jet* clustering;
- ◇ **type 4:** $E_T^{em}(seed) = 2.0\,\mathrm{GeV}$, $E_T^{em}(shoulder) = \infty$ and $E_T^{had}(seed,shoulder) = \infty$ for low-P_T electron in B-physics.

[10] Here and in the following, the term 'energy' indicates the E_T.

[11] Note that seed towers fulfill also the shoulder condition, unless the shoulder threshold is higher than the seed threshold.

[12] Electromagnetic and total contributions separately.

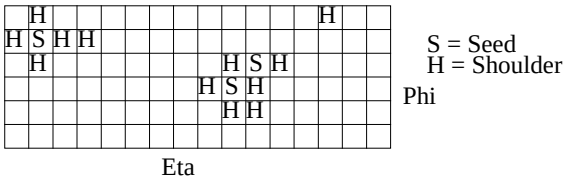

Step 1: seed and shoulder trigger tower tagging

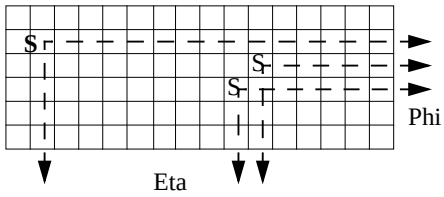

Step 2: seed and shoulder trigger tower eta-phi address recording

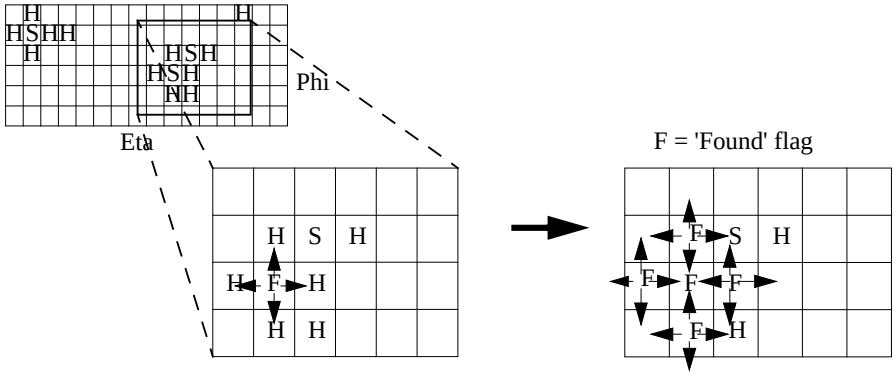

Step 3: contiguous shoulder towers are merged into clusters

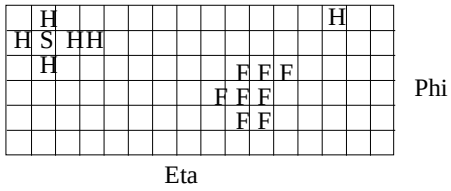

Step 4: trigger towers assigned to a cluster are excluded from further iterations

Figure 3.5: *Cluster finding procedure.*

In the case of type 4 clusters, the choice of an infinite electromagnetic shoulder threshold essentially corresponds to an implicit isolation requirement, since this procedure will lead to single trigger tower clusters. Isolation patterns can be explicitly required during clustering by asking the smallest of the sums depicted in fig. 3.6 to be less than a given threshold; however, for low-P_T electrons, produced for instance in the semileptonic decays of B or C-hadrons, a type 4 clustering is preferred, since, assuming the identified cluster correctly tags the tower struck by the electron, any further tower con-

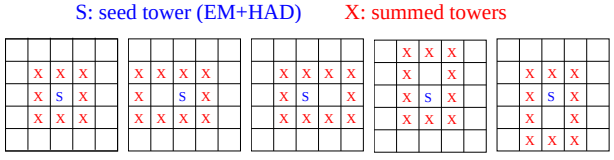

Figure 3.6: *Tower isolation patterns.*

tribution to the energy would dilute the information deposited in the calorimeter by the electron.

Exactly as for Level 1, Level 2 calorimetry primitives can be grouped into two categories:

object primitives: energy depositions[13] associated to hadronic (type 3) or electromagnetic (type 1, 2 and 4) clusters. Besides energy content and type, the information concerning clusters' position ($\eta - \phi$ address of seed towers) is stored, in order to enable combinations between calorimetric and tracking (XFT) primitives;

global primitives: the number of clusters, according to cluster type and energy, is available at Level 2. Global energy sums are cluster-based, *id est* they are obtained by summing the contributions of all cluster in an event; the total ΣE_T is performed over all type 3 clusters, while other ΣE_T observables can be defined considering different clusters subsets (for instance, on can compute the sum over all type 3 clusters with E_T greater than a given minimum threshold). Global non clusterized energies, on the other hand, are available at Level 1 only.

SVT

The study of B-physics, that is, processes involving b quarks, is of crucial importance at hadron colliders. On one hand, this kind of physics allows precision measurements on the Yukawa section of the SM – related to V_{CKM} and CP violation phenomena – by exploiting channels like $B^0_d \to J/\psi + K_S$, $B^0 \to \pi^+\pi^-$, $B_s \to \rho + K_S$; on the other hand, a high P_T b enhanced statistics translates into an improved knowledge on dijet mass resolution (for instance from $Z^0 \to b\bar{b}$), therefore enabling more control of energy-scale systematics. These studies are crucial for improvements in top physics measurements and searches for new phenomena ($H^0 \to b\bar{b}$).

Already during Run I, CDF, being equipped with a vertex detector, was capable of performing such studies, which essentially rely on reconstructing secondary vertices which are produced as a consequence of the remarkable B-hadrons decay length ($\sim 500\,\mu$m). However, during Run I this capability was confined to the offline analysis, while the tagging of the interesting events was referred to leptonic triggers; for this reason, the global efficiency on B-physics was drastically reduced, while some specific processes – like, for instance, $B^0 \to \pi^+\pi^-$, important for CP violations measurements – were virtually undetectable.

During Run II, this lack will be filled by the introduction of the SVT (Silicon Vertex Tracker [3]), a device for tagging displaced tracks already at trigger level; as previously mentioned, in fact, displaced tracks (*id est* with large impact parameter) can be interpreted as signals of the existence of secondary decay vertices of heavy flavoured objects. This tool provides a response by merging the information supplied by the new silicon vertex detector (SVXII) with the output of the Level 1 fast tracker (XFT, see pag. 53) in time for the Level 2 decision; in this way, the SVT will allow the collection of fully hadronic decay modes of B-hadrons as well as an efficiency enhancement for the semileptonic channels by enabling a lower P_T threshold for lepton tagging.

[13] At Level 2, the full calorimeter resolution of 125 MeV is exploited.

The working strategy of SVT is summarized in fig. 3.7. First, SVXII channels, grouped into 24 ϕ sectors (each one of the 12 azimuthal wedges is divided in two sectors according to the sign of z), are read out by 72 *Hit Finders*, which perform pedestal and bad-channel subtraction; once strip readout is completed, the *Hit Finders* search for hit clusters on each layer contained in the corresponding sectors, computing the centroid of each admissible cluster. Centroids represent the most likely intersection points between the trajectory of a track with each of the five[14] radial silicon layers of SVXII.

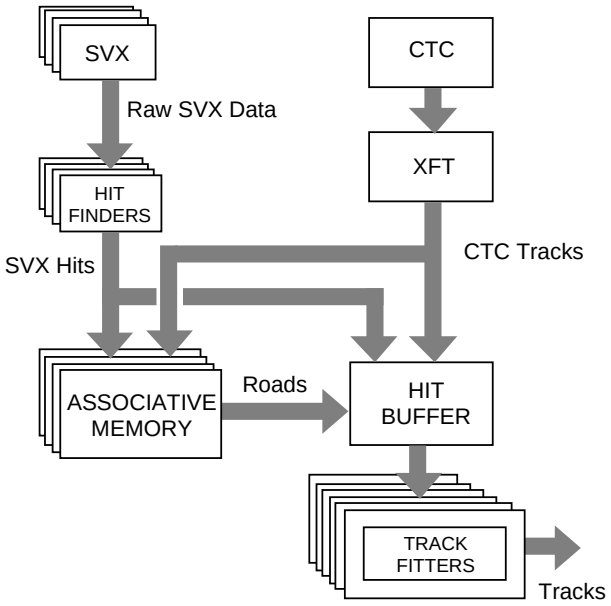

Figure 3.7: *The* SVT *data flow.*

Silicon clusters information is then transmitted to the *Associative Memory Sequencer* (AMS), which, at the same time, is fed with the XTRP output; in the AMS, a first, tentative association between clusters and XFT tracks takes place: this is done by lining up the clusters of a given ϕ sector with outer XFT tracks. Due to the large number of possible combinations arising from this procedure, each cluster is substituted by a *superstrip*, whose dimension ($250\,\mu$m) represents the best compromise between fake tracks rejection and cost. Then, the association between stacks of *superstrips* and XFT tracks is performed: each admissible combination, evaluated on the basis of lookup tables, defines a *road*, which represents a broad track.

Roads, each corresponding to a set of four SVXII clusters and an outer XFT track, are then sent to the *Hit Buffers*, which retrieve the full detector information (*id est* the single hits coordinates for each SVXII cluster and the two XFT track parameters[15]) to be used to fit the track to an arc of circumference trajectory and obtain the three parameters P_T, ϕ and d (impact parameter).

Simulations of the SVT trigger show that the resolutions $\sigma_d \simeq 35\,\mu$m (for $P_T > 2\,\mathrm{GeV}/c$), $\sigma_\phi \simeq 1\,$mrad and $\sigma_{P_T} \simeq 0.3\% \cdot P_T^2$ (with $[P_T] = \mathrm{GeV}$) are at reach. As an example of the rejecting power of the algorithm, one can consider the case of the B-decay $\mathrm{B}^0 \to \pi^+\pi^-$, where the requirement of two XFT tracks ($P_T(1) > 2\,\mathrm{GeV}/c$ and $P_T(2) > 3\,\mathrm{GeV}/c$) well separated between them ($35^\circ < \delta\phi < 135^\circ$) fulfilling an additional request on the impact parameter ($|d| > 100\,\mu$m) at Level 2 reduces the rate by a factor 10^3, whilst maintaining an efficiency of $\sim 50\%$ on the signal.

Two potential problems need to be controlled in order for the SVT trigger to meet design specifications; the first concerns mechanical alignment of the SVXII detector, which has to be collinearly aligned with the beam axis within 100 mrad in order to keep into account the fact that SVT does not have z information. The second problem, related to the occupancy of SVXII, is directly connected to the event multiplicity; it may happen, in fact, that high luminosity scenarios, where too many tracks are fed into SVT, could cause

[14] Only four are used by SVT.

[15] Namely, the signed curvature and the ϕ seed (*id est* the azimuthal coordinate of the track at axial superlayer 3 of the COT – see pag. 55).

timing problems in the SVT trigger. The control of this kind of problem will need testing of the SVT machinery on real data in the actual Run II scenario.

Muons

Minor differences distinguish Level 2 from Level 1 muon primitives; this difference is essentially related to the precision of the ϕ-matching between XFT tracks and stubs. At Level 2, in fact, full detector resolution is exploited and the matching is performed within 1.25^o for CMU and CMX, while for CMP the track segment to be matched to the XFT track has to be reconstructed within one-tube stack, which corresponds to an azimuthal coverage of 1.25^o at the closest radial distance from the beam axis, reducing to 0.6^o towards the edges of the chamber.

Electrons

At Level 2, central and plug shower maximum (XCES and XPES) primitives are available for triggering on electrons and photons; the shower maximum detectors rely on the strip/wire chambers (CES) contained in the central electromagnetic calorimeter towers and on two-layers of scintillator strips (PES) located within the electromagnetic plug calorimeters.

Both detectors provide a measurement of the charge deposition as well as a determination of the position of the intersection point of the track trajectory at the detector surface; this is achieved by merging the information collected by strip pads and wires in the central region or by U and V plug scintillators strips (see fig. 2.12).

The purpose of these detectors is two-fold: first, providing rate-rejection handle against non-electromagnetic matter and, second, enabling a separation between electrons and photons.

XCES Although the readout electronics has been completely renewed, both detector specifications and XCES trigger working scheme remain substantially the same for Run II as for Run I.

Only the signals collected by the wires are used at trigger level; the procedure for computing the XCES primitive follows from the shower maximum detector geometry: each calorimeter wedge ($\Delta\phi = 15^o$, $\eta \gtrless 0$) contains two strip chamber modules, each subtending a $\Delta\eta \sim 0.55$ region. There are 32 wires, all parallel to the z-axis and spanning the whole width of a sector, belonging to each module; these are divided into eight groups (*bits*) of four adjacent wires. The pulse-heights of the wires within the same bit are summed together and compared to a threshold; if at least one of the two bits – one per CES module – corresponding to the same average ϕ value fulfills the minimum pulse-height requirement, the corresponding XCES bit is set. In this way 16 XCES bits are defined per detector wedge (8 bits$\times$2 thresholds – high/low P_T electron/photon), leading to a total of 768 XCES bits.

The XCES primitive is usually matched in azimuth and P_T with an XFT track for triggering electrons; the ϕ-matching can achieve a 2^o resolution, which is $\sim$8 times finer than a track-tower matching. This results into a $\sim 50\%$ background reduction, while $\sim 90\%$ efficiency on signal is retained. Efficiency curves as functions of the XCES raw pulse-height for tracks fulfilling standard electron requirements[16] (to

[16]Not including CES requirements.

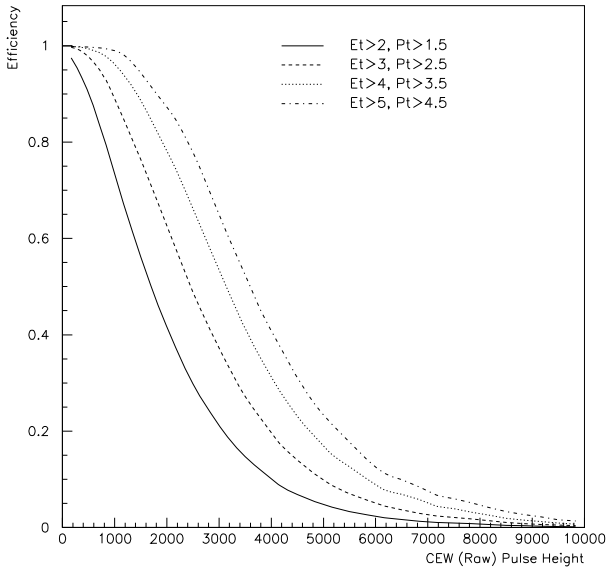

Figure 3.8: *Efficiency curves as functions of the* XCES *pulse-height requirement [4].*

be discussed later, among the Physics Objects) are shown in fig. 3.8 for different track P_T; the following empirical rule for estimating the 90%-efficient pulse height requirement can be drawn:

$$N_{ph}^{90\%} = 500 \times (P_T^{\rm e} - 0.5) \ ,$$

where $P_T^{\rm e}$ is the electron transverse momentum expressed in GeV/c.
Triggering upon photons, on the other hand, involves only a requirement on the pulse-height, while XFT tracking can be used as a veto for charged tracks extrapolating in the vicinity of the XCES bit.

XPES The PES is a new detector, with a different geometry and a different functioning from the CES. Besides, most of its acceptance, covering $1.13 < |\eta| < 3.50$, falls outside the tracking region (which extends up to $|\eta| \simeq 2$).
The possible options for using its information for the Level 2 trigger are numerous but two are presently object of studying. In either case, signals collected by groups of scintillator strips are compared to threshold values and, eventually, correlated to signals collected by the corresponding plug calorimeter towers.

3.2 Physics Objects

As shown in the previous sections, physics objects are of fundamental importance for selecting a signal from the bulk of background events produced in hadronic collisions; however, it was pointed out that at trigger level, especially at Level 1 and 2, the full detector resolutions are seldom exploited completely due to time constraints. The third level of the trigger supplies a further step towards refining selection tools, which has the two-fold implication of augmenting the selection purity and of lowering the event rate to a level compatible with storing procedures.

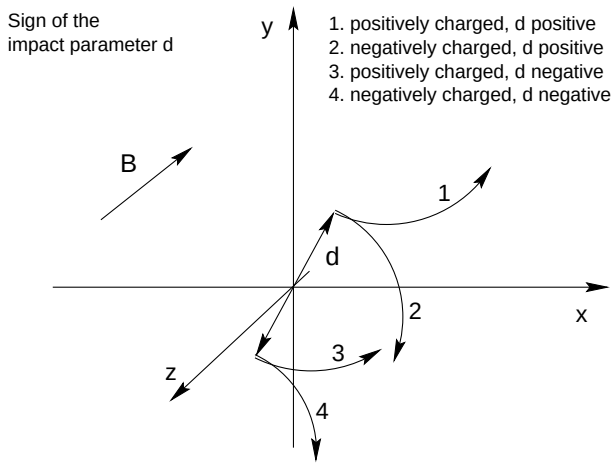

Figure 3.9: *Sign convention for impact parameter.*

3.2.1 Level 3

At Level 3, a more sophisticated event reconstruction is performed; this implies the definition of a new class of physics objects, including three-dimensional tracks, jets and identified leptons, which will be discussed in the following.

Some variables, as well as quantities that need a long processing (like, for instance, global kinematical event observables, or track isolation properties), cannot be calculated within the allowed time slot at trigger level; an further offline processing is then performed on the selected events.

3.2.2 Tracks

Tracks carrying an electric charge qe (where e is the positron charge) travelling with a velocity $\boldsymbol{v}$ in a homogeneous magnetic field $\boldsymbol{B}$ experience a Lorentz force:

$$\boldsymbol{F} = qe\boldsymbol{v} \wedge \boldsymbol{B}$$

that constrains the tracks to a helicoidal trajectory, whose radius, measured in the plane transverse to $\boldsymbol{B}$, is directly related to the track transverse momentum P_T according to the relation:

$$\rho = \frac{P_T}{|q|eB} \ .$$

A track trajectory is completely defined by five parameters [5]:

- $\cot\theta$: cotangent of polar angle of helix measured at minimum approach to beam axis;
- C : signed half curvature (same sign of q);
- z_0 : z-coordinate of minimum approach to beam axis;
- d : impact parameter (minimum distance of helix from beam axis with sign defined according to fig. 3.9);
- φ_0 : azimuthal angle of helix at minimum approach to beam axis.

Reconstruction

Some problems affected the tracking efficiency at CDF during Run I; these can be briefly summarized as follows:

- ◇ the length of SVX and SVX′ ($\sim 50\,\text{cm}$) was covering only part of the $p\overline{p}$ interaction region[17]; consequently, only $\sim 60\%$ of the events fell into the vertex detector acceptance;
- ◇ the four layers of silicon in SVX′, with a $\sim 95\%$ hit efficiency, yielded a global tracking efficiency of $\sim 75\%$ in four-out-of-four hit assignment for tracks within detector acceptance; furthermore, the short lever arm ($\sim 5\,\text{cm}$) induced a poor P_T resolution;
- ◇ the silicon layers in SVX$^{(\prime)}$ were single-sided, thus providing $r-\phi$ information only;
- ◇ three-dimensional tracking efficiency was further degraded by limited stereo sampling in the CTC.

The track-finding procedure used during Run I was based on linking SVX′ hits to previously fitted tracks in the CTC; this method, although improving the resolution achievable on the track parameters, did not allow any recovery from outer tracking inefficiencies.

The CDF tracking system for Run II has then been thought in order to fit a higher luminosity scenario and, at the same time, for correcting the limitations observed during Run I. For this purpose, the CTC and the SVX have been substituted by the COT and a new silicon complex respectively.

The adoption of the COT, a tracking chamber which addresses the increased luminosity and reduced bunch spacing by adopting smaller drift cells, provides a faster response and double stereo sampling with respect to Run I configuration.

Inner tracking (*id est* for $r < 48\,\text{cm}$) is entrusted to a silicon multilayer complex, which includes LAYER00, SVXII and ISL. The combination of these devices results in up to eight points for each fiducial track and guarantees a coverage of almost all $p\overline{p}$ interaction region; position measurements[18], ranging from ~ 1.6 to $\sim 28\,\text{cm}$, supply a long lever arm providing a P_T measurement with a precision of $\delta P_T/P_T^2 \sim 0.4\%$ in the silicon system alone.

The potentialities of this architecture can be fully exploited by means of a tracking procedure, which integrates the information supplied by various detectors. Several options are being investigated: besides the stand-alone COT reconstruction and tracking in the silicon system seeded from COT tracks (inherited from Run I), stand-alone silicon reconstruction and outward extension of silicon tracks in the COT will be possible. The latter options allow tracking to be extended in the region $1 < |\eta| < 2$.

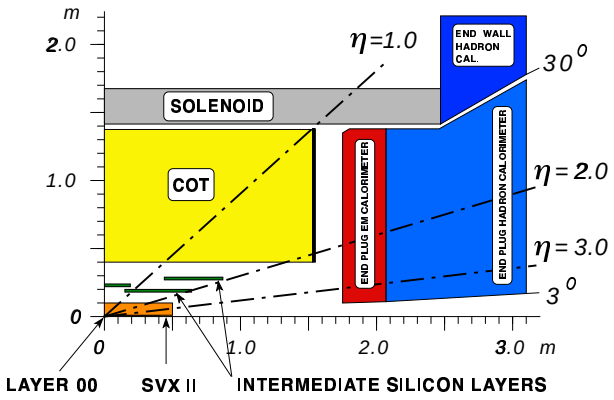

Figure 3.10: *$r-z$ view of* CDF.

[17] $p\overline{p}$ interactions are approximately Gaussian-distributed with $\sigma \simeq 30\,\text{cm}$.

[18] All layers except the innermost provide both $r-\phi$ and $r-z$ information

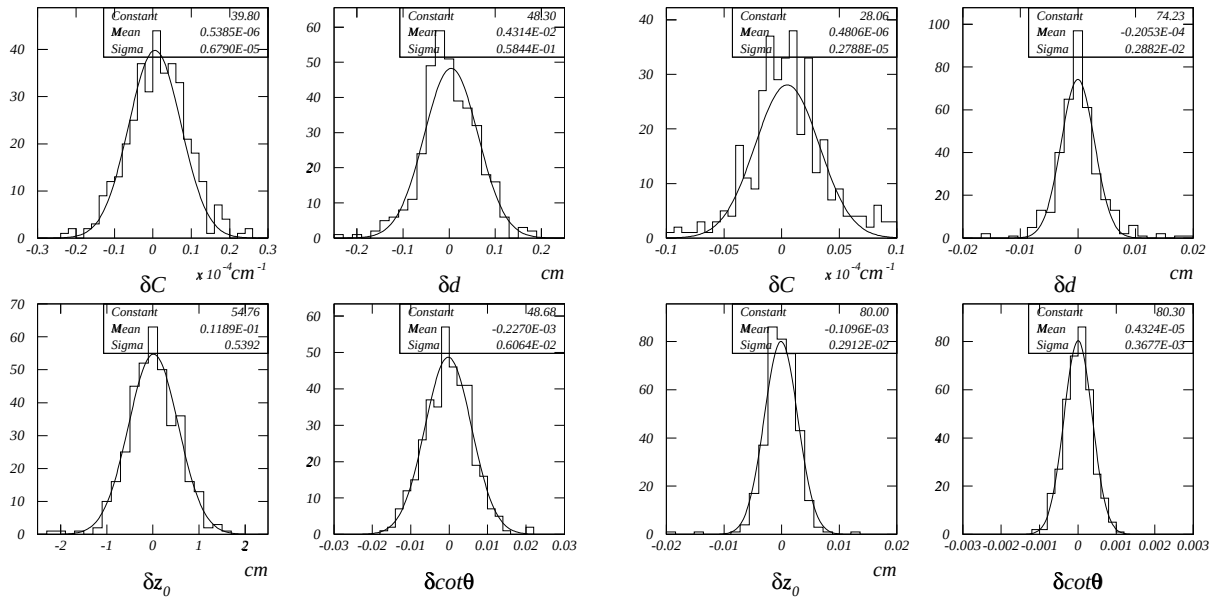

Figure 3.11: *A comparison between expected resolutions on tracking parameters achievable in stand-alone* COT *(left) and integrated tracking (right) environments [6].*

Resolutions

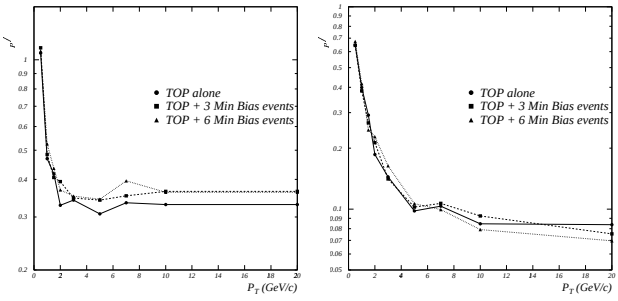

Figure 3.12: *A comparison between expected P_T resolutions for stand-alone* COT *(left) and integrated tracking (right) [6].*

To study the performances of the CDF II tracking system, the dense environment of b-jets in $t\bar{t}$ events have been used. As previously mentioned, if on one hand the design of the new tracking detectors has been developed on the basis of achieving optimal performances even in a higher luminosity scenario, on the other, this led to the introduction of more material around the interaction point (more silicon layers and COT stereo superlayers). Simulations have then been focussed on estimating the impacts that luminosity changes and multiple scattering phenomena induce on the resolution of the tracking parameters; the effect of multiple interactions (whose average number per beam cross depends on both the instantaneous luminosity and number of colliding bunches) is kept into account by mixing one $t\bar{t}$ event with a variable number of generated minimum bias events[19] (see fig. 3.12).

Resolution estimates have been obtained as the difference between the reconstructed track parameters and the corresponding generated quantities which have been supplied as input to the tracking simulator. Results are shown in figs. 3.12 and 3.11; although fig. 3.11 refers to a low luminosity scenario, degradations due to multiple interactions (which have been treated as described above) show a weak dependence on $\mathcal{L}$, of the order of 10% for

[19] An auto-accepting trigger path is used for collecting of unbiased events for calibration purposes.

$\mathcal{L}$ spanning from $1(3)\times10^{32}\,\mathrm{cm}^{-2}\mathrm{s}^{-1}$ to $2(6)\times10^{32}\,\mathrm{cm}^{-2}\mathrm{s}^{-1}$ in correspondence of 36(108) TEVATRON bunches.
Both figs. 3.12 and 3.11 show a comparison of the tracking resolutions achievable by the COT running in a stand-alone mode and by the integration of all tracking devices; this allows to appreciate the contribution of the silicon vertex detector, whose effect – related to the increased number of layer and of their shorter distance from the beam axis – is crucial for pursuing high precision measurements in particular on d and z_0. The effect of augmenting the number of silicon layers and of their arm lever, on the other hand, implies an enhanced resolution on P_T as well. A summary of the resolutions achievable in Run II by CDF is reported in table 3.2.

Resolution		
	COT	COT+SVXII+ISL
$\delta P_T/P_T^2\,[(\mathrm{GeV}/c)^{-1}]$	3×10^{-3}	1×10^{-3}
$\delta d\,[\mu\mathrm{m}]$	600	30
$\delta z_0\,[\mu\mathrm{m}]$	5×10^{3}	30
$\delta\cot\theta$	6×10^{-3}	4×10^{-4}

Table 3.2: *Summary of expected resolutions on various track parameters in Run II.*

In Run I, with an instantaneous luminosity $\sim10^{31}\,\mathrm{cm}^{-2}\mathrm{s}^{-1}$, the CTC could provide a momentum resolution $\delta P_T/P_T^2\simeq0.2\%(\mathrm{GeV}/c)^{-1}$ as a stand-alone tracker and $\delta P_T/P_T^2\simeq0.1\%(\mathrm{GeV}/c)^{-1}$ in combination with SVX or by using beam-constrained tracks. The use of SVX, on the other hand, implied a consistent increase in impact parameter resolution, passing from $\sim340\,\mu$m (stand-alone CTC) to $\sim15\,\mu$m.

The determination of the absolute momentum scale can be obtained by means of a comparison between a clean and known signal to some reference. In the case of CDF the decay $\mathrm{J}/\psi\to\mu^+\mu^-$ is studied; the estimate of the momentum scale is performed by renormalizing the observed $\mathrm{J}/\psi(1\mathrm{S})$ peak to the world average.

3.2.3 Primary vertex reconstruction

Reconstructed tracks enable the computation of the primary vertex in each event: its z position is then used in defining the actual pseudorapidity of each physics object reconstructed in the event, while its transverse position is important since it provides the benchmark for secondary vertex-finding procedures. The $\mathrm{p\overline{p}}$ luminous region has a Gaussian spread of about $35\,\mu$m in the transverse plane: its location is known with good precision, but a more precise determination can be obtained with the track parameters. Instead of relying on the beam spot location, an algorithm can be run on all reconstructed tracks according to an iterative scheme used during Run I (VXPRIM [7]): a P_T-weighted fit is performed with the tracks in the xy plane; tracks with large impact parameter with respect to the fit vertex are discarded, and the fit is repeated until stability is reached. The resulting resolution in the x and y coordinates of the primary vertex ranges from 6 to $26\,\mu$m, depending on the topology of the event and on the number of tracks used in the fit. This determination of the primary vertex represents a significant improvement over the beam spot information alone, and it is more reliable on an event-by-event basis.

3.2.4 Jets

Isolated partons emerging from the initial $p\overline{p}$ collision, due of their nature of strongly interacting matter, undergo a process called fragmentation; during fragmentation, a parton shower is developed from the original parton as an effect of the increasing strong coupling constant as lower P_T regimes are reached. Fragmentation terminates with hadronization, a process where all partons recombine in colour singlet states, corresponding to on shell hadrons. By momentum conservation, the more energetic the initial parton is, the closer the resulting hadrons are confined in phase-space; these clusters of particles are called jets and their importance is related to the fact that they represent the only physically-measurable quantity carrying a reminiscence of the initial parton.

Jet Clustering

The information provided by the cluster finder algorithm at trigger level can be considered as a first-order jet reconstruction; at Level 3, looser time constraints enables to exploit the full detector segmentation for a better jet energy and direction determination.

At CDF a cone algorithm is used for jet reconstruction; the opening angle of the cone is usually defined in terms of a radius in the $\eta-\phi$ plane. Due to the relativistic properties of pseudorapidity, in fact, this definition allows to conveniently identify jets by circular disks on the $\eta-\phi$ calorimetry map. The magnitude of the radius (R) has to be chosen accordingly with the characteristics of the physical process under study: hence, lower radii (typically 0.4) will be preferred in high multiplicity events, where a higher jet resolution is required.

The first step for jet clustering consists in assigning to each calorimetry tower ($\Delta\eta \simeq 0.1$, $\Delta\phi \simeq 15^{o}$) a $r\eta\phi$ vector, with r representing the transverse energy deposition and η, ϕ addressing the corresponding energy barycenter[20].

Preclustering. Vectors with $E_T > 1\,\mathrm{GeV}$ are ranked according to a decreasing magnitude order; the vector list is then scanned downwards in the following way:

1. a circle of radius R is drawn around the first element of the list;
2. all vectors falling inside the circle are summed to it and removed from the list;
3. a new circle is drawn around the next vector in the list;
4. steps 2 and 3 are repeated recursively until the end of the list is reached.

Clustering. A second iterative procedure involving all vectors with $E_T > 0.1\,\mathrm{GeV}$ is started:

5. the E_T associated to each circle is recomputed by merging all the enclosed vectors;
6. new circles are drawn around the so obtained resultants;
7. steps 5 and 6 are reiterated until a stable configuration[21] is reached.

[20] The baricenter of the energy is defined assuming that all electromagnetic and hadronic energies have been released at a depth of 6 radiation lengths (X_0) and 10 interaction lengths (λ) respectively.

[21] A stable configuration is achieved when circles are reconstructed in the same position for two consecutive iterations; usually this happens after three iterations.

It may happen that two circles overlap; in this case, if the total contribution of all vectors belonging to the intersection region does not exceed the 75% of the magnitude of the smaller of the two resultants, each vector is assigned to the closest resultant. Otherwise, the two circles are replaced by a single one, centered around the sum of their resultants.

The circles that remain at the end of the procedure are identified with jets if their energy is large enough (typically 10 or 15 GeV) to guarantee their unambiguous interpretation in terms of partons.

Jet corrections

According to CDF definition, jets emerge from a vector sum of the momenta associated to calorimeter towers enclosed in a certain region (cone), under the assumption that all tower contributions come from massless particles originated in the primary vertex[22] and detected in the energy baricenter of each tower. Unambiguous results can be obtained only if adequate corrections, aimed at reducing systematic effects degrading the energy determination, are applied to the raw energies detected by the calorimeters.

Detector. During Run I, central and plug calorimeter relied on different detection techniques (scintillators and gas proportional chambers respectively); this introduced a non-homogeneity in energy response that had to be accounted for. This effect should be substantially reduced in Run II, thanks to the calorimeter plug upgrade, which will rely on scintillators as an active media.
Imperfect calorimeter coverage as well as limited response for low-P_T hadrons, also contributes in degrading energy measurements, since little or no energy deposition is detected for particles escaping through detector cracks – in particular at boundaries between the central and plug regions – or for soft hadrons reaching the hadron calorimeter.

Clustering procedure. The clustering procedure described above has a finite resolution essentially imposed by R, the jet $\eta - \phi$ radius; particles which, during hadronization or subsequent hadron decay, are emitted at large angles, fail to contribute to the jet they would naturally belong to. In the same way, *out-of-cone* losses can be caused by low-P_T particles being trapped in the magnetic field.

Underlying event and multiple interactions. These two phenomena produce observable effects in the jet clustering procedure. In the first case, strong interactions involving beam remnants can introduce a flux of hadrons that can interfere with particles produced in the hard scattering process; this "extra production" of hadrons can have a relapse on the jet definition, since some particles generated in the underlying event can be included in the clustering procedure. The same can happen when multiple interactions occur, *id est*, when two (or more) collisions occur during the same beam cross; in this case, therefore, more events are overlapped.

All these effects have been accounted for in the definition of jet corrections, whose aim is to suitably rescale the transverse energy of each jet to a value which represents *the most likely E_T that would have been measured if all the degrading effects were not present.* The most general form for the corrections to be applied to the P_T^{raw} of a jet (cone

[22]The definition of primary vertex is different for Level 3 and offline jet clustering; in the first case, in fact, the collision is assumed to take place in the detector origin, while in the latter the primary interaction point is reconstructed by means of a beam-constrained fit of all tracks.

$R = \sqrt{\Delta\eta^2 + \Delta\phi^2}$) is the following [8]:

$$P_T(R) = (P_T^{raw}(R) \times f_{rel} - UEM(R)) \times f_{abs}(R) - UE(R) + OC(R) \ ,$$

where:

f_{rel}:	relative energy scale factor, correcting for non-uniformities in the detector response;
$UEM(R)$:	correction for multiple interactions;
$f_{abs}(R)$:	absolute energy scale factor, rescaling the raw jet energy into the average true jet energy;
$UE(R)$:	correction for underlying event;
$OC(R)$:	*out-of-cone* losses correction.

The absolute calorimetric energy scale can be estimated by means of a two-step procedure. First, the electromagnetic energy scale can be determined using a sample of $J/\psi \to e^+e^-$ or $Z^0 \to e^+e^-$ events; this can be done exactly as for setting the momentum scale of the tracking system by renormalizing the observed $J/\psi(1S)$ and Z^0 peaks to the corresponding world average values. Hence, this information can be used for calibrating the response of the hadronic calorimeter: once the process $Z^0 \to e^+e^- + 1\ jet$ is considered, the hadronic energy scale can be determined by renormalizing the energy of the single jet to the energy measured for the recoiling leptons.

3.2.5 Soft Leptons

Lepton detection and tagging is a crucial feature at hadron colliders, where their presence provide a powerful handle to access electroweak processes. According to their production mode, leptons can be broadly divided into two classes: prompt high P_T leptons, mainly coming from vector boson decay ($Z^0 \to \ell^+\ell^-$ and $W^\pm \to \ell^\pm\nu_\ell$), and non isolated leptons. The latter, referring to leptons embedded within a jet, are usually characterized by a softer P_T spectrum and – in case a correct identification is provided – can be safely related to the semileptonic decay of charmed or bottom hadrons. In fact, decaying bottom or charmed hadrons are expected to emit an electron or a muon[23] in approximately 20% of the cases. Furthermore, bottom hadrons decay in charmed hadrons[24], whose downstream decays can yield leptons.

Electrons

Electron tagging at CDF essentially relies on energy depositions in the electromagnetic towers of the calorimeter; identification procedures, however, depend on both the transverse energy and the rapidity of the candidate. For electrons produced in the semileptonic decay of bottom and charmed hadrons, being characterized by a softer P_T spectrum with respect to prompt electrons, a reconstructed track extrapolating to an electromagnetic deposit and consistent with E/P electron hypothesis is needed to reduce the background from photons; therefore, electron identification is limited within the acceptance of the tracking system. During Run I, soft electron tagging was then performed within $|\eta| < 1$.

[23] Taus, although produced with almost equal frequency than electrons and muons, due to their problematic detection, do not give a significant contribution to B physics at CDF.

[24] Since $|V_{cb}|^2 \sim 200 \cdot |V_{ub}|^2$.

In Run II one hopes to fully exploit the new tracking capabilities as well as the performances of the new plug calorimeter; however, at the present moment, predictions are difficult to make, since the new detector has not been tested in running conditions. Moreover, the detector simulation and reconstruction packages in the Run II configuration is still under development.

The possibility of a non-electron track faking an E/P requirement because of the contribution of surrounding soft particles releasing energy in the same calorimeter towers is still high; a further contribution may also come from isolated hadrons performing early showering (*id est*, before reaching the hadronic section of the calorimeter). Two sets of requirements help in keeping these effects under control; the first one relies on two purely calorimetric variables:

- $\diamond$ E_{had}/E_{em}: an upper bound on this variable can essentially result in an upper bound on the hadronic energy deposition detected within a jet cone. According to the process that led to the electron, the ratio E_{had}/E_{em} can be computed on cluster topologies other than jets, such as single towers or 3×3-tower squares.

- $\diamond$ L_{shr}, the lateral shower shape χ^2, is a χ-squared comparison of the observed calorimeter lateral shower profile to test-beam electrons.

The second set, on the other hand, exploits the information provided by the CES detector. The latter proves to be of crucial importance for tagging non isolated electrons, due to its finer granularity with respect to the calorimeter towers; a predetermined number (typically 3, 5, 7, 9 or 11) of contiguous strips (or wires) is clustered around a seed, whose rôle can be played by a strip/wire either detecting an energy larger than 0.5 GeV or intercepted by the trajectory of a reconstructed track. Three kinds of information are accessible after clustering:

pulse-height: the energy content of a cluster reconstructed either in the strip or in the wire plane (E_s, E_w);

position: the centroids of the clusters reconstructed in the strip and wire planes provide a x–z reading in the local wedge-coordinate system (see fig. 2.10). This information is useful for providing a high quality track-cluster matching;

shape: two χ-squared comparisons (χ^2_{strip}, χ^2_{wire}) of CES cluster profile fits (in strip and wire planes respectively) to test beam electrons.

Cluster-based procedures for electron tagging, like the standard electron selection described in table 3.3, however, contain several implicit isolation requirements that makes them rather inefficient in case the soft electron is embedded in a jet, which is the most likely situation expected in b and c quark decay; clustering procedures, in fact, tend to average energy contributions coming from adjacent towers, making a few-GeV signal very difficult to distinguish from the large backgrounds provided by photons and low-energy hadrons releasing most of their energy in the electromagnetic calorimeter.
For this reason, during Run I a track-based soft electron tagging procedure[25] has been studied [9] and applied in offline analyses involving b-jet identification, for instance in top

[25]The soft electron track-based procedure is part of a more general algorithm, dedicated to soft lepton tagging (often indicated as SLT).

Variable	Std. electron cuts[26]	Soft electron cuts[27]
$(E_T)_{em}$	>7.5 GeV	–
P_T	>6 GeV/c	$\geqslant 2$ GeV/c
E_{em}/P	–	$\geqslant 0.7$, $\leqslant 1.5$
E_{had}/E_{em}	<0.04 [28]	<0.1
L_{shr}	<0.2	–
E_{s_5}/P, E_{w_5}/P [29]	–	$\geqslant \min\{0.6, 0.24+0.03P\}$ GeV
$\lvert\Delta x\rvert$ [30]	<1.5 cm	$\leqslant \max\{0.7, 1.82-0.1867P\}$ cm
$\lvert\Delta z\rvert$ [30]	<3 cm	$\leqslant 2$ cm
$\chi^2_{strip}/6$	<10	$\leqslant 16$
$\chi^2_{wire}/6$	<10	$\leqslant 16$
Q_{CPR}	–	$\geqslant 4744-11592(P/P_T)+7923(P/P_T)^2$
Q_{CTC}	–	$\geqslant 29.15+e^{1.671-0.08P}$, $P\leqslant 15$ GeV/c

Table 3.3: *Standard electron selection compared to soft electron requirements (P, P_T expressed in* GeV/c*) for Run I; further explanation is provided in the text.*

searches [12]; instead of beginning from an electromagnetic deposition in the calorimeter, the algorithm starts by extrapolating all tracks passing a standard set of loose quality criteria to the central electromagnetic calorimeter (CEM) and to the muon chambers. Then, if the track extrapolates to a fiducial region of the detector, it is flagged as a 'candidate' track; in the following, candidate tracks undergo a selection criteria – whose main requirements are reported in table 3.3 – optimized for tagging electrons coming from b quark decay.

The soft electron tagger is characterized by a fake rate of $\lesssim 0.4\%$ per track, at the same time retaining an average efficiency of $\sim 70\%$ on single electron tracks [11].

In order to achieve these goals, the soft electron algorithm exploits two more track-dependent pieces of information supplied by the detector: the energy deposition in the central preradiator (CPR) and the specific energy loss ($\mathrm{d}E/\mathrm{d}x$) experienced by the candidate track in traversing the central tracking chamber.

The CPR energy (Q_{CPR}) is computed in a similar way to CES: a three-wire sum is performed around the point the track extrapolates to; since larger track η values correspond to thicker layers of material travelled by the particle, larger charge depositions in the CPR are expected for increasing η. Exploiting this fact, a rough z matching can be obtained between the CPR deposition and the track by introducing a $P/P_T = 1/\sin\theta$ dependence in the CPR pulse-height requirement.

Within the range of interest, $\mathrm{d}E/\mathrm{d}x$ is essentially independent from momentum if electrons are considered; conversely, a strong momentum dependence is exhibited by other particles, like muons and light charged hadrons, which can contaminate the electron sample. The specific energy loss (Q_{ctc}) is required to match the expected electron behaviour for

[26] The standard electron tagging procedure is cluster-based: all calorimetric quantities refer to reconstructed jets unless explicitly remarked.

[27] The soft electron tagger relies on a track-based procedure: single tower quantity are used when calorimetric variables are computed. The tower is determined by extrapolating the candidate electron track to the electromagnetic calorimeter.

[28] In a 3×3-tower square centered in the electron jet seed.

[29] E_{s_5}, E_{w_5} are five-strip/wire cluster energies.

[30] Δx and Δz describing the spatial mismatch between track extrapolation at CES and cluster centroid.

$P \leqslant 15\,\mathrm{GeV}/c$.

A serious source of background for either cluster-based or track-based procedure is due to photons arising from the decay of neutral pions, copiously produced within jets, which tend to convert into electron-positron pairs in detector material. The P_T spectrum of these electrons is not very different from that of electrons produced in b and c quark decays. This can be achieved by means of an algorithm that, after reconstructing all possible conversion pairs within an event, discards any electron candidate that can be associated to one leg of a conversion pair; in order to tag conversion pairs, the algorithm performs a first selection on the basis of geometrical considerations: two variables, $\Delta \cot\theta$ and $\Delta S = D - \rho_1 - \rho_2$, where D is the distance between the center of the two circular trajectories – of radii ρ_1 and ρ_2 – describing the tracks in the $r-\phi$ plane, are used to select tracks compatible with coming from a common vertex[31], constrained to lay within 50 cm from the beamline (where the highest concentration of material in the tracking volume is found). Then, the two tracks fulfilling this requirement must converge to an invariant mass lower than $0.5\,\mathrm{GeV}/c^2$ to be tagged as a conversion pair.

Muons

Tagging in the case of muons is much less problematic than for electrons, since the natural tendency of muons to penetrate thick layers of materials can be exploited in order to separate them from surrounding electromagnetic and hadronic matter: for this purpose, the shielding offered by the calorimeters is used, while detection of charged particles beyond them is achieved by means of the muon system. The usual method for tagging muons consists in extrapolating a track to the muon system and matching it to a stub reconstructed therein.

The soft muon algorithm differs from a standard selection essentially because a lower P_T threshold implies taking into account the effect of multiple scattering, which becomes more relevant the lower P_T the particle has; after extrapolation, the distances from the edges of each detector as well as the average multiple scattering distance (σ_{MS}) are computed for each track. These parameters are used to assign tracks to four different fiducial regions of the muon system[32]: CMUP for tracks traversing both CMU and CMP volumes, CMU/CMP for tracks passing through the CMU/CMP volume only, while escaping the coverage of CMP/CMU, and CMX for tracks falling in the CMX fiducial volume. Each track falling in one of these classes is then matched to a muon stub; matching requirements depend on the class the track belongs to, as described in table 3.4. From expected mismatch, χ^2 variables are built for each matching quantity: Δx refers to the distance between the extrapolated track and the stub in the transverse plane computed at the inner radius of the muon detector, while Δz refers to the mismatch in the z direction; in particular, the variable $\chi^2_{\Delta\phi\Delta x}$ takes into account the correlation between Δx and $\Delta\phi$, the latter describing the mismatch between the track extrapolated direction and the stub slope.
The major source of contamination in the case of muons arises from calorimeter *punch-throughs* (secondary charged pions leakages through the outermost layer of the hadron calorimeter) and from muons produced in the decays in flight of kaons or pions, which are responsible of 'fake' stubs. The former is strongly limited by the coincidence of CMU

[31] Actual requirements on these variables are $|\Delta\cot\theta| < 0.06$ and $\Delta S < 0.3\,\mathrm{cm}$.

[32] The value of $\sigma = \sqrt{\sigma^2_{SM} + \sigma^2_{res}}$, with σ_{res} describing the resolution of the detector, will be used as an estimate of the Gaussian fluctuation affecting the extrapolated position of the track in the muon system.

Variable	Soft muon cuts			
	CMUP[33]	**CMU**	**CMP**	**CMX**
P_T	$\geqslant 3\,\mathrm{GeV}/c$	$\geqslant 2\,\mathrm{GeV}/c$	$\geqslant 3\,\mathrm{GeV}/c$	$\geqslant 2\,\mathrm{GeV}/c$
$\lvert\Delta z\rvert$	$< \max\{3\sigma, 8\,\mathrm{cm}\}$	$< \max\{3\sigma, 8\,\mathrm{cm}\}$	–	–
$\lvert\Delta x\rvert$	$< \max\{3\sigma, 2\,\mathrm{cm}\}$	$< \max\{3\sigma, 2\,\mathrm{cm}\}$	$< \max\{3\sigma, 5\,\mathrm{cm}\}$	–
$\lvert\Delta\phi\rvert$	–	–	$< 0.1\,\mathrm{rad}$	$< 0.1\,\mathrm{rad}$
$\chi^2_{\Delta\phi\Delta x}$	–	< 10 [34]	< 10 [35]	< 9 [36]
$\chi^2_{\Delta x}$	–	–	–	< 9
$\chi^2_{\Delta z}$	–	–	–	< 9
$E_{had} - \Sigma_p^{0.2}$ [37]	$< 6\,\mathrm{GeV}$	$< 6\,\mathrm{GeV}$	$< 6\,\mathrm{GeV}$	–

Table 3.4: *Soft muon requirements for Run I; further explanation is provided in the text.*

and CMP in the CMUP category. Furthermore, since punchthroughs are characterized by a higher activity in the muon chambers (especially in the CMU), an upper limit on the number of tubes involved in the stub definition (typically 5) is applied.

[33] Matching requirements for CMUP tracks refer to stubs in CMU only; the presence of a stub in CMP is enough to reduce background from *punchthroughs*.

[34] The $\chi^2_{\Delta\phi\Delta x}$ (CMU) replaces the straight Δx requirement for $P_T < 20\,\mathrm{GeV}/c$.

[35] The $\chi^2_{\Delta\phi\Delta x}$ (CMP) replaces the Δx, $\Delta\phi$ requirements for $P_T < 10\,\mathrm{GeV}/c$.

[36] The $\chi^2_{\Delta\phi\Delta x}$ (CMX) replaces the $\Delta\phi$ requirement for $P_T \leqslant 5\,\mathrm{GeV}/c$.

[37] The variable $\Sigma_p^{0.2}$ is defined as the sum of the momenta of all tracks reconstructed within a cone of $R = 0.2$ around the candidate muon. This cut, applied to tracks with $P_T > 6\,\mathrm{GeV}/c$ only, is aimed at increasing muon purity; above this value, muons – which are minimum ionizing particles – deposit smaller energies in the calorimeters than hadrons.

Bibliography

[1] T. Lyss, R. Loser, *"$t\bar{t}$ Production Cross Section for 100 pb^{-1}"*, CDF internal note 3481, Jun 1997.

[2] M. Albrow *et al.*, (The CDF Trigger and Datasets Working Group), *"Run II Trigger Table and Datasets Plan"*, CDF internal note 4718, Sep 2000.

[3] S. Belforte *et al.*, *"SVT – Silicon Vertex Tracker – Technical Design Report"*, CDF internal note 3108, Oct 1996.

[4] K. Byrum, A. B. Wicklund, *"E_T dependence of the XCES trigger"*, CDF internal note 4424, .

[5] H. Wenzel, *"Tracking in the SVX"*, CDF internal note 1790, May 1998.

[6] F. Abe *et al.* (The CDF II Collaboration), *"The CDF II Detector Technical Design Report"*, FERMILAB-PUB-96-390-E, Oct 1996.

[7] S. Dell'Agnello *et al.*, *"A Primary Vertex Finding Package"*, CDF internal note 1789, 1992.

[8] T. Affolder *et al.* (The CDF Collaboration), *"Measurement of the Top Quark Mass with the Collider Detector at Fermilab"*, HEP-EX/0006028, Jun 2000.

[9] C. Campagnari, D. Kestenbaum, *"Review of the SLT Algorithm for Run Ib"*, CDF internal note 3682, May 1996.

[10] G. Apollinari *et al.*, *"Measurement of the $t\bar{t}$ production cross section using SLT tags"*, CDF internal note 3861, Nov 1996.

[11] C. Campagnari, D. Kestenbaum, *"The SLT tags and backgrounds for 110 pb^{-1}"*, CDF internal note 3582, May 1996.

[12] F. Abe *et al.* (The CDF Collaboration), *Phys. Rev.* **D 50**, 2966 (1994).

Chapter 4

An improved multijet trigger for Run II

One of the primary goals for Run II at TEVATRON is the search for the Higgs boson. Studies based on Run II simulations show that, for an integrated (CDF and D0) luminosity of the order of $10\,\mathrm{fb}^{-1}$, a 3σ H^0 evidence is at reach for $M_\mathrm{H} \lesssim 130\,\mathrm{GeV}/c^2$, while a 95% C.L. exclusion is achievable for $M_\mathrm{H} \lesssim 190\,\mathrm{GeV}/c^2$ [1].

Although Higgs production at TEVATRON is dominated by gluon fusion ($\sigma \sim 0.7\,\mathrm{pb}$ for $M_\mathrm{H} = 120\,\mathrm{GeV}/c^2$), its associated production with a vector boson is a much more promising channel despite its lower cross-section ($\sigma \sim 0.3\,\mathrm{pb}$ for $M_\mathrm{H} = 120\,\mathrm{GeV}/c^2$ – see fig. 1.12), since it allows a much more effective control of the QCD background by the vector boson reconstruction.

Experimentally, the most promising final states correspond to leptonic decays of the vector bosons, since the isolated high P_T leptons provide a good trigger and a clean signature; however, they are affected by a limited branching ratio ($\sim 11\%$). Conversely, final states with hadronically decaying vector bosons are characterized by a higher branching ratio ($\sim 47\%$), but suffer from multijet backgrounds which are expected to be several orders of magnitude larger.

In both cases, however, since for $M_\mathrm{H} \lesssim 130\,\mathrm{GeV}/c^2$ the favoured Higgs decay channel proceeds through $\mathrm{b\overline{b}}$ production (*B.R.* $\sim 70\%$ – see fig. 1.14), b-jet identification is a crucial feature for reducing backgrounds; two approaches can be pursued: the first one – object of this study – consists of tagging the soft leptons produced in the semileptonic decay of the B hadrons and is complemental with the second one, which, on the other hand, exploits the large B-hadron lifetime.

4.1 Run I trigger

During Run I, a trigger for multijet final states was developed for top quark searches [2], which eventually culminated with its discovery [3]. The multijet trigger for Run Ib consists of the following requirements:

- Calorimetric requirements at Level 2 on the total detected energy ($\Sigma E_T \geqslant 120\,\mathrm{GeV}$), global clusterized energy ($\Sigma E_T^{cl} \geqslant 125\,\mathrm{GeV}$) and number of hadronic[1] clusters ($N_{cl} \geqslant 4$, with $E_T^{cl} \geqslant 15\,\mathrm{GeV}$);

[1] *Id est* type 3 clusters, according to the classification given on pag. 57.

◇ Cluster requirements are confirmed at Level 3, when a more refined clustering procedure is available: at least 4 jets with $E_T^{jet} \geqslant 10\,\mathrm{GeV}$ have to be found.

This selection was found to be extremely efficient ($\sim 90\%$) on $t\bar{t}$ events, where a high jet multiplicity is expected in case both t quarks decay hadronically; furthermore, limited trigger cross section ($\sim 3\,\mathrm{nb}$) guaranteed a low event rate.

The data sample collected with this trigger was also used in a subsequent search for the Standard Model Higgs boson [4]. However, given the fact that the multijet trigger criteria were motivated by the kinematics of the top quark decay into six jets, the trigger was found to be rather inefficient for the Higgs search (see fig. 4.1 on next page). Improving trigger performance requires a loosening of the kinematical cuts, while the trigger rate has to be kept under control by some other means, for example by tagging the soft leptons produced in the semileptonic decay of b and c quarks originated by the bosons.

4.2 Data samples

As of this writing, the CDF Run II software environment is under development within an object oriented framework written in C++ language; in particular, the trigger and full detector simulations are not yet available. For this reason, a FORTRAN simulation package based on Run I detector has been used; for trigger studies, a specific module has been developed (RUN2TRS) which provides efficiencies and acceptances of the Run II detector.

Signal

Samples of 10000 H^0+$Z^0/W^{\pm}\to b\bar{b}$+$q'\bar{q}$ events have been generated at $\sqrt{s}=2\,\mathrm{TeV}$ with PYTHIA for $M_H = 110$, 120, $130\,\mathrm{GeV}/c^2$ and subsequently processed through the detector simulator (QFL).

Background

Level 2 & 3 background rate estimates have been performed on a sample of 500000 JET20 events collected during Run Ib by means of a trigger which essentially requires a cluster with $E_T \geqslant 20\,\mathrm{GeV}$ at Level 2.
Since the simulation of QCD processes with multijet final states are unreliable, a real data sample collected with loose requirements[2] has been preferred to a Monte Carlo generated sample for a description of background characteristics.

The efficiency of lepton requirements have been studied on a sample of 30000 conversion electrons and of 10000 muons from $J/\psi(1S)$ decay, both collected during Run Ib; electrons have been searched for in a low P_T inclusive single electron dataset, while muons have been isolated by means of a low P_T single muon trigger path within a dimuon dataset used for $J/\psi(1S)$ studies[3].

In the following, the implicit assumption of a medium luminosity scenario for Run II has been made; therefore, according to table 3.1 on pag. 52, the value $\mathcal{L} = 10^{32}\,\mathrm{cm}^{-2}\mathrm{s}^{-1}$ has been assumed in all rate estimations.

[2] Almost the totality ($\sim 99\%$) of the signal passes the Run I JET20 trigger.

[3] The trigger paths used for collecting the unbiased electron and muon samples are included in the trigger CEM_8_CFT_7_5_XCES and PSIA_DIMUON_JPSI_SINGLE_V1 respectively.

4.3 Level 1

4.3.1 Calorimetry

The Level 1 calorimetric primitive has been taken from the QCD inclusive jet path, which requires a single inclusive trigger-tower with energy content above a certain E_T threshold. Two threshold values have been so far proposed (5 and 10 GeV [5]), but only the highest one is interesting for this study. This is because loose requirements, leading to higher rates, can be incompatible with the allowed trigger bandwidths, in which case the acceptance rate is artificially limited by means of a prescaler. The same rejection, however, affects signal efficiency, which makes prescaled trigger paths particularly inconvenient for rare processes.

The signal efficiency after the requirement of an inclusive trigger-tower with $E_T \geqslant 10\,\mathrm{GeV}$ is $\gtrsim 98\%$, while the rate has been estimated to be 2.7 kHz (for $\mathcal{L} = 10^{32}\,\mathrm{cm}^{-2}\mathrm{s}^{-1}$).

4.4 Level 2

4.4.1 Calorimetry

As previously mentioned (see § 4.1), the Run I multijet trigger was not optimized for Higgs searches and, consequently, was found to be rather inefficient in selecting $H^0+Z^0/W^{\pm}$ hadronic final states [6]; as can be seen from fig. 4.1, Level 2 calorimetric requirements of this trigger cannot overcome a 30% efficiency level.

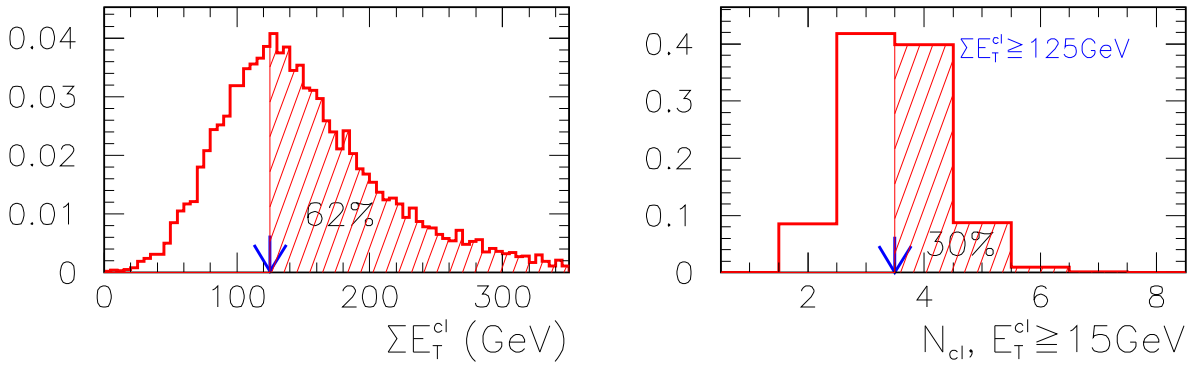

Figure 4.1: *Run I multijet trigger efficiency for Level 2 calorimetric requirements on* $HV \to b\bar{b}q\bar{q}^{(\prime)}$ *($M_H = 120\,\mathrm{GeV}/c^2$) sample.*

The initial modification towards an Higgs-optimized multijet trigger has been motivated by topological considerations on the signal: $H^0+Z^0/W^{\pm} \to$ *had* events are expected[4] to produce four jets in the final state; taking into account the eventuality of loosing one jet or merging two of them, the possibility of requiring only three clusters at Level 2 has been considered, which, according to fig. 4.1 (right plot), would guarantee a significant increase in the efficiency.

[4] Disregarding initial and final state radiation processes at this time.

At this point, two parameters still need to be fixed: the E_T threshold of the (at least) three clusters and the ΣE_T^{cl} threshold. The possibility of requiring unequal thresholds for the cluster E_T has been investigated, but led to no significant improvement in the signal-to-background ratio.

A further step towards a signal to background ratio enhancement can be pursued by constructing an optimal ΣE_T^{cl} primitive; in principle, ΣE_T^{cl} could be defined as the sum of the E_T of all hadronic clusters (type 3, according to the definition of pag. 57) with energy content above a certain threshold. In the following, only two cases are considered:

- $\Sigma E_T 3 \equiv \Sigma E_T^{cl}$ where $E_T^{cl} \geqslant 3\,\mathrm{GeV}$;
- $\Sigma E_T 10 \equiv \Sigma E_T^{cl}$ where $E_T^{cl} \geqslant 10\,\mathrm{GeV}$.

In order to take into account the natural correlation between the ΣE_T^{cl} and the number of clusters, the behaviour of different combinations of ΣE_T^{cl} primitives and cluster E_T thresholds has been studied; the results are shown in fig. 4.2.

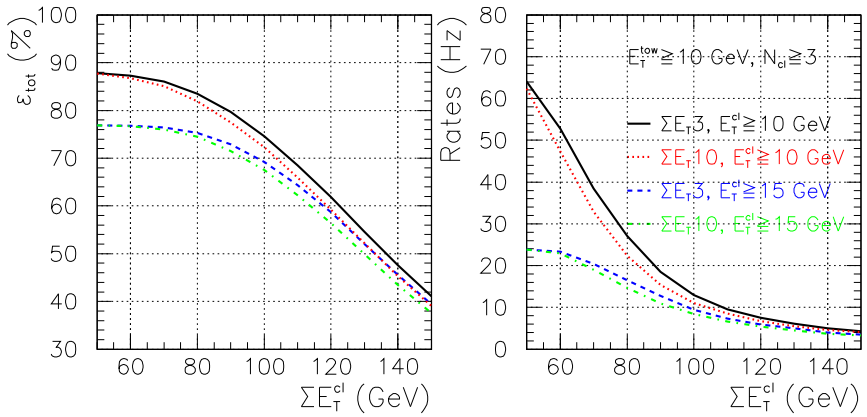

Figure 4.2: *Level 2 efficiencies (left) and rates (right) for different calorimetric requirements as functions of the corresponding ΣE_T^{cl} primitives. Efficiencies and rates are computed on* $\mathrm{HV} \to \mathrm{b\bar{b}q\bar{q}}^{(\prime)}$ *($M_\mathrm{H} = 120\,\mathrm{GeV}/c^2$) and* JET20 *respectively.*

The choice of the optimal Level 2 primitive is performed on the basis of efficiency maximization. Since no secondary vertex explicit reconstruction will be made at Level 3, a rate level of ~ 15 Hz is acceptable if compared to the total Level 2 bandwidth, accounting to 300 Hz (see tab. 3.1); therefore the requirements:

$$\Sigma E_T 10 \geqslant 90\,\mathrm{GeV},\ N_{cl}(E_T^{cl} \geqslant 10\,\mathrm{GeV}) \geqslant 3,$$

corresponding to an efficiency of 77.6% and a rate of 15.4 Hz, will be applied at Level 2.

A graphical representation of the Level 2 calorimetric selection is shown in fig. 4.3, where the distributions of the calorimetric quantities at Level 2 for signal and data are compared.

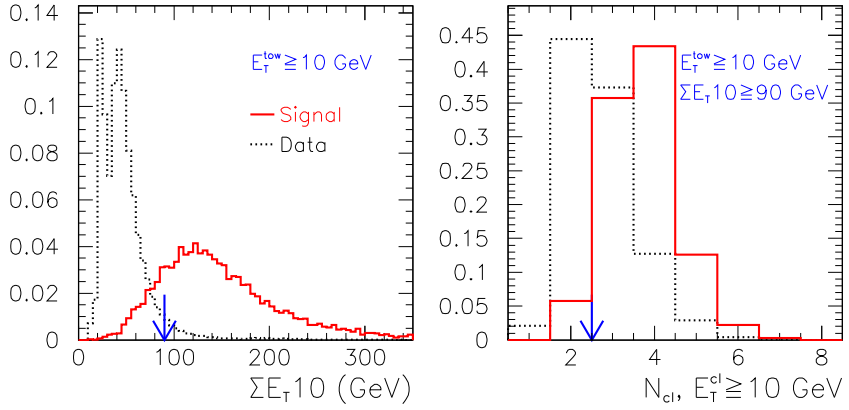

Figure 4.3: $\Sigma E_T 10$ *(left) and number of clusters with* $E_T^{cl} \geqslant 10\,\mathrm{GeV}$ *(right) distributions as functions of* $\Sigma E_T 10$ *for* $\mathrm{HV} \to \mathrm{b\bar{b}q\bar{q}}^{(\prime)}$ *(*$M_\mathrm{H} = 120\,\mathrm{GeV}/c^2$*) signal and* JET20 *background.*

4.4.2 Leptons

Electrons

Electrons emerging from the semileptonic decay of B and D-hadrons produced by H^0 and $\mathrm{Z}^0/\mathrm{W}^\pm$ exhibit a soft P_T spectrum (see fig. 4.4); Run I single electron triggers, being focused on electrons characterized by higher P_T spectra, cannot be applied. Electrons coming from B and D-hadron decays are not expected to be isolated, which, besides their soft P_T spectrum, makes them difficult to tag by means of their energy deposition in the electromagnetic calorimeter, due to the broad $\eta - \phi$ segmentation ($\Delta\eta \simeq 0.2\ \Delta\phi = 15^0$) of its towers.

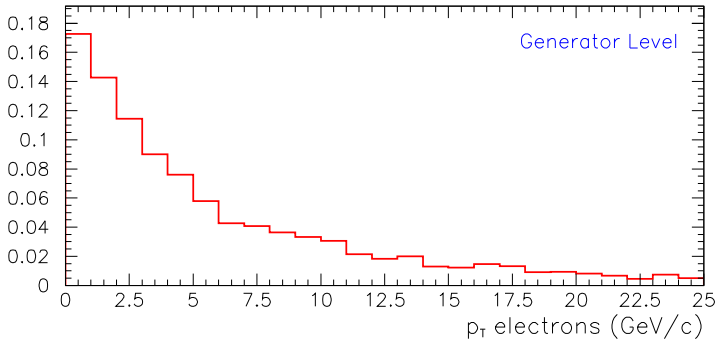

Figure 4.4: P_T *spectrum for generator level electrons produced in* $\mathrm{b} \to \mathrm{e}\nu_\mathrm{e}X$ *and* $\mathrm{c} \to \mathrm{e}\nu_\mathrm{e}X$ *decays in* $\mathrm{HV} \to \mathrm{b\bar{b}q\bar{q}}^{(\prime)}$ *(*$M_\mathrm{H} = 120\,\mathrm{GeV}/c^2$*) events.*

A much finer segmentation in ϕ ($\sim 2^\mathrm{o}$) is however offered by the strip chambers (CES), whose information is available at Level 2 as XCES bits (see § 3.1.2, pag. 61). A XCES bit is set for a given XFT track[5] if the sum of the signals collected by the four wires closest to the track extrapolation point at CES exceeds a certain threshold (two thresholds will be available in Run II).

[5] In order to simulate the XFT behaviour within the Run II environment, Run I smeared CTC tracks are used for mimicking the XFT output.

Due to poor CES simulation, it has been necessary to estimate the XCES efficiency as a function of the pulse-height threshold for true electrons from an experimental data sample; the conversion electrons extracted from the low P_T inclusive electron sample have been used for this purpose. In each event, trigger electrons are combined to all oppositely charged tracks having $P_T > 0.5\,\mathrm{GeV}/c$ and vertex-constrained fits are performed for each pair being consistent with a conversion; the track corresponding to the lowest fit χ^2 value is then identified as a conversion electron if its calorimetric deposition does not exceed the energy associated to the trigger electron. [7]. Applying a standard electron selection[6] (see table 3.3) to the soft legs has made possible the collection of an unbiased sample to test the CES efficiency with respect to the ADC pulse-height associated to the electron track.

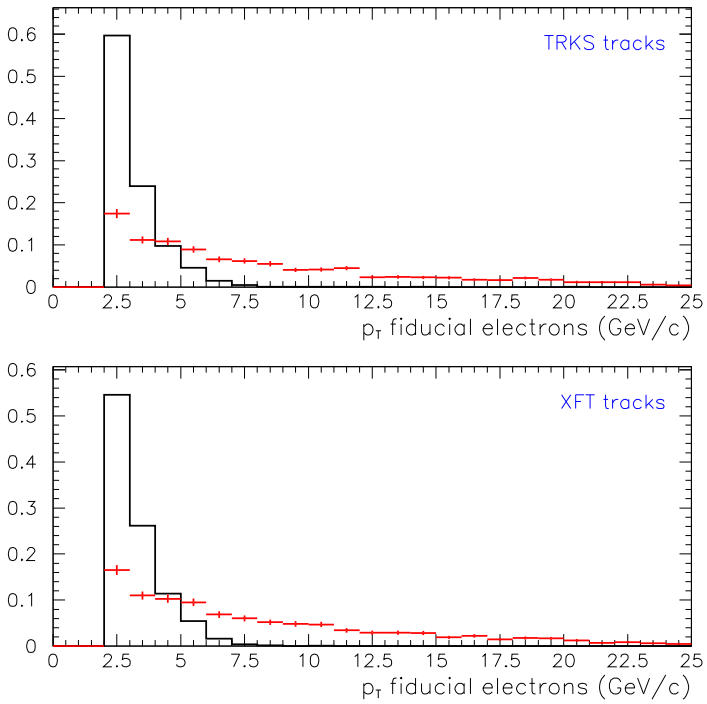

Figure 4.5: *P_T spectrum for* TRKS[7] *and* XFT *reconstructed electrons produced in* $\mathrm{b}\to\mathrm{e}\nu_\mathrm{e}X$ *and* $\mathrm{c}\to\mathrm{e}\nu_\mathrm{e}X$ *decays in the* $\mathrm{HV}\to\mathrm{b\bar{b}q\bar{q}}^{(\prime)}$ *($M_\mathrm{H} = 120\,\mathrm{GeV}/c^2$) sample (crosses) compared to conversion electrons (solid) .*

As shown in fig. 4.5, the selected sample of electrons exhibit a softer P_T spectrum than signal electrons; if on one hand this makes the efficiency evaluation conservative, on the other it may lead to a too conservative estimate, which could invalidate the discriminating power of CES-based requirements. In order to avoid this, two procedures for estimating the CES efficiency have been tested. In one case a simple counting experiment has been performed on the conversion sample irrespective of its P_T spectrum; in the other, the counting experiment has been weighted by the P_T spectrum of signal electrons. The efficiency is then estimated by the expression:

$$\epsilon_\mathrm{e} = \frac{\sum_{i=1}^{N^p} w_i}{\sum_{i=1}^{N^p+N^f} w_i} \ , \tag{4.1}$$

[6]Not including any requirement on wire or strip energies recorded in the CES.

[7]The label TRKS indicates tracks that have been fully reconstructed in the offline analysis.

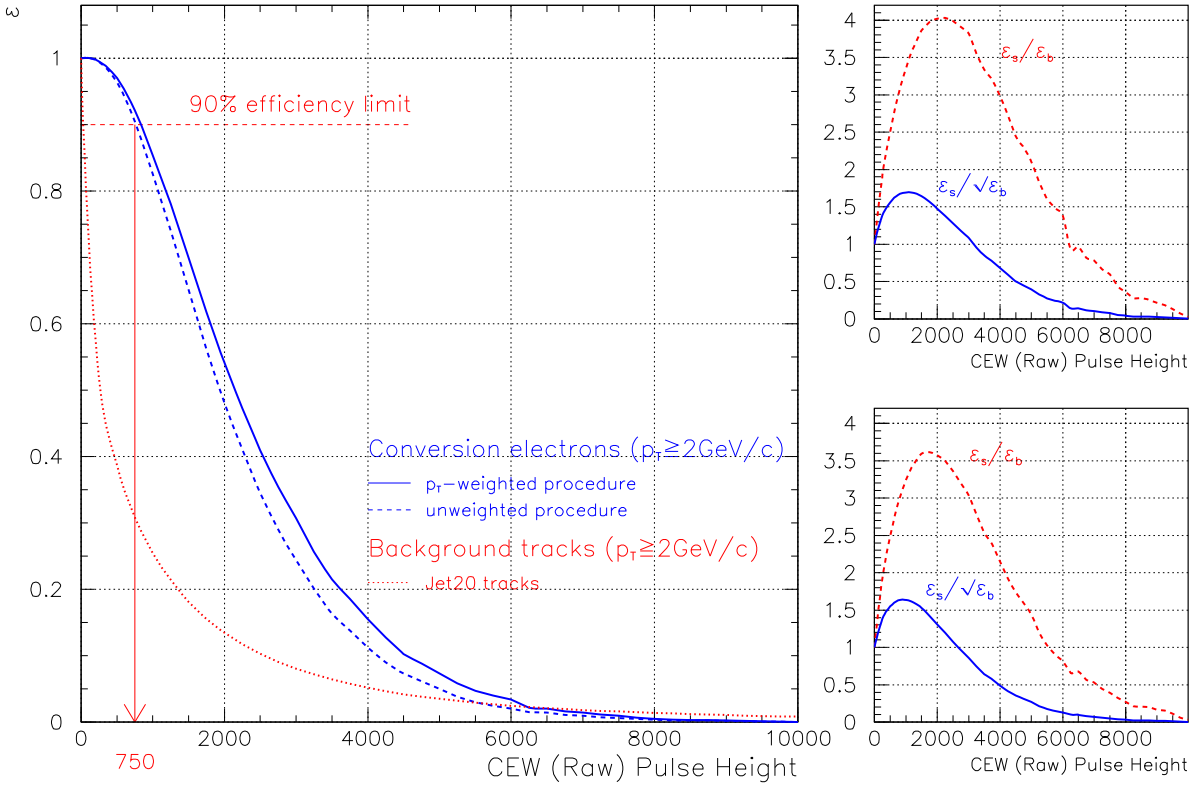

Figure 4.6: *Left:* CES *efficiency vs. minimum* XCES ADC *pulse-height threshold for conversion soft leg electrons and for generic background tracks* ($P_T \geqslant 2\,\mathrm{GeV}/c$). *Right:* S/B *gain (dashed) and significance (solid) for weighted (upper) and unweighted (lower) procedures.*

where N^p and N^f are the number of electrons respectively passing and failing the XCES requirement; each electron has been weighted according to its P_T by a factor w_i, whose values have been calculated from the ratio of signal to conversion electrons (normalized) P_T spectra[8]. In the case of unweighted procedure, expression (4.1) trivially reduces to:

$$\epsilon_e = \frac{N^p}{N^p + N^f} \ . \tag{4.2}$$

The results of both procedures, with the 90%-efficiency limit highlighted, are shown in fig. 4.6.

The two procedures lead to comparable results; in particular, in both cases, the same threshold value of 1000 ADC counts has been found on the basis of significance maximization (see solid curves in the right plots of fig. 4.6). The efficiency for the corresponding XCES requirement (see dashed curves in the left plots of fig. 4.6) are 85.4% and 82.6% for the weighted and unweighted procedures respectively[9].

The suitability of the unbiased sample, with particular reference to the P_T spectrum being softer than expected for signal electrons, has been tested by studying the P_T dependence of the XCES requirement; fig. 4.7, which has been obtained by means of expression (4.2), shows that a plateau value is reached already at $P_T \simeq 5\,\mathrm{GeV}/c$.

[8]More suitably binned distributions have been used rather than the ones depicted in fig. 4.5.

[9]Note that a 90% efficiency is achieved by the unweighted procedure for a pulse-height threshold of 750 ADC counts, which is in agreement with the estimations quoted in [5].

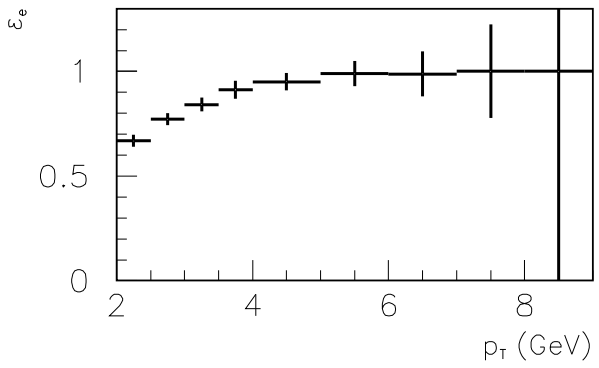

Figure 4.7: *P_T dependence of* XCES *requirement ($E_{\rm ph} > 1000$* ADC *counts) estimated on conversion electrons (overflow bin for $P_T \geqslant 8\,\mathrm{GeV}/c$).*

Hence, the poor CES simulation has been by-passed by weighting each generated electron associated to a XFT track with transverse momentum $P_T(\geqslant 2\,\mathrm{GeV}/c)$ extrapolating to the CES fiducial volume by the corresponding efficiency $\epsilon_{\rm e}(P_T)$.

Finally, the so calculated efficiency per electron leads to the efficiency[10] for selecting a 'signal' event according to the expression:

$$\epsilon_{evt} = 1 - \prod \left(1 - \epsilon_{\rm e}(P_T)\right) \ , \tag{4.3}$$

where the product runs over all CES-fiducial electrons with $P_T \geqslant 2\,\mathrm{GeV}/c$ produced in the semileptonic decay of a B or D hadron coming from V or H^0 in a given event.

Contributions to the rate, on the other hand, come from those background events which contain at least one XFT track with $P_T \geqslant 2\,\mathrm{GeV}/c$ associated to a XCES pulse-height of at least 1000 ADC counts. Results of the selection are summarized in fig. 4.8.

The magnitude of the efficiency drop in passing from the solid curve (Level 2 calorimetry only) to the dotted one (XCES pulse-height requirement added) and the rate behaviour can be interpreted as follows. On one hand, the efficiency drop can be explained considering that in only 30% of the events in which a signal electron has been produced, a signal electron with $P_T \geqslant 2\,\mathrm{GeV}/c$ is emitted within the CES acceptance (after calorimetric requirements, with $\Sigma E_T 10 \geqslant 90\,\mathrm{GeV}$). On the other hand, the small rate rejection can be interpreted in terms of fake tracks. In other words, particles which are either true electrons not related to the signal[11] (such as conversion electrons) or generic tracks fulfilling the XCES pulse-height requirement – neither of which are taken into account in the computation of the efficiency – can contribute significantly to the rate, being implicitly included in its definition.

[10] Efficiencies will here be defined with respect to generated events and not to 'analyzable' ones.

[11] *Id est* not coming from the semileptonic decay of B or D hadrons produced in the decay of either H^0 or V.

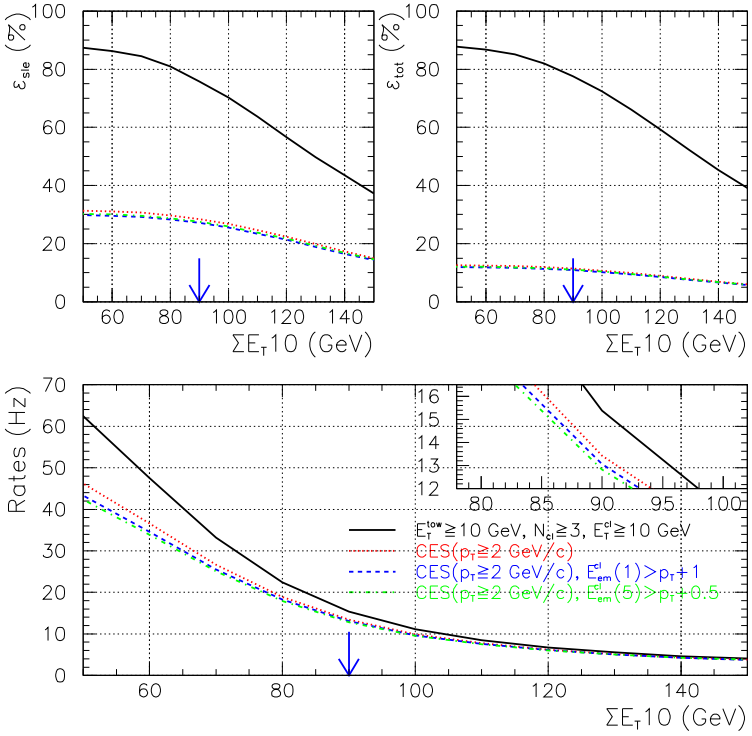

Figure 4.8: *Top: Level 2 efficiency computed on* $H^0V \to b\bar{b}q\bar{q}^{(\prime)}$ *($M_H = 120\,\mathrm{GeV}/c^2$) events; events with a* $b \to e\nu_e X$ *or* $c \to e\nu_e X$ *decay (left) or all events (right). Bottom: rate calculated on* JET20 *sample. Both efficiency and rate are plotted in terms of* $\Sigma E_T 10$.

The effective significance of this hypothesis can be tested by evaluating a fake tag probability, defined as the probability for a CES-fiducial track of passing the XCES pulse-height requirement; this can be done directly on the JET20 events, assuming there is no significant enrichment in heavy flavours in the sample (see fig. 4.9). The only difficulty in this procedure is related to the definition of fiduciality, since XFT tracks carry $r-\phi$ information only; this can be overcome by linking each XFT track to the CTC track that seeded its simulation[12]. Once the track fiduciality in the CES detector has been established, XFT tracks can be extrapolated to the correct XCES bit (as described in § 3.1.2) and the corresponding pulse-height compared to the threshold of 1000 ADC counts.

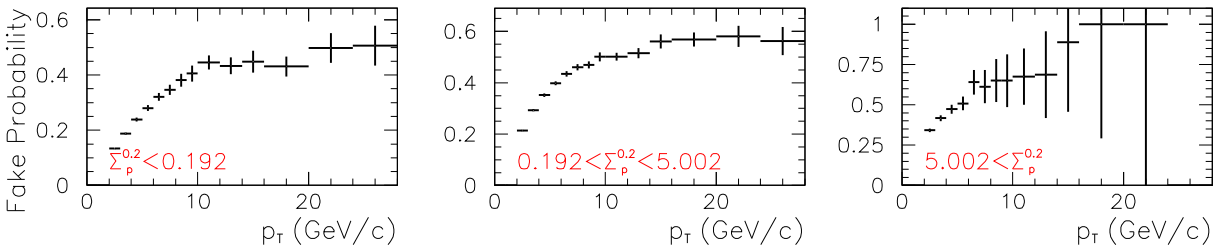

Figure 4.9: *Fake tag probability as a function of track* P_T *for different isolation ranges (for generic tracks in* JET20 *events).*

[12] As explained on pag. 81, XFT tracks are simulated from CTC tracks.

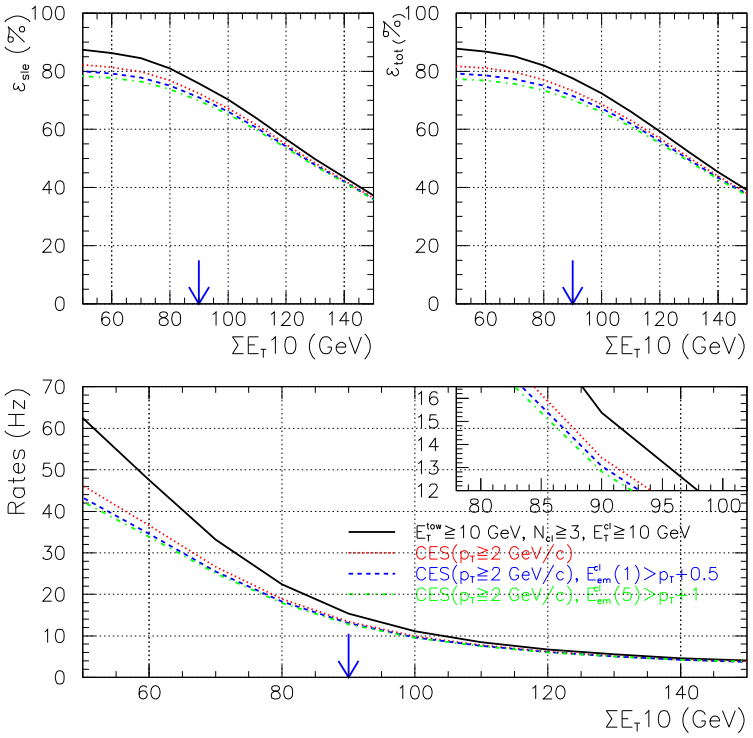

Figure 4.10: *Top: Level 2 efficiency computed on* $H^0V \to b\bar{b}q\bar{q}^{(\prime)}$ *($M_H = 120\,\mathrm{GeV}/c^2$) events when fake electron contribution is taken into account; events with a* $b \to e\nu_e X$ *or* $c \to e\nu_e X$ *decay (left) or all events (right). Bottom: rate calculated on* JET20 *sample. Both efficiency and rate are plotted in terms of* $\Sigma E_T 10$.

The fake tag probability is expected to depend essentially on two variables: the track P_T and its isolation, which has been parametrized according to the quantity $\Sigma_p^{0.2}$, which is defined as the sum of the momenta of all tracks contained in a $\eta - \phi$ cone with $R = 0.2$ around the considered track.

Each track associated to a non-null fake tag probability will therefore result in an enhancement in the P_{evt}, according to a simple generalization of expression (4.3). The magnitude of the fake probability (shown in fig. 4.9) and, consequently, the behaviour of the solid and dotted curves for efficiency and rate shown in fig. 4.10, appears to agree with the hypothesis made; this, furthermore, implies that the XCES pulse-height requirement on its own is not a suitable selection for signal events.

A more strict selection on 'signal' electrons can be pursued at Level 2 by matching (in ϕ only) the XFT-tracks with electromagnetic clusters in the CEM; for this purpose, two different procedures have been considered: the first one uses low P_T electron clusters ('type 1' – see § 3.1.2), while for the second one a new type of electromagnetic clusters has been hypotized (seed[13] 2.5 GeV, infinite shoulder – later referred as 'type 5'). Both procedures are then added to the XCES pulse-height requirement; their effect on both efficiency and rates has already been shown in figs. 4.8 and 4.10 (see dashed curves) and are reported in table 4.1.

[13]The seed value has been chosen in order to maximize the $S/\sqrt{B}$ ratio, while the shoulder has been set in order to force single-tower clusters, which exploits the highest possible CEM granularity available at Level 2 needed to extract the signal of non-isolated electrons.

Selection (E_{ph} in ADC counts)	**Efficiency** (%)		**Rate** (Hz) (JET20)
		+*fakes*	
Calorimetry only	75.8 (77.6)		15.4
$p_T(\mathrm{e}) \geqslant 2\,\mathrm{GeV}/c$, $E_{ph} > 1000$	28.4 (11.4)	72.3 (73.2)	13.4
$p_T(\mathrm{e}) \geqslant 2\,\mathrm{GeV}/c$, $E_{ph} > 1000$ (type 1)	27.1 (10.8)	70.9 (71.5)	13.1
$p_T(\mathrm{e}) \geqslant 2\,\mathrm{GeV}/c$, $E_{ph} > 1000$ (type 5)	27.6 (11.0)	69.9 (70.1)	12.8

Table 4.1: *Level 2 event efficiencies and rate for* $\Sigma E_T 10 \geqslant 90\,\mathrm{GeV}$ *(efficiencies are computed on* $\mathrm{H^0V} \to \mathrm{b\bar{b}q\bar{q}}^{(\prime)}$ *(*$M_\mathrm{H} = 120\,\mathrm{GeV}/c^2$*) with respect to events with a* $\mathrm{b} \to \mathrm{e}\nu_\mathrm{e}X$ *or* $\mathrm{c} \to \mathrm{e}\nu_\mathrm{e}X$ *decay – efficiencies on inclusive sample are indicated in brackets).*

The introduction of the matching requirements has not supplied a solution to the efficiency drop, which is still much more consistent than the one observed correspondingly in the rate; therefore any further requirement, besides the purely calorimetric ones, is not justified.

Muons

Muon identification essentially works on the basis of a matching between a track and a cluster of hits (*'stub'*) collected in some muon chamber. At Level 2, when only ϕ-matching is possible between stubs and XFT tracks, Run II muon triggers will take advantage of a finer azimuthal resolution[14] (1.25°) than in Run I (when the resolution was 5°). This procedure is simulated by using Run I CTC smeared tracks for mimicking the XFT output and Run I low P_T ($3.3\,\mathrm{GeV}/c$) trigger stubs information available at Level 1 for muon chambers performance.

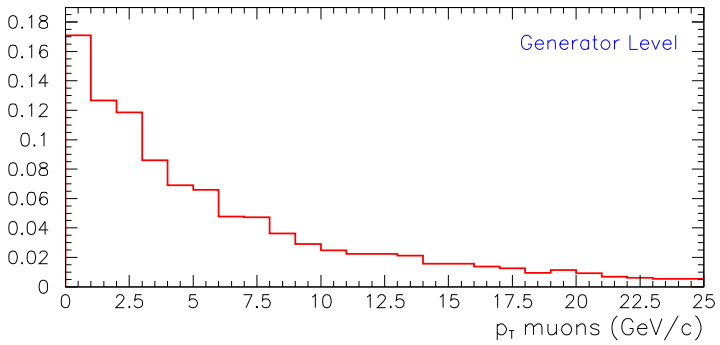

Figure 4.11: P_T *spectrum for generator level muons produced in* $\mathrm{b} \to \mu\nu_\mu X$ *and* $\mathrm{c} \to \mu\nu_\mu X$ *decays in* $\mathrm{HV} \to \mathrm{b\bar{b}q\bar{q}}^{(\prime)}$ *(*$M_\mathrm{H} = 120\,\mathrm{GeV}/c^2$*) events.*

Since, as for electrons, muons generated in $\mathrm{b} \to \mu\nu_\mu X$ and $\mathrm{c} \to \mu\nu_\mu X$ decays are characterized by a soft P_T spectrum (see fig. 4.11), the Run II Level 2 trigger efficiencies have been determined on real muons identified in a sample of events collected in Run Ib by means of a low P_T single muon trigger, which require a Level 1 stub with $P_T \geqslant 6\,\mathrm{GeV}/c$

[14] This is due to the improved track finder procedure implemented for Run II.

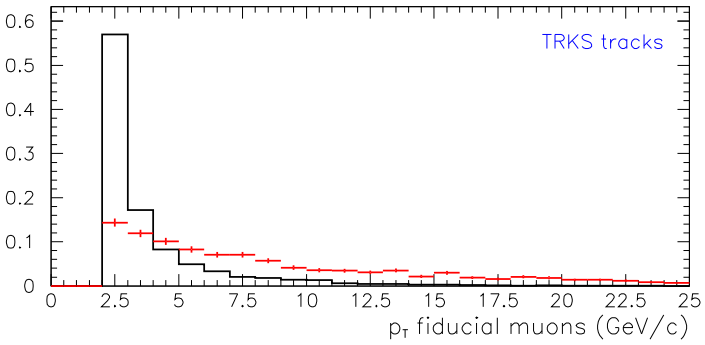

Figure 4.12: *P_T spectrum for fully reconstructed muons produced in* $\mathrm{b}\to\mu\nu_\mu X$ *and* $\mathrm{c}\to\mu\nu_\mu X$ *decays in* $\mathrm{HV}\to\mathrm{b\overline{b}q\overline{q}}^{(\prime)}$ *($M_\mathrm{H}=120\,\mathrm{GeV}/c^2$) sample (crosses) events with respect to* $\mathrm{J}/\psi(1\mathrm{S})$ *muons (solid).*

(CMU, CMP) or $P_T\geqslant 10\,\mathrm{GeV}/c$ (CMX) and at Level 2 a CFT track with $P_T\geqslant 7.5\,\mathrm{GeV}/c$ or $P_T\geqslant 12\,\mathrm{GeV}/c$ matched respectively to a CMU, CMP or CMX reconstructed stub.
Before proceeding in the measurement of the Level 2 muon requirement, consisting of a matching between a low P_T stub and a XFT track, it has been necessary to introduce an unbiased sample of muons. This has been done by tagging as 'unbiased' the muon[15] that, for each event, has provided the best vertex-constrained fit to the $\mathrm{J}/\psi(1\mathrm{S})$ with the trigger muon. Once the unbiased sample has been determined, and the invariant masses of each 'unbiased μ' – 'trigger μ' pair recorded, two mass regions have been defined: a 3σ window around the $\mathrm{J}/\psi(1\mathrm{S})$ peak for the signal and a $4\div 8\sigma$ region away from the $\mathrm{J}/\psi(1\mathrm{S})$ peak for background. Finally, the Run II trigger performance has been tested by means of a counting experiment and its efficiency estimated by the expression (that has to be considered function of the muon P_T):

$$\epsilon_\mu = \frac{N^p_{\mathrm{J}/\psi} - N^p_{bgd}}{\left(N^p_{\mathrm{J}/\psi} - N^p_{bgd}\right) + \left(N^f_{\mathrm{J}/\psi} - N^f_{bgd}\right)}\ , \tag{4.4}$$

where $N_{\mathrm{J}/\psi}$ and N_{bgd} are the number of muons associated to the signal and background mass windows, while the apices p and f indicate passing or failing the Run II trigger requirements. Before studying the Level 2 efficiency, it is worthwhile taking a look to the Level 1 Run I efficiency, shown in fig. 4.13; this offers two pieces of information: first, it allows a cross-check of the unbiased sample by means of a comparison with the results obtained in an independent analysis (indicated by the dotted curves in figure). Secondly, it shows that the Run I Level 1 low P_T trigger requirement is characterized by a smooth turn-up at low P_T: a significant efficiency level ($\gtrsim 70\%$ for CMU and $\gtrsim 50\%$ for CMX) is preserved even below the nominal threshold of $3.3\,\mathrm{GeV}/c$, which reduces the Run II sensitivity from the Run I Level 1 muon requirement, allowing in this way to study the Run II trigger performances down to $\sim 2\,\mathrm{GeV}/c$, which represents some lower working limit for the XFT.

A graphical representation of the P_T dependence of ϵ_μ for Run II Level 2 requirement, on the other hand, is shown in fig. 4.14, where the dotted curves are fitted to the experimental points according to the function described in [8].

[15]Defined as a fully reconstructed track with CMU or CMX information.

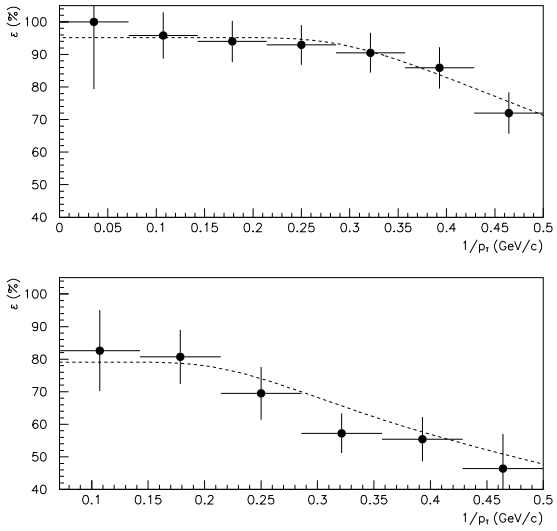

Figure 4.13: *Run I Level 1 low P_T muon trigger efficiency in terms of $1/P_T$ threshold (top for* CMU *and bottom for* CMX*) computed on* J/ψ(1S) *muon sample.*

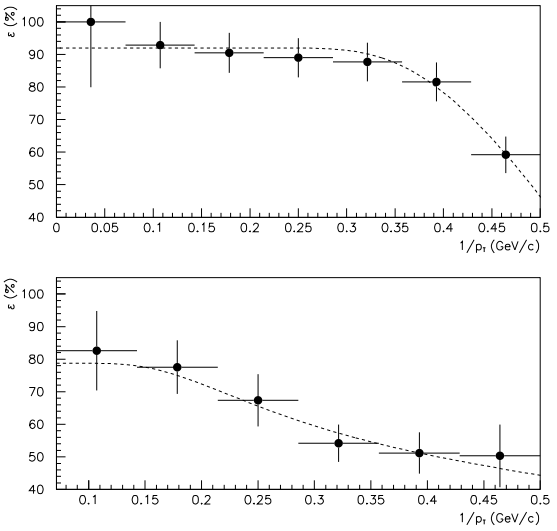

Figure 4.14: *Run II Level 2 low P_T muon trigger efficiency in terms of $1/P_T$ threshold (top for* CMU *and bottom for* CMX*) computed on* J/ψ(1S) *muon sample.*

The method for computing the probability of selecting 'signal' events[16] follows from the convolution procedure used for electrons, which led to the expression (4.3): the weight applied per muon[17] depends on its P_T according to fig. 4.14. The expression for the event efficiency therefore assume the more general form:

$$P_{evt} = 1 - \prod (1 - \epsilon_\mu(P_T)) \ , \tag{4.5}$$

where the product is extended over all signal muons of the event (each associated to a specific value of $\epsilon_\mu(P_T)$) which fall in some muon chamber fiducial volume.

A rescaling has been performed on data for estimating the effect of the increase in acceptance (of a factor $\sim$1.5) of the CMX on Level 2 efficiencies and rates. In order to do this, the total rate has been written as the sum of two contributions:

$$\mathcal{R}ate(total) = \mathcal{R}ate(\text{CMU}, \text{CMU} + \text{CMX}) + \mathcal{R}ate(\text{CMX}) \ ,$$

where $\mathcal{R}ate(\text{CMU}, \text{CMU} + \text{CMX})$, being the contribution from events with at least one signal μ falling in the CMU acceptance, does not depend on the CMX geometry; therefore, assuming an azimuthally symmetric events, the increase in the CMX acceptance can be kept entirely described considering [9]:

$$\mathcal{R}ate(\text{CMX}) \longrightarrow 1.449 \times \mathcal{R}ate(\text{CMX}) \ .$$

At this point, the Level 2 muon requirements have been studied in terms of their efficiency and rate for different values of the μ P_T and $\Sigma E_T 10$; while contributions to

[16] In this case events containing a muon fiducial in some muon chamber and which has been produced in the semileptonic decay of a B or D-hadron coming from V or H^0.

[17] Here a XFT track associated to a fully reconstructed track with CMU or CMX information.

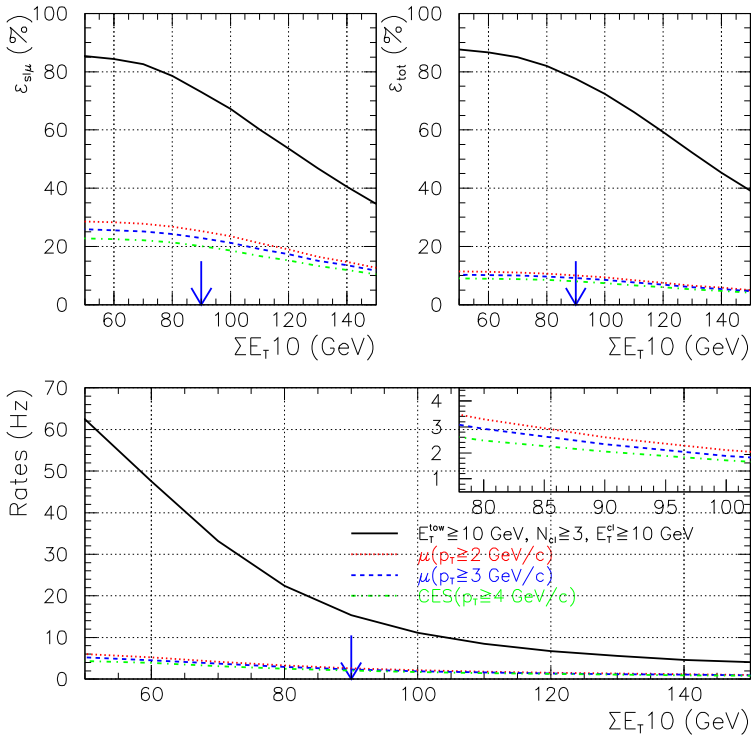

Figure 4.15: *Top: Level 2 efficiency computed on* $H^0V \to b\bar{b}q\bar{q}^{(\prime)}$ *($M_H = 120\,\mathrm{GeV}/c^2$) events is taken into account; events with a* $b \to \mu\nu_\mu X$ *or* $c \to \mu\nu_\mu X$ *decay (left) or all events (right). Bottom: rate calculated on* JET20 *sample. Both efficiency and rate are plotted in terms of* $\Sigma E_T 10$.

the efficiency have been discussed above, contributions to the rate comes from those background events which contain at least one XFT track passing the P_T requirement and that can be associated to a muon stub in the CMU or in the CMX. As shown in fig. 4.15 and in table 4.2, muon-based Level 2 requirements on their own would be perfectly admissable, since the efficiency drop induced by muon acceptance[18] is balanced by a more consistent rate rejection.

Selection	**Efficiency** (%)	**Rate** (Hz) (JET20)
Calorimetry only	73.0% (77.6%)	15.4 Hz
$p_T(\mu) \geqslant 2\,\mathrm{GeV}/c$	25.3% (10.1%)	2.87 Hz
$p_T(\mu) \geqslant 3\,\mathrm{GeV}/c$	22.9% (9.11%)	2.58 Hz
$p_T(\mu) \geqslant 4\,\mathrm{GeV}/c$	20.1% (7.99%)	2.26 Hz

Table 4.2: *Level 2 event efficiencies and rates for* $\Sigma E_T 10 \geqslant 90\,\mathrm{GeV}$ *(efficiencies are computed on* $H^0V \to b\bar{b}q\bar{q}^{(\prime)}$ *($M_H = 120\,\mathrm{GeV}/c^2$) with respect to events with a* $b \to \mu\nu_\mu X$ *or* $c \to \mu\nu_\mu X$ *decay – efficiencies on inclusive sample are indicated in brackets).*

[18]The fraction of events in which a signal muon has been produced within CMU or CMX acceptance ranges between 30% and 23% according to the P_T cut after calorimetric requirements ($\Sigma E_T 10 \geqslant 90\,\mathrm{GeV}$).

Nevertheless, owing to the behaviour of the electron requests (see § 4.4.2), no lepton-oriented Level 2 requirements can be applied together with purely calorimetric requests. This means that this Level 2 trigger path will enter Level 3 with an efficiency of 77.6% and a rate of 15.4 Hz, which, as anticipated on pag. 80, is an acceptable value.

4.5 Level 3

The guiding idea for the Level 3 selection consists of exploiting the better resolution achievable by a more sophisticated event reconstruction that allows a more discriminant lepton identification. This will be combined with more stringent calorimetric requirements.

4.5.1 Calorimetry

At Level 3, calorimetry requirements essentially are aimed at confirming the Level 2 requirements; this, in particular, means that events passing the Level 3 should have at least 3 jets[19] with a minimum transverse energy content of 10 GeV. Similarly, there will be a requirement on ΣE_T^{jet}, but the value of the cut will be decided after the lepton requirements in order to keep control of the rate.

4.5.2 Soft Lepton Tag

Lepton requirements follow directly from the Soft Lepton Tag (SLT) algorithm developed during Run I for the top analysis and whose details are described elsewhere (see § 3.2.5). The SLT is based on a two-fold procedure, designed to work differently on data and Monte Carlo; while data are treated applying the specific selections that will be recalled in the following sections, the Monte Carlo procedure identifies all signal leptons[20] produced in the event and that are within detector acceptance, associating each of them to a tagging efficiency that has been estimated on true leptons collected from suitable datasets. The Monte Carlo procedure has been modified with respect to the original SLT version in order to adapt it to the considered signal.

Since the SLT requirements were optimized for the top search, a check has been performed on the variables that could be affected by the different signal topology.

Electron tag

The electron selection is based on matching a track[21] with $P_T \geqslant 2\,\mathrm{GeV}/c$ with calorimetric quantities, tipically energy depositions in the CEM, CES and CPR detectors; at the same time, the quality of this matching has been taken into account by comparing the P_T and the extrapolated position of the track at the CES detector respectively with its

[19] Jets are reconstructed with a cone $R=0.4$

[20] Again, here a signal lepton is a lepton produced in the semileptonic decay of a B or D-hadron coming from a boson.

[21] Here a fully reconstructed track fulfilling standard quality criteria and fiducial requirements – i.e. extrapolating in the instrumented region of the CEM detector ($|\eta| \lesssim 1$).

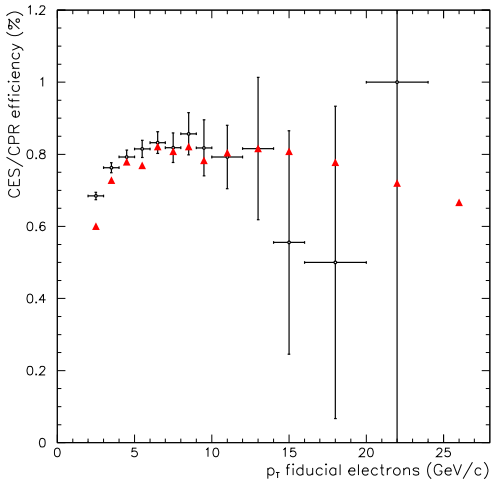

Figure 4.16: CES *and* CPR *combined efficiency as a function of track* P_T *for conversion electrons.*

electromagnetic tranverse energy deposition in the CEM calorimeter and the position of the matched cluster in the CES[22].

Soft electron requirements can be broadly divided into two classes according to their isolation dependence; in this way[23]:

- $|\Delta x_{CES}| \leqslant \max\{0.7\,\text{cm}, 1.82\,\text{cm} - 0.1867 \times \text{P}\}$
- $|\Delta z_{CES}| \leqslant 2\,\text{cm}$
- $E_{s_5}/P, E_{w_5}/P \geqslant \begin{cases} 0.24 + 0.03 \times P & \text{if } P \leqslant 12\,\text{GeV}/c \\ 0.6 & \text{if } P > 12\,\text{GeV}/c \end{cases}$
- $\chi^2_{strip}/6, \chi^2_{wire}/6 \leqslant 16$
- $Q_{CPR} \geqslant 4744 - 11592 \times (P/P_T) + 7923 \times (P/P_T)^2$

belong to the isolation-independent class. Therefore, their efficiency can be safely estimated from real data by means of a suitable sample of unbiased electrons (see crosses in fig. 4.16): for the purpose of cross-checking the efficiency quoted in [10] (triangles in fig. 4.16), the same conversion sample defined for Level 2 studies has been used. Looking at fig. 4.16, an efficiency enhancement has been observed at low P_T with respect to the standard SLT measurement; this is probably due to a higher purity of the conversion sample achieved by tagging the leading leg of each conversion by means of a trigger which requires XCES information. At the same time, in order to avoid the trigger bias, it has been necessary to remove from the unbiased sample all electrons extrapolating to a CEM tower already matched to a trigger electron. Furthermore, fig. 4.16 shows that conversion electrons do represent a source of background and that, therefore, a conversion veto[24] has to be included in the selection.

[22] A cluster in the CES detector is considered only if its wire and strip profiles are compatible with an electron cluster hypothesis.

[23] Expressing energies in GeV and P, P_T in GeV/c; Q_{CPR} is expressed in terms of ADC counts.

[24] Whose details are described in § 3.2.5.

On the other hand, considering the class of isolation-dependent quantities, the requirements:

- $0.7 \leqslant E_{em}/P \leqslant 1.5$
- $E_{had}/E_{em} \leqslant \begin{cases} 0.1 & \text{if } \textit{flat } E_{em}/P \text{ cut} \\ 0.05+\Sigma_p^{0.2}/E_{em} & \text{if } \textit{sliding } E_{em}/P \text{ cut} \end{cases}$

need to be studied on the signal Monte Carlo in order to keep into account the intrinsic dependence on the environment track density of the variables they are applied on. However, as a cross-reference, these quantities have been studied on the unbiased conversion electron sample as well (see fig. 4.17 for E_{em}/P and fig. 4.18 for E_{had}/E_{em}), without evidentiating remarkable discrepancies with respect to the Monte Carlo.

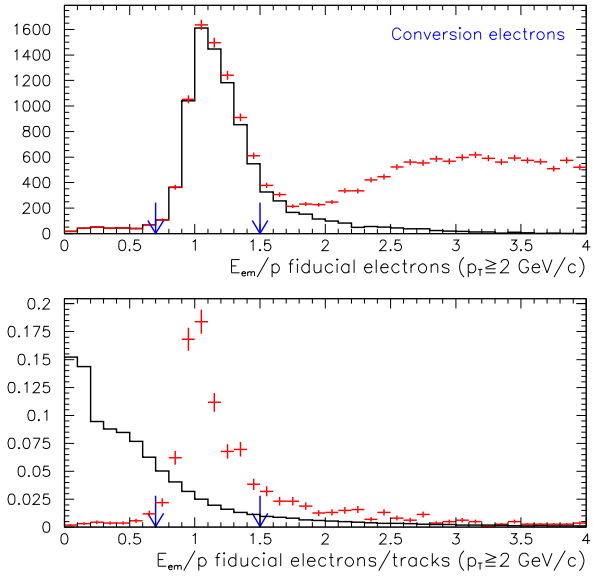

Figure 4.17: *Top: E_{em}/P for conversion electrons (crosses: all conversion soft legs; solid: conversion soft legs extrapolating to a* CEM *tower matched to a trigger electron have been removed). Bottom: E_{em}/P for $\mathrm{H^0V \to b\bar{b}q\bar{q}^{(\prime)}}$, $M_{\mathrm{H}} = 120\,\mathrm{GeV}/c^2$ (crosses) and* JET20 *(solid) samples.*

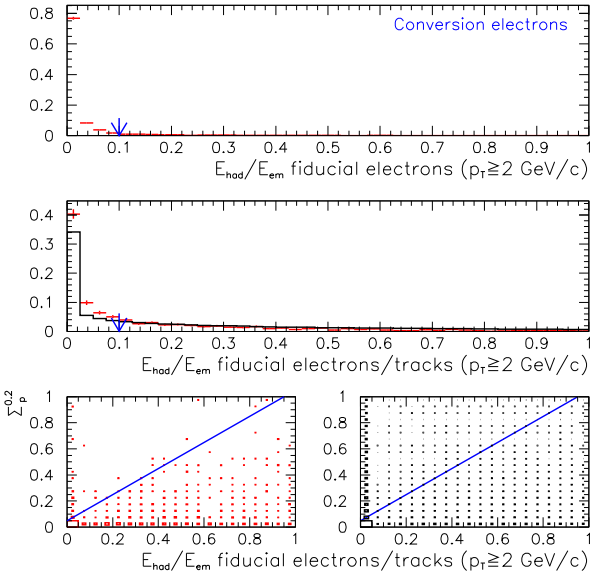

Figure 4.18: *Top: E_{had}/E_{em} (flat) for conversion electrons. Middle: E_{had}/E_{em} (flat) for $\mathrm{H^0V \to b\bar{b}q\bar{q}^{(\prime)}}$ ($M_{\mathrm{H}} = 120\,\mathrm{GeV}/c^2$) sample. Bottom: E_{had}/E_{em} vs. $\Sigma_p^{0.2}$ for for $\mathrm{H^0V \to b\bar{b}q\bar{q}^{(\prime)}}$, $M_{\mathrm{H}} = 120\,\mathrm{GeV}/c^2$ (left) and* JET20 *(right).*

The standard SLT algorithm includes also a cut on the $\mathrm{d}E/\mathrm{d}x$ (see § 3.2.5); in this context, however, this request has been kept separated from the others, since its isolation-dependence is still under study.

The procedure for computing the event tagging probability[25] is formally identical to the one used at Level 2 for the electron selection: four different possible alternatives have been examined, as a result of switching between the *flat* or *sliding* E_{had}/E_{em} cut and of turning on or off the $\mathrm{d}E/\mathrm{d}x$ requirement. Efficiencies and rate behaviours have then been monitored as a function of ΣE_T^{jet} and the results summarized in fig. 4.19.

[25] SLT electron tagging efficiencies (i.e. the 'triangles' of fig. 4.16) have been used.

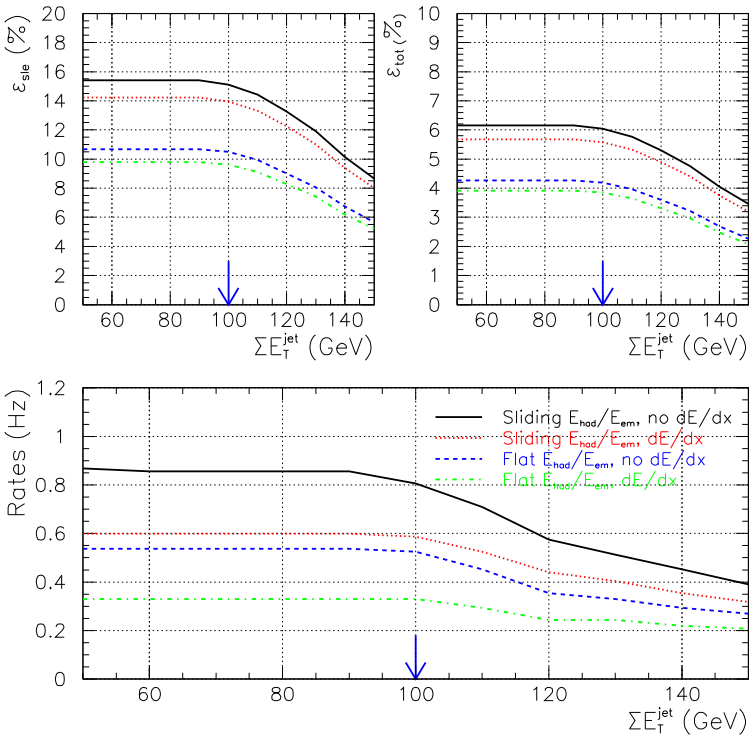

Figure 4.19: *Top: Level 3 efficiency computed on* $H^0V \to b\bar{b}q\bar{q}^{(\prime)}$ *($M_H = 120\,GeV/c^2$) events; events with a* $b \to e\nu_e X$ *or* $c \to e\nu_e X$ *decay (left) or all events (right). Bottom: rate calculated on* JET20 *sample. Both efficiency and rate are plotted in terms of* ΣE_T^{jet}.

Muon tag

At Level 3, the selection criteria follow directly from the SLT algorithm requirements; therefore, tracks[26], which are required to have $P_T \geqslant 2\,GeV/c$, are divided into four classes according to the muon detectors they extrapolate to (see [10]):

- CMUP: the track extrapolates within the fiducial volumes of both CMU and CMP
- CMP: the track extrapolates within the CMP fiducial volume and is not CMU-fiducial
- CMU: the track extrapolates within the CMU fiducial volume and is not CMP-fiducial
- CMX: the track extrapolates within the CMX fiducial volume

Once the track fiduciality has been defined, a track–stub matching procedure is performed, where essentially a stub is required for each detector the track is fiducial within; then, most of the muon requirements relate to the track–stub match that has been so far established[27]. Furthermore, the minimum ionizing requirement:

- $E_{had} - \Sigma_p^{0.2} < 6\,GeV/c$

has been asked for all muon candidates with $P_T > 6\,GeV/c$.

[26] As in the case of electrons, fully reconstructed tracks fulfilling standard quality requests are considered.

[27] Refer to § 3.2.5 or to [10] for details.

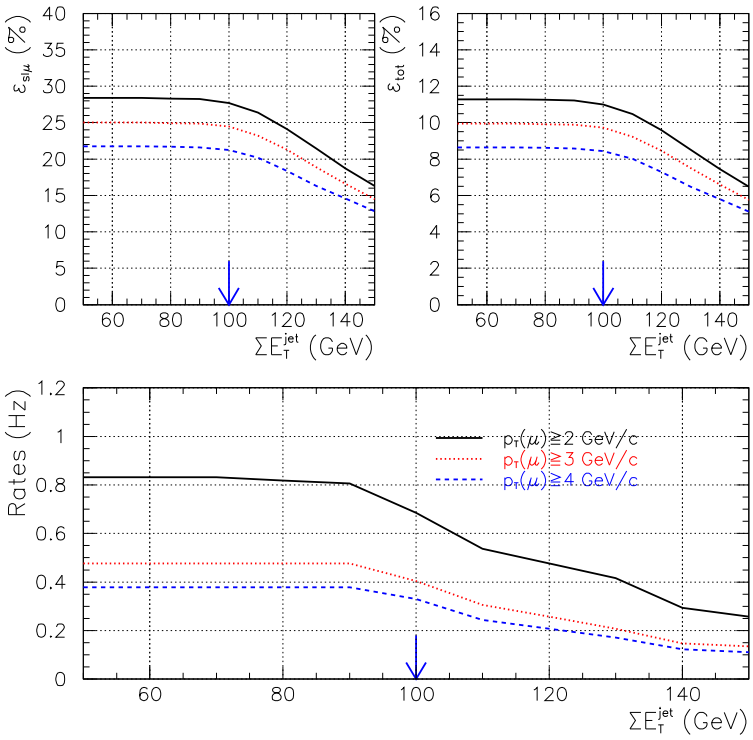

Figure 4.20: *Top: Level 3 efficiency computed on* $H^0V \to b\bar{b}q\bar{q}^{(\prime)}$ *($M_H = 120\,GeV/c^2$) events; events with a* $b \to \mu\nu_\mu X$ *or* $c \to \mu\nu_\mu X$ *decay (left) or all events (right). Bottom: rate calculated on* JET20 *sample. Both efficiency and rate are plotted in terms of* ΣE_T^{jet}.

The increase in acceptance of the CMX has been treated as in the case of Level 2 (see pag. 89). As in the case of electrons, soft muon tagging efficiencies evaluated for the $t\bar{t}$ analysis [3] have been used for computing the event tagging probabilities[28]. The results, in function of ΣE_T^{jet}, are shown in fig. 4.20.

4.5.3 Combined SLT

Once the soft lepton tagging procedure has been tested separately for electrons and muons, a combined strategy has to be defined for the Level 3 selection; at this point, when all possible primitives have already been defined (and, with them, their efficiency), the main problem is keeping the rate at an acceptable value (~ 1 Hz). In fig. 4.21, which has been obtained combining the two most efficient lepton requests (*sliding* E_{had}/E_{em} cut and no dE/dx requirement for electrons and $P_T(\mu) \geqslant 2\,GeV/c$ for muons) with all calorimetric requirements, the efficiency and rate behaviours are shown in terms of the cut value for ΣE_T^{jet}, which, at this point, represents the only 'free parameter' we can act on to reduce the rate.

The considered combination of single lepton primitives is acceptable in terms of rate for $\Sigma E_T^{jet} \geqslant 100\,GeV$; for this situation, values for the efficiencies and the rate are reported in table 4.3.

[28] Same procedure used previously for Level 2 and in the case of electrons.

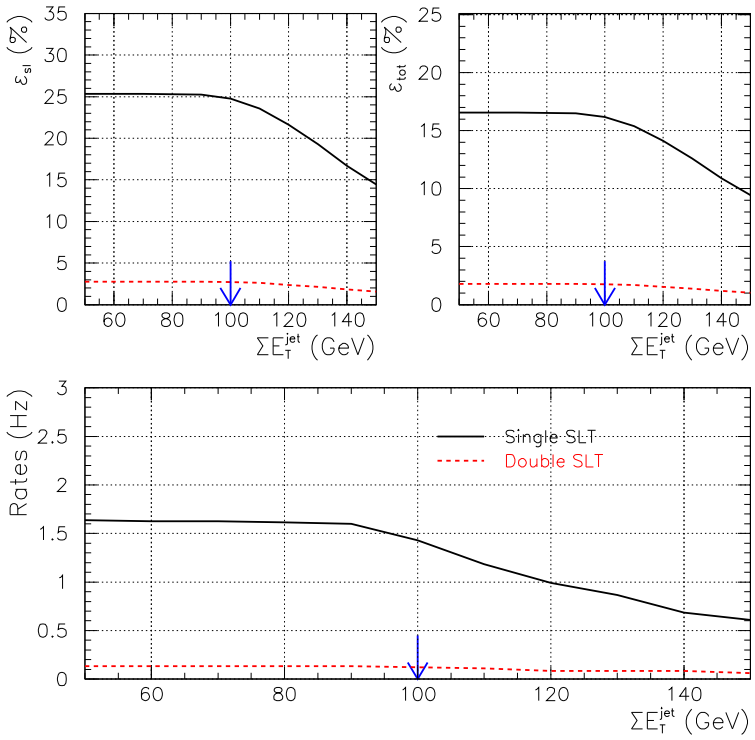

Figure 4.21: *Top: Level 3 efficiency computed on* $H^0V \to b\bar{b}q\bar{q}^{(\prime)}$ *($M_H = 120\,GeV/c^2$) events; events with a* $b \to \ell\nu_\ell X$ *or* $c \to \ell\nu_\ell X$ *decay (left) or all events (right). Bottom: rate calculated on* JET20 *sample. Both efficiency and rate are plotted in terms of* ΣE_T^{jet}.

Selection	**Efficiency**	**Rate** (JET20)
Single SLT	24.8% (16.2%)	1.43 Hz
Double SLT	2.71% (1.77%)	0.122 Hz

Table 4.3: *Level 3 event efficiencies and rate for* $\Sigma E_T^{jet} \geqslant 100\,GeV$ *(efficiencies are computed on* $H^0V \to b\bar{b}q\bar{q}^{(\prime)}$ *($M_H = 120\,GeV/c^2$) with respect to events with a* $b \to \ell\nu_\ell X$ *or* $c \to \ell\nu_\ell X$ *decay – efficiencies on inclusive sample are indicated in brackets).*

4.6 Summary

In summary, the proposal for a multijet trigger for (SM) Higgs associated production with a vector boson, especially aimed at tagging the leptons produced in the semileptonic decays of their B and D-hadrons, consists of the following requirements:

LEVEL 1: single trigger-tower $E_T^{tow} \geqslant 10\,GeV$

LEVEL 2: $\Sigma E_T 10 \geqslant 90\,GeV$, $N_{cl} \geqslant 3$ $(E_T^{cl} \geqslant 10\,GeV)$

LEVEL 3: $\Sigma E_T^{jet} \geqslant 100\,GeV$, $N_{jet}^{0.4} \geqslant 3$ $(E_T^{jet} \geqslant 10\,GeV)$, soft electron OR muon tag

The total efficiency, including the effects due to the increased CMX acceptance in Run II, is 16.2%, corresponding to a rate of 1.43 Hz ($\mathcal{L}_{inst}=1\times10^{32}\,\mathrm{cm}^{-2}\mathrm{s}^{-1}$). The efficiency value obtained on a $\mathrm{H^0V}\to\mathrm{b\overline{b}q\overline{q}^{(\prime)}}$ signal (a 15.6% is estimated when the CMX upgrade is not taken into account) is therefore comparable to the result achieved by the SLT algorithm[29] on a ℓ+*jets* $\mathrm{t\overline{t}}$ signal with similar jet multiplicity (15.6%, see [11]). Table 4.4 reports the behaviour of the efficiency for the SLT-multijet trigger as a function of the Higgs mass.

M_{H} [GeV/c^2]	**Efficiency** [%]	
		+CMX ext
110	13.9	14.3
120	15.6	16.2
130	16.6	17.3

Table 4.4: *Event efficiencies for* SLT*-multijet trigger computed on inclusive* $\mathrm{H^0V}\to\mathrm{b\overline{b}q\overline{q}^{(\prime)}}$ *samples as functions of* M_{H}.

The obtained results refer to a situation where a full track reconstruction scenario has been assumed at Level 3; further investigations, aimed at considering a less sophisticated event reconstruction at Level 3 – such as regional reconstruction –, as well as at monitoring the trigger dependencies from instantaneous luminosity, are in progress.

[29] In the $\mathrm{t\overline{t}}$ case, the E_{had}/E_{em} *flat* cut has been used.

Bibliography

[1] M. Carena, J. S. Conway, H. E. Haber, J. D. Hobbs *et al.*, (The Fermilab Higgs Working Group), *Report of the Higgs Working Group*, HEP-PH/0010338, Oct 2000.

[2] J. Benlloch, W. Bokhari, J. Friedman, L. Rosenson, P. Sphicas, *"The multijet data sample"*, CDF internal note 2916, Dec 1994.

[3] F. Abe *et al.* (The CDF Collaboration), *"Evidence for top quark production in* $\mathrm{p\overline{p}}$ *collisions at* $\sqrt{s}=2\,\mathrm{TeV}$*"*, *Phys. Rev.* **D 50**, 2966 (1994).

[4] J. Troconiz, R. Vilar, J. Valls, *"Search for Higgs Bosons Produced in Association with a Vector Boson in* $\mathrm{p\overline{p}}$ *Collisions at 1.8*$\,\mathrm{TeV}$*"*, *Phys. Rev. Lett.* **81**, 5748 (1998).

[5] M. Albrow *et al.* (The CDF Trigger and Datasets Working Group), *Run-II Trigger Table and Datasets Plan*, CDF internal note 4718, Aug 1998.

[6] J. Troconiz, J. A. Valls, R. Vilar, *Update in the Search for a Neutral Heavy Scalar in the Multijet Data Sample*, CDF internal note 4129, Nov 1997.

[7] M. Tanaka, Private Communication.

[8] S. P. Pappas *et al.*, *"Run 1B Low* p_T *Central Dimuon Trigger Efficiencies*, CDF internal note 4076, Feb 1997.

[9] The CDF II Collaboration, *"The CDF II Detector Technical Design Report"*, FERMILAB-PUB-96-390-E, Oct 1996.

[10] C. Campagnari, D. Kestenbaum, *"Review of the SLT Algorithm for Run 1b"*, CDF internal note 3682, May 1996.

[11] G. Apollinari *et al.*, *"Measurement of the* $\mathrm{t\overline{t}}$ *production cross section using SLT tags.*, CDF internal note 3861, Nov 1996.

Chapter 5

Characterization of Higgs*strahlung* events

This Chapter is devoted to a characterization of the sample selected with the multijet trigger described in the previous chapter in terms of kinematical characteristics, background contribution and signal-to-background ratio (S/B). The effect of requiring the presence of b-tagged jets not only via SLT but also via SVX-based tagging algorithms (SECVTX) will be studied. Moreover, a possible choice of kinematic variables that can be used in increasing the S/B is presented.

Mass reconstruction will be performed as a function of the b-tag information. In particular it will be shown how a specific set of jet corrections developed for b-jets containing a semileptonic decay can improve the mass resolution. A preliminary estimate of the achievable S/B using a parameterization of Run II tagging and tracking efficiencies and a preliminary kinematical selection is given at the end, compared to the expectation from the Run II Higgs Working Group findings.

5.1 The trigger-selected sample

The sample considered here has been selected with the multijet trigger described in chapter 4, whose requirements can be summarized as follows:

LEVEL 1
- $\diamond$ Single tower with $E_T \geqslant 10\,\mathrm{GeV}$

LEVEL 2
- $\diamond$ $N_{cl} \geqslant 3$ ($E_T^{cl} \geqslant 10\,\mathrm{GeV}$)
- $\diamond$ $\Sigma E_T^{cl} \geqslant 90\,\mathrm{GeV}$

LEVEL 3
- $\diamond$ $N_{jet}^{0.4} \geqslant 3$ ($E_T^{jet} \geqslant 10\,\mathrm{GeV}$)
- $\diamond$ $\Sigma E_T^{jet} \geqslant 100\,\mathrm{GeV}$
- $\diamond$ one soft lepton tag ($P_T \geqslant 2\,\mathrm{GeV}/c$)

The total efficiency on the signal for $M_\mathrm{H} = 120\,\mathrm{GeV}/c^2$ amounts to 15.6% (16.2% when including the CMX extension) with a trigger rate $\mathcal{R} = 1.43\,\mathrm{Hz}$, corresponding to a cross section of 14.3 nb for $\mathcal{L}_{inst} = 10^{32}\,\mathrm{cm}^{-2}\mathrm{s}^{-1}$ ($\sigma = \mathcal{R}/\mathcal{L}_{inst}$). Since for $M_\mathrm{H} = 120\,\mathrm{GeV}/c^2$ the $\mathrm{H^0}+\mathrm{Z^0}/\mathrm{W^\pm}$ production cross section is $\sigma \times B.R.(\mathrm{H} \to \mathrm{b\bar{b}}) \times B.R.(\mathrm{V} \to \mathrm{q\bar{q}}) = 0.122\,\mathrm{pb}$, this implies that the signal-to-background ratio (S/B) at trigger level is about 1×10^{-6}, where

the background is almost totally due to QCD processes. Given the high fake rate of the SLT requirement, the heavy flavour content of the sample is of the order of 25% [1].

5.2 Data samples

Signal and JET20 data samples have already been described in § 4.2: $H^0V \to b\bar{b}q\bar{q}^{(\prime)}$ events – used for computing efficiencies – have been generated with PYTHIA for $M_H = 110, 120, 130\,\mathrm{GeV}/c^2$, while JET20 events have been collected by a loose trigger requiring a Level 2 cluster with $E_T^{cl} \geqslant 20\,\mathrm{GeV}$.

Background – Monte Carlo QCD

Since b-tagging is an essential step in multijet Higgs analyses, in the following the heavy flavour content will be studied on both signal and background samples; since, as previously mentioned, the heavy flavour content of the JET20 sample is expected to be limited, an additional background, consisting of QCD events with heavy flavour production is needed. A large sample of events ($\sim 2M$) has been generated with PYTHIA for $2 \to 2$ QCD process; initial and final state radiation phenomena contribute to provide the topology needed for trigger acceptance. In order to reduce production time, only events where heavy flavour production occurred ($N_{c-quark} + N_{b-quark} \geqslant 1$) were fed to the detector and Run II trigger simulations (QFL and RUN2TRS); subsequently, only events fulfilling the Level 2 multijet calorimetric requirements (see § 4.4.1) have been saved on disk, reducing in this way the disk space needed for storing. The collected statistics (18544 events) corresponds to an integrated luminosity of $0.34\,\mathrm{pb}^{-1}$.

5.3 Signal Topology

Before proceeding to the identification of b-jets and, subsequently, to invariant mass studies, it is important to find an event topology consistent with the process $H^0V \to b\bar{b}q\bar{q}^{(\prime)}$, by means of which signal events can be characterized. As explained in chapter 3, the clustering procedure used for jet definition relies on the simple idea that reconstructed jets should ideally resume the final state parton configuration of each event. However, several reasons may affect the observable number of jet (and their energies): threshold effects, connected to the finite cutoff values that explicitly enter the definition of jets, jet merging, *id est* the possibility that two or more jets fall within the same searching cone, and finite geometrical acceptance would reduce the number of jets; at the same time, radiation processes can give rise to the opposite effect, that is, additional jets in the final state. The resulting picture, for both signal and background, is described in fig. 5.1, where the situation refers to the following conditions:

- ◇ Clustering cone radius: $R = 0.4$;
- ◇ $(E_T^{jet})_{raw} \geqslant 10\,\mathrm{GeV}$ [1];
- ◇ $|\eta^{detector}| \leqslant 2.4$.

[1] $(E_T^{jet})_{raw}$ refers to uncorrected energies.

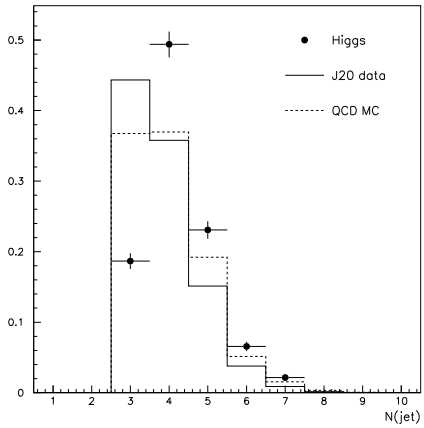

Figure 5.1: *Jet multiplicity distribution for signal ($H^0V \to b\bar{b}q\bar{q}^{(\prime)}$, $M_H = 120\,\mathrm{GeV}/c^2$) and backgrounds (JET20, QCD) after trigger selection (arbitrary normalization).*

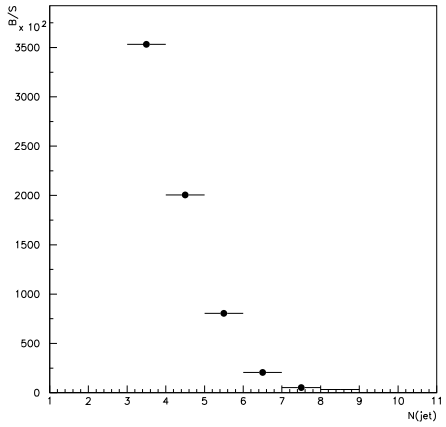

Figure 5.2: *Background/Signal ratio as a function of N_{jet} after trigger selection. The ratio B/S has been computed on the basis of the* JET20 *background sample.*

Therefore, although in an ideal picture one would expect the four leading jets corresponding to the four final partons produced in the decay of the H^0V system, the various effects that have just been discussed dilute this piece of information: hence, the correct interpretation of the four leading jets in terms of 'signal' partons[2] is matched in the $\sim$65% of the cases. The requirement $N_{jet} \geqslant 4$ is 81.3% efficient on the signal and has an acceptance of 56.8% on the background; this is shown, in terms of background-to-signal ratio (B/S), in fig. 5.2.

After requiring $N_{jet} \geqslant 4$, the E_T spectra for the four leading jets have been studied: fig. 5.3 shows the corresponding distributions for signal and backgrounds when the jet E_T are fully corrected for geometry and detector effects, according to the corrections described in § 3.2.4. This change, that will be assumed from now on, will affect also the kinematical variables that will be studied, since these essentially rely upon jets energies and directions.

At the same time, at this level a minimum separation between jets ($\Delta R_{min} \geqslant 0.5$) has been required in order to permit a clean jet reconstruction even within dense events, where the performance of the jet clustering algorithm may be degraded. In any case, the impact of this cut is minimal, given its extreme efficiency: $\epsilon(\Delta R_{min} \geqslant 0.5) = 97.1\%$.

5.3.1 Identification of b-jets

As previously mentioned, $H^0 \to b\bar{b}$ represents the dominant H^0 decay mode when a light Higgs hypothesis is assumed; this has been implicitly taken into account during signal generation, when the Higgs boson decay is forced into a $b\bar{b}$. Therefore, the signal sample always contains at least two b quarks from the decay of the Higgs boson; extra heavy flavour (b or c) contributions can be as well provided by vector boson decays.

The identification of heavy flavour jets will concern the four leading jets only, as suggested by their interpretation in terms of the partons directly produced in the bosons

[2]By this meaning the four partons directly connected to the decaying bosons.

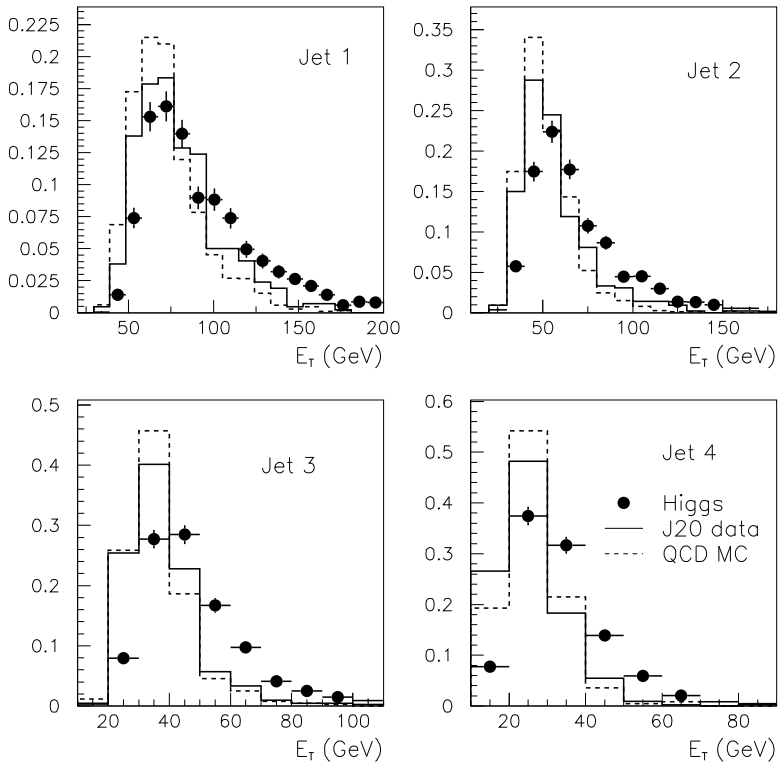

Figure 5.3: *E_T distribution of the four leading jets for signal ($H^0V \to b\bar{b}q\bar{q}^{(\prime)}$, $M_H = 120\,\mathrm{GeV}/c^2$) and backgrounds (JET20, QCD), after trigger selection (arbitrary normalization).*

decay. Heavy flavour-tagging techniques essentially rely on two peculiarities of b and c decays:

- ◇ as previously mentioned (see § 3.2.5), the decay of a D or B-hadron – respectively carriers of c and b flavours – is often ($\sim 20\%$ of the cases) accompanied by the emission of a lepton, usually embedded within the jet originated by the hadronic remnants of the decaying hadron and characterized by a low P_T spectrum;
- ◇ D and B-hadrons are massive and associated to large momenta; this, together with their relatively long lifetimes ($\sim 1 \div 1.5$ ps), results in decay lengths of the order of $c\tau \simeq 300 \div 500\,\mu$m, which become detectable by means of vertex detectors.

A brief description of the tagging procedures that will be used in the following is given.

Soft Lepton Tagging

The soft lepton tagging procedure, based upon the identification the non-isolated soft leptons (e or μ) produced in the semileptonic decays of D and B-hadrons, which has already been described beforehand in this work (see § 3.2.5 and chapter 4), can be used as a tagging tool for heavy flavour jets; relying on the mere fact that leptons produced in heavy flavour semileptonic decays are embedded into jets, a jet can be tagged as being originated from a b or c quark whenever a lepton is found within its cone, that is, when the $\eta - \phi$ distance between the direction of the lepton from the jet direction does not exceed 0.4.

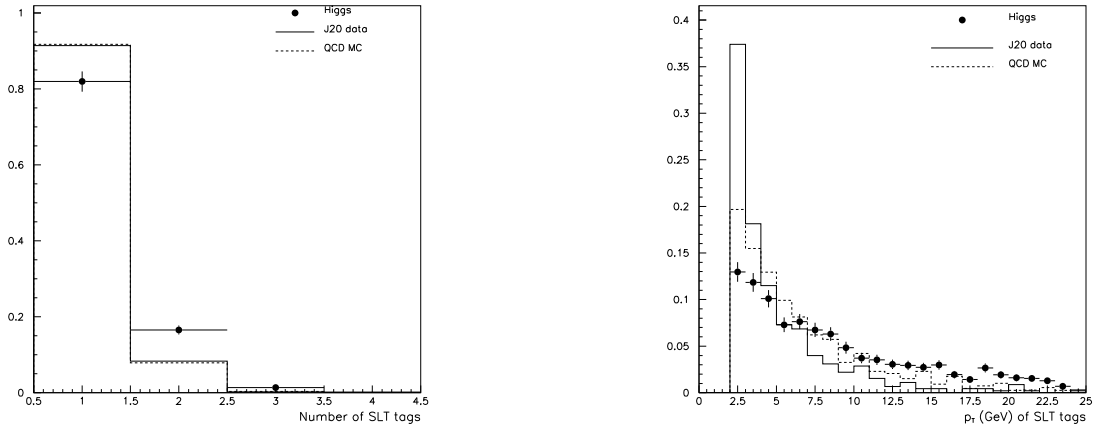

Figure 5.4: *Left: number of* SLT *tracks in signal* ($H^0V \to b\bar{b}q\bar{q}^{(\prime)}$, $M_H = 120\,\mathrm{GeV}/c^2$) *and background* (JET20, QCD) *events. Right:* P_T *distribution of the* SLT*-tagged tracks in the same samples. Both plots refer to samples being selected by the* SLT*-multijet trigger with the* $N_{jet} \geqslant 4$ *requirement.*

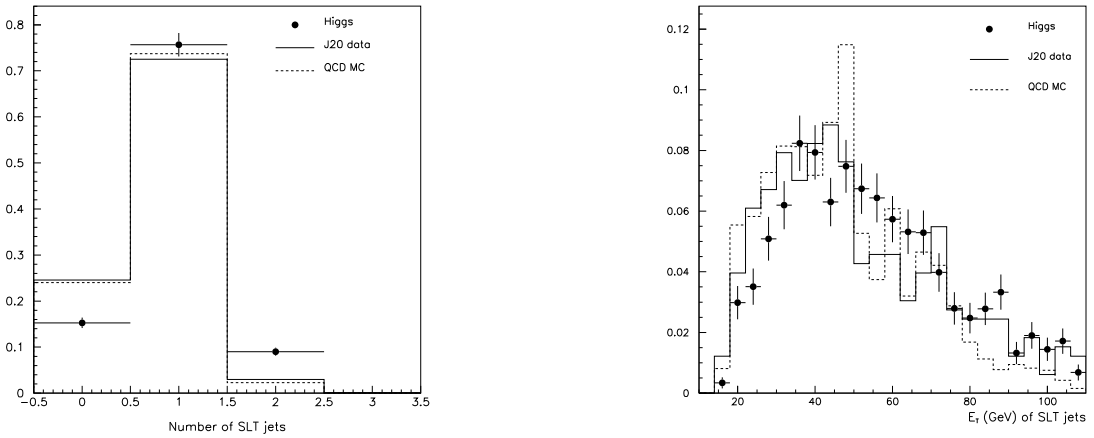

Figure 5.5: *Left: number of* SLT*-tagged jets (four leading only) per event. Right:* E_T *distribution for* SLT*-tagged jets. Both plots refer to* $H^0V \to b\bar{b}q\bar{q}^{(\prime)}$ ($M_H = 120\,\mathrm{GeV}/c^2$) *signal and* JET20, QCD *background samples after trigger selection and* N_{jet} *requirement.*

As shown in chapter 4, the SLT algorithm is characterized by an overall efficiency (electrons and muons) of 16.2%; this value takes into account the increase in acceptance expected for Run II due to the CMX extended coverage (by a factor ~ 1.5 – see § 3.1.1). In the following, however, Run I geometry will be assumed; consequently, an efficiency of 15.6% will be considered for the trigger selection.

The number of SLT tracks expected per event in signal and background samples is depicted in fig. 5.4, where also their P_T distribution is shown. The criteria used for selecting electron candidate tracks follow the scheme of the Level 3 electron primitive, where the $\mathrm{d}E/\mathrm{d}x$ is not included to accomplish for the possible unavailability of suitable calibrations of the COT at trigger level; however, jet tagging by means of a SLT track will include the $\mathrm{d}E/\mathrm{d}x$ for electrons. In fig. 5.5, the number of SLT-tagged jets per event is shown together with their E_T spectrum.

The SLT algorithm has been designed for the dense environment of high P_T b-jets in $t\bar{t}$ events; apart from efficiency, a crucial feature of the procedure is therefore fake rejection. Despite a fake rate per track of $\lesssim 1\%$, only 25% of the events with three or more jets that have been selected by means of a soft lepton tag presents a heavy flavour content.

Secondary vertex reconstruction

Secondary vertices are reconstructed by means of an algorithm (SECVTX) optimized for high background rejection and high acceptance for real b-jets. The reconstruction of a secondary vertex embedded in a jet occurs on a track-basis, where, among the tracks enclosed within the jet cone, the ones that are actually considered must fulfill the following quality criteria:

- $P_T > 0.5$ GeV/c;
- impact parameter significance[3] $S_d > 2.5$;
- hits in at least two layers of the SVX.

Tracks passing these requirements are ranked according to number of SVX hits, P_T and S_d; starting from the first ('best') two tracks, an iterative procedure searches for common vertices (*seed* vertices), located where the trajectories of two tracks cross in the transverse plane. Once a seed vertex has been found, the impact parameter of all the other tracks is recomputed with respect to the it: all tracks with $S_d^{seed} < 3$ are then associated to the seed vertex. If no vertex associated to three or more tracks is found, a second iteration begins. This time, a new list of tracks, fulfilling more restrictive quality requirements, is compiled:

- $P_T > 1.5$ GeV/c;
- $S_d > 4.0$;
- hits in at least three layers of SVX.

As in the first loop, starting from the first tracks in the list, the procedure scans all possible track pairs compatible with being originated from a common vertex.

At the end of the procedure, tagged vertices are classified according to the reconstructed decay length L_{xy} in the transverse plane, computed as the distance between primary (see par. 3.2.3) and secondary vertex. A 'good' tag corresponds to requiring L_{xy} being significantly greater than zero, $|L_{xy}|/\sigma_L > 3$. For the classification of the secondary vertex, it is useful to give a sign to the value of L_{xy}: the decay length is given the sign of the scalar product between the vector pointing from primary to secondary vertex and the vector obtained as the sum of the momenta of all tracks fitted to the secondary vertex (see fig. 5.6). Ideally, if the vertex tags the location of a real heavy quark decay, the sign of the decay length is positive[4] while negative decay lengths are mostly due to fake vertices.

[3]The impact parameter significance of a charged track is defined as $S_d = |d|/\sigma_d$, where d is impact parameter of the track and σ_d is the uncertainty in its determination, obtained from the uncertainty in the track helix parameters and the resolution on the location of the primary vertex in the xy plane.

[4]Actually, misreconstruction leads to negative decay lengths in 6% of true heavy flavour decays; this occurs mainly when tracks from a b vertex are fitted together with tracks from a c vertex or when tracks have a low P_T spectrum.

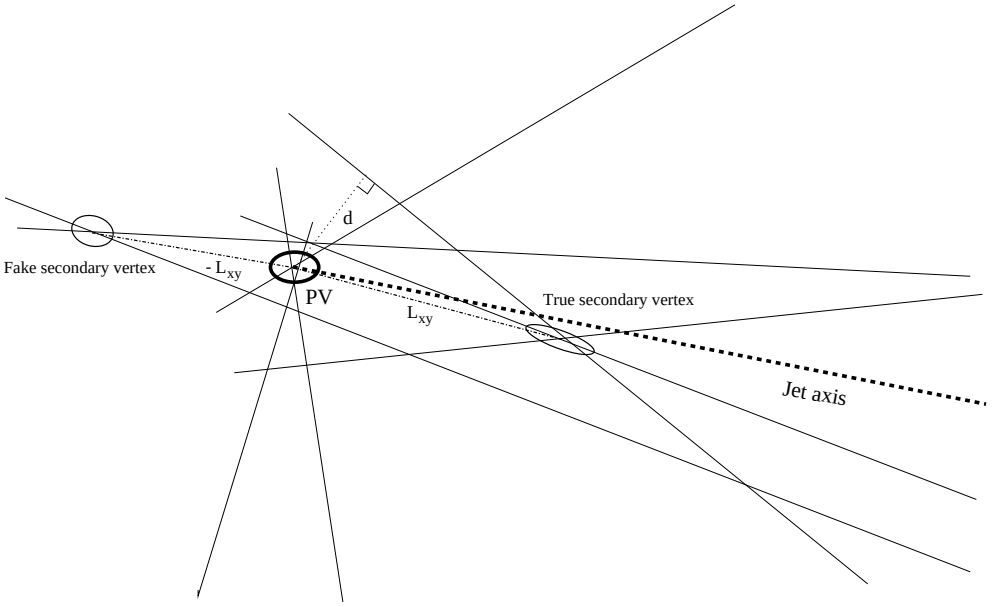

Figure 5.6: *Secondary vertex reconstruction (*SECVTX*).*

Two-track vertices consistent with coming from γ-conversions or from K^0_S or Λ decays are removed according to their location[5], track charge and their invariant mass.
Finally, a jet containing a vertex associated to a significantly positive decay length is called a b-tagged jet.

As for SLT-tagging, SVX-tagging is considered only among the leading four jets; the number and the E_T distribution of SVX-tagged jets in signal and background events after SLT-multijet trigger and N_{jet} selection is shown in fig. 5.7.

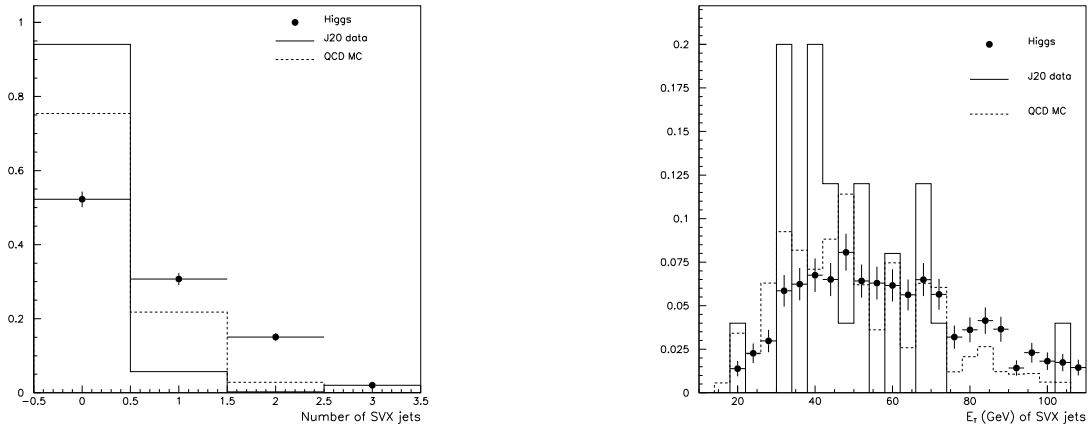

Figure 5.7: *Left: number of* SVX*-tagged jets (leading four only) per event. Right: E_T distribution for* SVX*-tagged jets. Both plots refer to* $H^0V \to b\bar{b}q\bar{q}^{(\prime)}$ *($M_H = 120\,\mathrm{GeV}/c^2$) signal and* JET20*,* QCD *background samples after trigger selection and N_{jet} requirement.*

[5]Conversions can be efficiently rejected by requiring the secondary vertex to lie inside the innermost layer of SVX, while K^0_S and Λ decays occurrence can be limited by requiring L_{xy} to be inconsistent with the corresponding $c\tau$ values.

Conversely to the SLT algorithm, whose performances suffer also from the limited branching ratio characterizing $b \to \ell\nu_\ell X$ and $b \to c \to \ell\nu_\ell X$ decays, SECVTX achieves a high efficiency ($\sim 30\%$) on selecting b-jets combined with high sample purity (for instance 70% in a high P_T inclusive jet sample).

5.3.2 b-tagging selection

The information contained in figures 5.5 and 5.7 is summarized in tab. 5.1, which reports signal efficiencies as well as background acceptances. The most promising signatures in the hadronic decay mode of H^0V consists of two b-tagged jets, since this is a very good handle for getting rid of the huge background of multijet events; for this reason, apart from the double SECVTX tagging, which has been used in the Run I analysis (see [2]), the possibility of reaching the double tag by means of any of the two b-tagging procedures described above (SLT and SECVTX) has been investigated.

Selection	**Efficiency** (%)			**Acceptance** (%)	
	M_H [GeV/c^2]			**JET20**	**QCD**
	110	120	130		
Trigger	13.9	15.6	16.6	–	–
$N(jet)$, ΔR_{min} [6]	11.0 (79.1)	12.3 (79.0)	13.5 (81.2)	54	61
$N(\text{SLT}) \geqslant 1$	9.23 (66.5)	10.5 (66.9)	11.6 (69.5)	41	46
$N(\text{SVX}) \geqslant 1$	5.14 (37.0)	5.90 (37.8)	6.68 (40.1)	3.0	15
$N(\text{SVX}) \geqslant 2$	1.66 (12.0)	2.11 (13.5)	2.37 (14.2)	0.10	1.7
$N(\text{SVX, SLT}) \geqslant 2$	3.46 (24.9)	4.03 (27.2)	4.57 (27.5)	2.6	5.2

Table 5.1: *Selection (b-tagging) efficiency on* $H^0V \to b\bar{b}q\bar{q}^{(\prime)}$ *events for different* M_H *values and acceptances for* JET20, QCD *background samples. Efficiencies are calculated with respect to the generated samples, while acceptances are computed with respect to trigger output; for reference, efficiencies with respect to trigger output have been quoted in brackets.*

Efficiency alone predicts the number of expected signal events in the final sample, but does not provide information of the significance of these events with respect to background events that at the same time are selected by the various requirements. This can be understood in terms of signal-to-background ratios (S/B) and significance ($S/\sqrt{B}$) calculated on the selected signal and background samples (see tab. 5.2). Due to its low purity, the possibility of double tagging events by means of the SLT procedure only has not been reported.

As can be seen in tab. 5.2, the SVX double tagging procedure – as expected – leads to the highest significance; however, one hopes to gain further separation by considering the invariant mass spectra of the two b-tagged jets (M_{bb}) and of the remaining two jets[7] (M_{jj}); for this reason the extra efficiency from the mixed (SVX,SLT) double tag can be useful.

[6] $N_{jet} \geqslant 4$, $\Delta R_{min} \geqslant 0.5$.

[7] As in the tagging procedure, only the four leading jets are considered when mass reconstruction is taken into account in order to reduce the combinatorial background.

$\mathcal{L}_{int}$ [fb^{-1}]	Selection	Expected events				S/B ($\times 10^{-5}$)			$S/\sqrt{B}$ ($\times 10^{-2}$)		
		M_H [GeV/c^2]			JET20	M_H [GeV/c^2]			M_H [GeV/c^2]		
		110	120	130	($\times 10^6$)	110	120	130	110	120	130
2	$N(\text{SVX}) \geqslant 2$	6.2	5.2	3.4	0.028				3.7	3.3	2.0
	$N(\text{SVX, SLT}) \geqslant 2$	13	10	6.6	0.73				1.5	1.2	0.77
10	$N(\text{SVX}) \geqslant 2$	31	26	17	0.14	22	19	12	8.3	6.9	4.5
	$N(\text{SVX, SLT}) \geqslant 2$	65	52	33	3.7	1.8	1.4	0.90	3.4	2.7	1.7
30	$N(\text{SVX}) \geqslant 2$	93	78	51	0.42				14	12	7.9
	$N(\text{SVX, SLT}) \geqslant 2$	195	150	99	11				5.9	4.5	3.0

Table 5.2: *Summary of b-tagging selection predicted performances. Expected number of events refer to* $H^0V \to b\bar{b}q\bar{q}^{(\prime)}$ *signal and* JET20 *background samples.*

5.4 Kinematical selection

In this section a tentative characterization of $H^0V \to b\bar{b}q\bar{q}^{(\prime)}$ events will be studied in terms of kinematical observables; while the b-tagging selection reported in the previous section, due to its high purity, sets the order-of-magnitude scale achievable in terms of signal efficiency and significance, a kinematical selection is meant to provide a refinement in the process of signal discrimination. Since the SLT-multijet trigger is characterized by looser calorimetry requirements with respect to the Run I multijet trigger used for Higgs searches in the fully hadronic final state, new kinematical variables have been considered with respect to the old analysis. Due to the fact that double b-tagging severely affects the statistics of the background samples, the kinematical studies will be performed starting on the trigger-selected samples; at the end, however, results for the combination of the two selections will be given.

5.4.1 Global variables

After the jet structure of each event has been defined, global kinematical variables can be constructed from jet quantities. Several kinematical variables have been studied with the aim of selecting the most discriminant ones, that is, the ones which can provide an effective enhancement in the signal-to-background ratio before the additional b-tagging requirement.
Among the studied variables, the most interesting ones are:

- $\Sigma E_T = \Sigma_{i=1}^{N_{jet}} (E_T^{jet})_i$, the scalar sum of the jet transverse energies, see fig. 5.8;
- $\Sigma_3^N E_T = \Sigma_{i=3}^{N_{jet}} (E_T^{jet})_i$, the scalar sum of the energies of all but the two jets with highest E_T, see fig. 5.9;
- $\Sigma E_T/\sqrt{\hat{s}}$, that characterizes the centrality of the energy flux, being $\hat{s} = x_1 x_2 s$ the fraction of s carried by the colliding partons[8], see fig. 5.10;

[8]Given s, the square of the $p\bar{p}$ center of mass energy ($\sqrt{s} = 2$ TeV), the Bjorken x variables are connected to observable quantities by the relation $x_{1,2} = (\Sigma E \pm \Sigma P_z)/\sqrt{s}$.

◇ t_4, the thrust value of the four leading jets in their center of mass frame of reference, see fig. 5.11. The value of t_4 is given by the expression:

$$t_4 \equiv \max_{\hat{\boldsymbol{n}}} \frac{\Sigma \boldsymbol{P} \cdot \hat{\boldsymbol{n}}}{\Sigma P} \ ;$$

the sum is extended to the leading four jets, whose momenta in their center of mass frame of reference have been indicated as $\boldsymbol{P}$. Note that the boost prevents unknown Bjorken x_1 and x_2 from being involved in the computation.

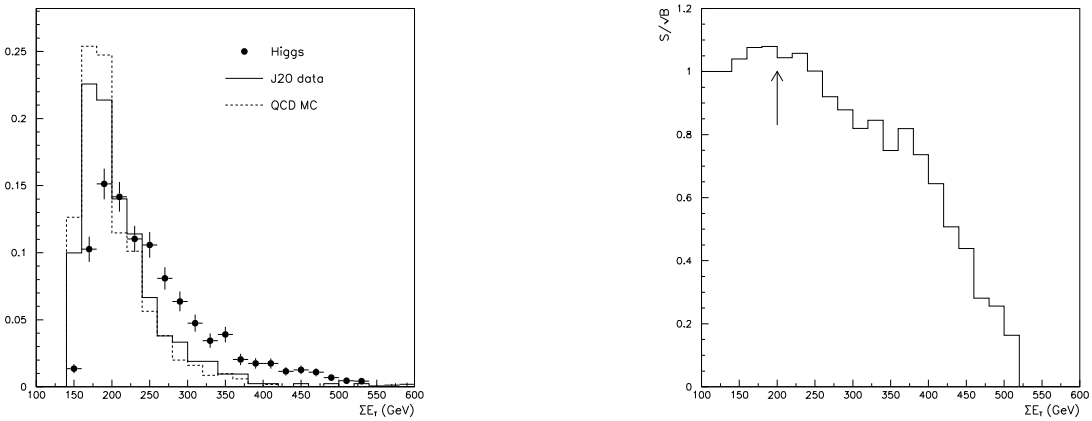

Figure 5.8: *Left:* ΣE_T *distribution for signal* $\mathrm{H^0V} \to \mathrm{b\overline{b}q\overline{q}}^{(\prime)}$ *($M_\mathrm{H} = 120\,\mathrm{GeV}/c^2$) and background (*JET20 *and* QCD*) samples (arbitrary normalization). Right: $S/\sqrt{B}$ ratio as a function of ΣE_T computed with respect to* JET20 *background.*

Among the kinematical variables that have been considered, the ΣE_T (see fig. 5.8) has to be handled with care: according to its significance (that is, the $S/\sqrt{B}$ ratio), maximum discrimination between signal and background can be achieved by requiring that $\Sigma E_T \geqslant 200\,\mathrm{GeV}$; this, however, although producing an enhancement in the S/B ratio, would result in a *a posteriori* drawback when, after the kinematical selection and the b-tagging, dijet invariant mass spectra M_{jj} for signal and background will be compared: a tight cut on ΣE_T – strongly correlated to M_{jj} – would inevitably induce a bias in these spectra, which would eventually look more similar among them – and would therefore be less separable – in the low mass ($\sim M_\mathrm{V}, M_\mathrm{H}$) region. For this reason, a preference has been given to kinematical variables that can increase the signal significance without biassing the dijet mass spectrum towards high values.

The variable $\Sigma_3^N E_T$ is expected to show a weaker correlation with respect to the final dijet invariant mass spectra, since in QCD $2 \to 2$ events, non leading jets are expected to emerge from radiation phenomena with a softer energy spectrum than jets produced in the decay of massive objects. As can be seen from fig. 5.9, the maximization of $S/\sqrt{B}$ leads to the requirement $\Sigma_3^N E_T \geqslant 60\,\mathrm{GeV}$.

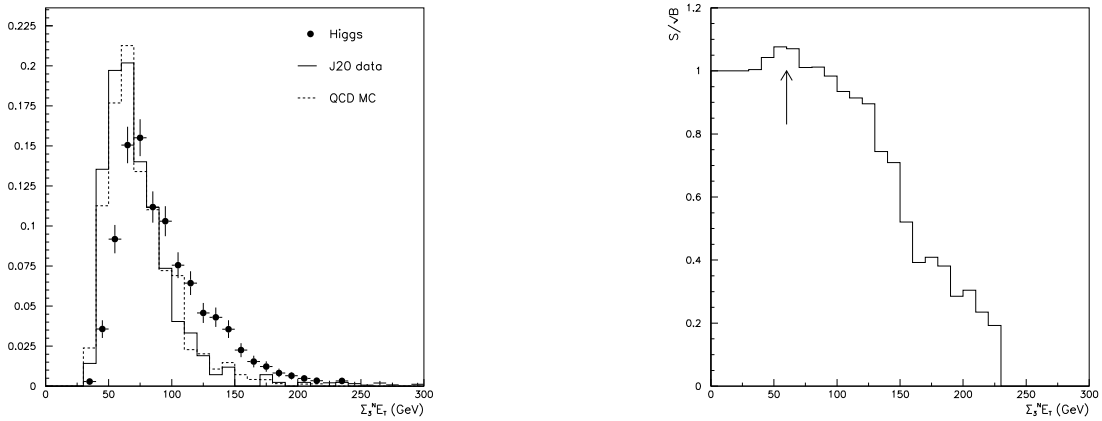

Figure 5.9: *Left:* $\Sigma_3^N E_T$ *distribution for* $\mathrm{H^0V \to b\overline{b}q\overline{q}^{(\prime)}}$ *(*$M_{\mathrm{H}} = 120\,\mathrm{GeV}/c^2$*) and background (*JET20, QCD*) samples (arbitrary normalization). Right:* $S/\sqrt{B}$ *ratio as a function of* $\Sigma_3^N E_T$ *computed with respect to* JET20 *background.*

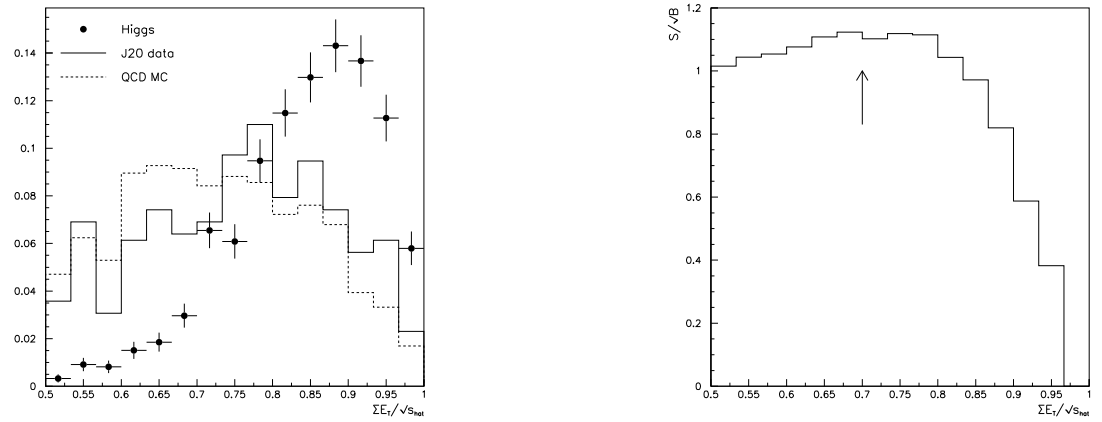

Figure 5.10: *Left:* $\Sigma E_T/\sqrt{\hat{s}}$ *distribution for* $\mathrm{H^0V \to b\overline{b}q\overline{q}^{(\prime)}}$ *(*$M_{\mathrm{H}} = 120\,\mathrm{GeV}/c^2$*) and background (*JET20, QCD*) samples (arbitrary normalization). Right:* $S/\sqrt{B}$ *ratio as a function of* $\Sigma E_T/\sqrt{\hat{s}}$ *computed with respect to* JET20 *background.*

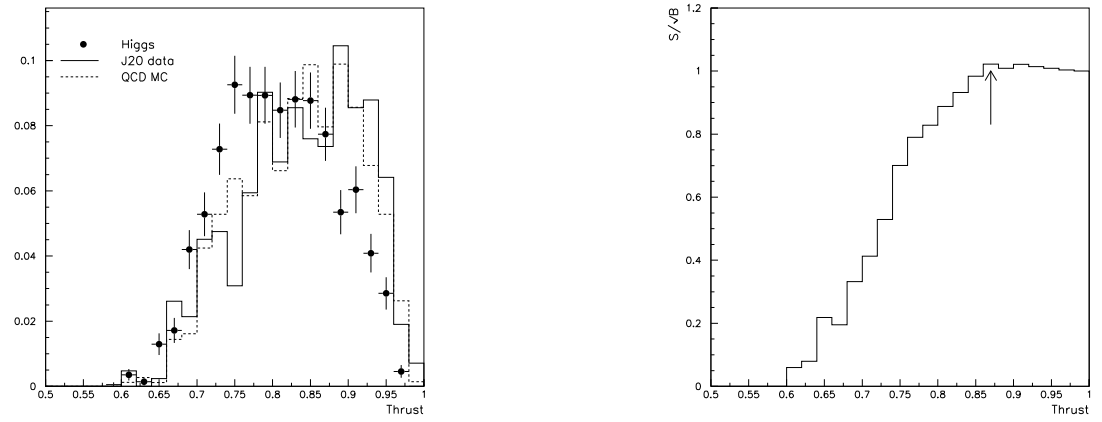

Figure 5.11: *Left:* t_4 *distribution for* $\mathrm{H^0V \to b\overline{b}q\overline{q}^{(\prime)}}$ *(*$M_{\mathrm{H}} = 120\,\mathrm{GeV}/c^2$*) and background (*JET20, QCD*) samples (arbitrary normalization). Right:* $S/\sqrt{B}$ *ratio as a function of* t_4 *computed with respect to* JET20 *background.*

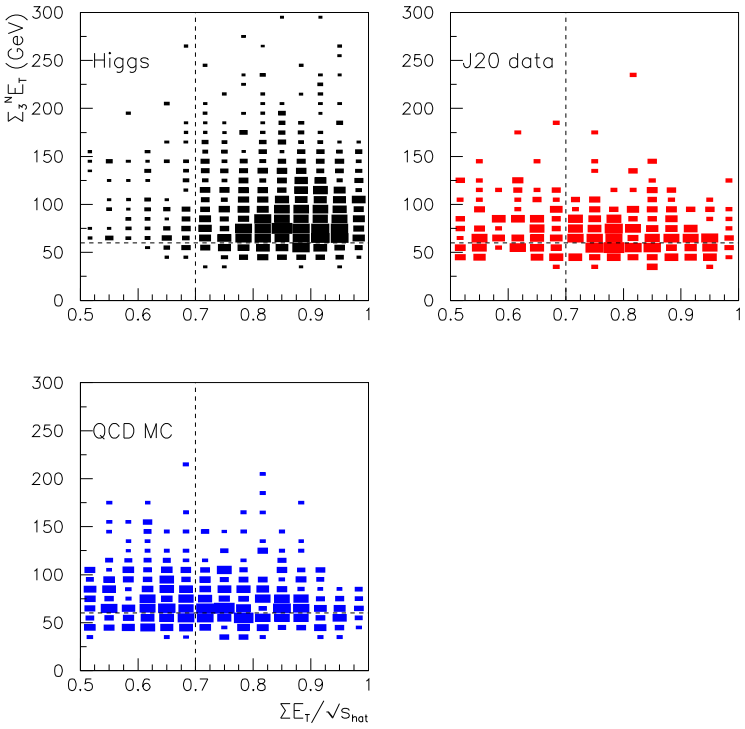

Figure 5.12: $\Sigma_3^N E_T$ *versus* $\Sigma E_T/\sqrt{\hat{s}}$ *for* $\mathrm{H^0V \to b\bar{b}q\bar{q}^{(\prime)}}$ *(*$M_\mathrm{H} = 120\,\mathrm{GeV}/c^2$*) and* JET20, QCD *background samples.*

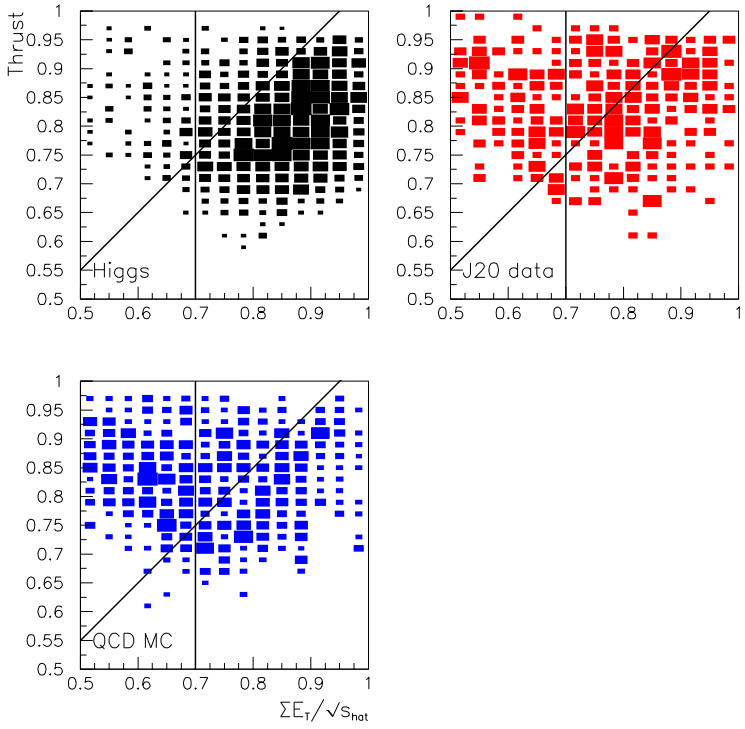

Figure 5.13: t_4 *versus* $\Sigma E_T/\sqrt{\hat{s}}$ *for* $\mathrm{H^0V \to b\bar{b}q\bar{q}^{(\prime)}}$ *(*$M_\mathrm{H} = 120\,\mathrm{GeV}/c^2$*) and* JET20, QCD *background samples.*

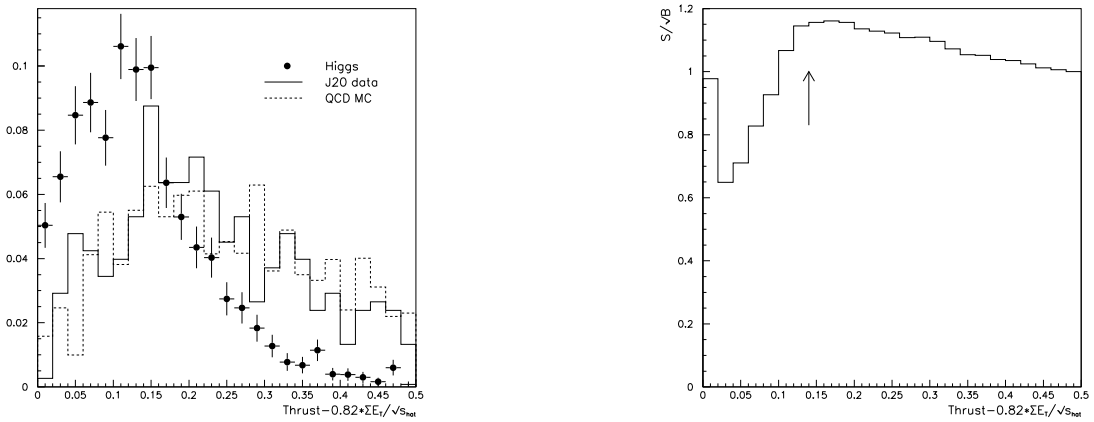

Figure 5.14: $t_4 - 0.82 \times \Sigma E_T/\sqrt{\hat{s}}$ *distribution for* $\mathrm{H^0V} \to \mathrm{b\overline{b}q\overline{q}^{(\prime)}}$ *(*$M_\mathrm{H} = 120\,\mathrm{GeV}/c^2$*) and background (*JET20*,* QCD*) samples (arbitrary normalization). Right:* $S/\sqrt{B}$ *ratio as a function of* $t_4 - 0.82 \times \Sigma E_T/\sqrt{\hat{s}}$ *computed with respect to* JET20 *background.*

Another characteristic of the production of two heavy objects is the centrality of the energy flux: the jets produced by the two bosons are mainly emitted in the transverse direction with respect to the beam line. This behaviour can be seen in the distribution of the variable $\Sigma E_T/\sqrt{\hat{s}}$ (see fig. 5.10), the transverse energy fraction, that provides an appreciable discrimination between the signal and the QCD background. Signal events populate the region closer to 1, while QCD events are characterized by a much smoother $\Sigma E_T/\sqrt{\hat{s}}$ distribution. Maximal significance is achieved for $\Sigma E_T/\sqrt{\hat{s}} \geqslant 0.7$, while the correlation between $\Sigma E_T/\sqrt{\hat{s}}$ and $\Sigma_3^N E_T$ is shown in fig. 5.12.

At this level background events have been selected with almost the same amount of "hardness" as the signal: separation can be improved by investigating variables that are more related to the spatial distribution of the decay products of the process. Among the considered variables, the best candidate turned out to be t_4 (fig. 5.11); however, its separation power becomes clear only when its correlation with $\Sigma E_T/\sqrt{\hat{s}}$ is considered. As visible in fig. 5.13, signal events populate the region where high values for both variables are observed, while background is more evenly distributed. The best separation can be achieved in terms of the variable $t_4 - 0.82 \times \Sigma E_T/\sqrt{\hat{s}}$, by requiring that $t_4 - 0.82 \times \Sigma E_T/\sqrt{\hat{s}} \leqslant 0.14$, as suggested by fig. 5.14.

Selection	$M_\mathrm{H} = 120$ [GeV/c^2] ($\sigma \times B.R. = 122$ fb)		**JET20**		**QCD**	S/B	$S/\sqrt{B}$
	ϵ (%)	exp'd evts	$\mathcal{A}$ (%)	exp'd evts ($\times 10^6$)	$\mathcal{A}$ (%)	($\times 10^{-5}$)	($\times 10^{-2}$)
Trigger	15.6	38.1	–	28.6	–	0.13	0.71
$N(jet)$, ΔR_{min}	12.3	30.1	54.1	15.5	60.7	0.194	0.765
$\Sigma E_T/\sqrt{\hat{s}} \geqslant 0.7$	11.2	27.5	33.0	9.44	30.2	0.291	0.895
$\Sigma_3^N E_T \geqslant 60$ GeV	9.8	23.9	21.4	6.12	20.2	0.391	0.966
$t_4 - 0.82\Sigma E_T/\sqrt{\hat{s}} \leqslant 0.14$	6.7	16.4	8.1	2.3	9.91	0.713	1.08

Table 5.3: *Summary of kinematical selection performance; efficiency (*ϵ*) is calculated with respect to generated signal (*$\mathrm{HV} \to \mathrm{b\overline{b}q\overline{q}^{(\prime)}}$*,* $M_\mathrm{H} = 120\,\mathrm{GeV}/c^2$*), while background acceptances on* JET20 *and* QCD *samples are computed with respect to trigger acceptance. For* S/B *and* $S/\sqrt{B}$ *estimations, the* JET20 *has been used. An integrated luminosity* $\mathcal{L} = 2\,\mathrm{fb}^{-1}$ *has been implicitly assumed.*

Table 5.3 reports the efficiency of the various steps of the selection on the signal events and the acceptance for the background samples; in both cases, the number of events refer to an integrated luminosity of $2\,\mathrm{fb}^{-1}$.

Note that no attempt to estimate the normalization of the Monte Carlo QCD source of background is made due to the large number of uncertainties in the predictions.

$\mathcal{L}_{int}$ [fb^{-1}]	Selection	Expected events				S/B ($\times 10^{-5}$)			$S/\sqrt{B}$ ($\times 10^{-2}$)		
		M_H [GeV/c^2]			JET20	M_H [GeV/c^2]			M_H [GeV/c^2]		
		110	120	130	($\times 10^6$)	110	120	130	110	120	130
2	$N(\mathrm{SVX})\geqslant 2$	6.2	5.2	3.4	0.028				3.7	3.3	2.0
	$N(\mathrm{SVX},\mathrm{SLT})\geqslant 2$	13	10	6.6	0.73				1.5	1.2	0.77
	$N(\mathrm{SVX},\mathrm{SLT})\geqslant 2$+KS [9]	7.7	5.9	3.8	0.07				2.9	2.2	1.4
10	$N(\mathrm{SVX})\geqslant 2$	31	26	17	0.14	22	19	12	8.3	6.9	4.5
	$N(\mathrm{SVX},\mathrm{SLT})\geqslant 2$	65	52	33	3.7	1.8	1.4	0.90	3.4	2.7	1.7
	$N(\mathrm{SVX},\mathrm{SLT})\geqslant 2$+KS [9]	39	30	19	0.35	11	8.4	5.4	6.6	5.1	3.2
30	$N(\mathrm{SVX})\geqslant 2$	93	78	51	0.42				14	12	7.9
	$N(\mathrm{SVX},\mathrm{SLT})\geqslant 2$	195	150	99	11				5.9	4.5	3.0
	$N(\mathrm{SVX},\mathrm{SLT})\geqslant 2$+KS [9]	116	89	57	1.1				11	8.5	5.4

Table 5.4: *Summary of b-tagging and kinematical selection predicted performances. Expected number of events refer to* $\mathrm{HV}\to \mathrm{b\bar{b}q\bar{q}}^{(\prime)}$ *signal and* JET20 *background samples. An integrated luminosity* $\mathcal{L}=2\,\mathrm{fb}^{-1}$ *has been implicitly assumed.*

5.5 Run II extrapolation

What follows is essentially a list of the possible source of improvement that may be expected for Run II. Most of the work for a quantitative estimate of these effects is clearly in progress and only real data will provide a final answer.

5.5.1 Detector acceptance

Detector upgrades will play a crucial rôle in achieving physics goals in Run II; the most significative improvements are:

- ◇ Enhanced muon identification due to CMX larger acceptance.
- ◇ New plug calorimeters will provide coverage up to $|\eta|\lesssim 3.6$; on one hand this corresponds to the possibility of exploiting the new Shower Maximum detector at trigger level, on the other the region $1<|\eta|<2$ will be accessible for electron identification provided that tracking is available in the same region.
- ◇ Apart from the increased z coverage of the interaction region, larger tracking efficiency can be obtained given the $|\eta|\leqslant 2$ acceptance of the silicon system. This will mean the possibility of exploiting its three-dimensional capabilities running standalone tracking procedures.

[9] KS stands for kinematical selection.

◇ The increase in tracking efficiency translates directly in enhanced SVX and SLT b-tagging capabilities. In particular, three-dimensional secondary vertex reconstruction will be possible, which, apart from a small increase in the efficiency ($\sim 10\%$), will mainly provide a more effective fake rejection.

5.5.2 Mass reconstruction

A further aspect that has to be considered at this point of the selection is the reconstruction of the decaying bosons; this is done by considering the invariant mass distributions of jet pairs. The problem of jet assignment is solved univocally only when two jets (exactly) have been tagged, in which case they are assigned to the scalar boson; conversely, all possible combinations need to be investigated. In any case, the resolution achievable on the reconstructed mass is an essential issue. For this reason several jet energy corrections have been developed [3, 4, 5, 6, 7]. The underlying philosophy is that, once jets have been corrected for all detector effects, a comparison with the signal Monte Carlo is still necessary in order to correct the measured jet energy back to the energy of the parton that originated it; furthermore, these corrections are process dependent. This is in particular true for b-jets since, for example, in the case of semileptonic decays, an amount of energy is lost through the presence of a neutrino and/or a muon.

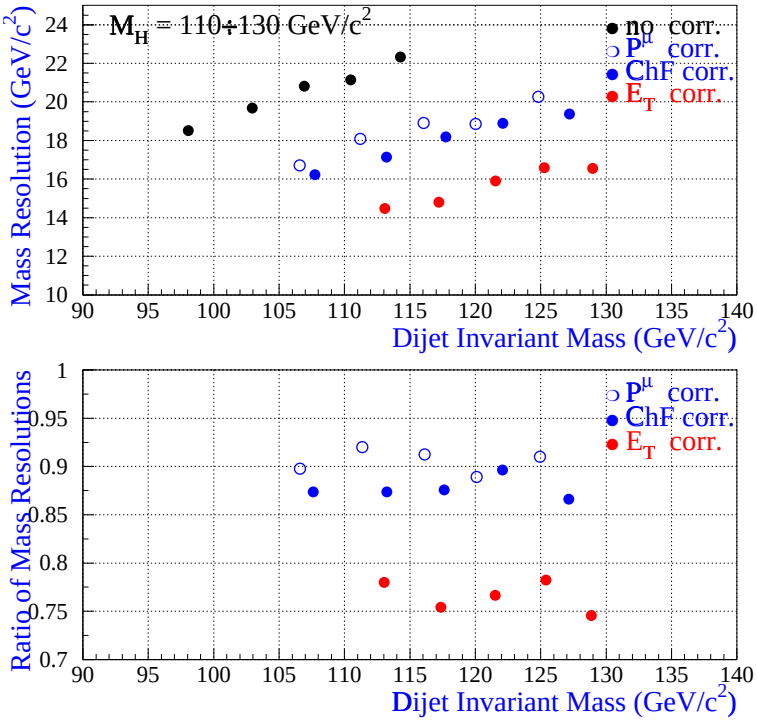

Figure 5.15: *Effects of specific* SLT*-multijet jet energy corrections on dijet invariant mass resolution as a function of mean reconstructed dijet mass; samples of* $H^0V \to b\bar{b}q\bar{q}^{(\prime)}$ *with* $M_H = 110, 115, 120, 125, 130\,\mathrm{GeV}/c^2$ *have been used.*

The overall improvement in mass resolution due to the jet energy corrections described in [7], specifically developed for samples collected by the SLT-multijet trigger, is shown in fig. 5.15. The effect of these corrections on the signal sample ($M_H = 120\,\mathrm{GeV}/c^2$) after the

trigger and N_{jet} requirements is shown for $N(\text{SVX,SLT}) \geqslant 2$ in fig. 5.16 (all combinations in jet assignment) and in fig. 5.17 (where correct assignment and combinatorial contributions are depicted). As expected, these corrections have almost no effect on the invariant mass shape of QCD $b\bar{b}$ background (see fig. 5.18).

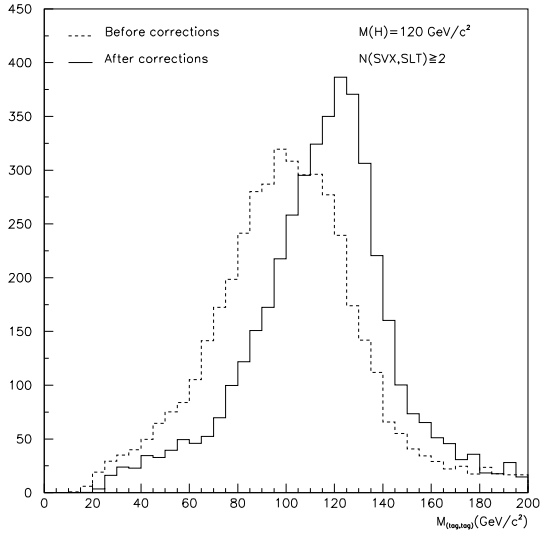

Figure 5.16: *Dijet invariant mass for* $H^0V \to b\bar{b}q\bar{q}^{(\prime)}$ *($M_H = 120\,\text{GeV}/c^2$) after trigger and N_{jet} requirements: N(SVX,SLT)$\geqslant 2$ before and after* SLT*-multijet specific corrections. All jet combinations have been plotted.*

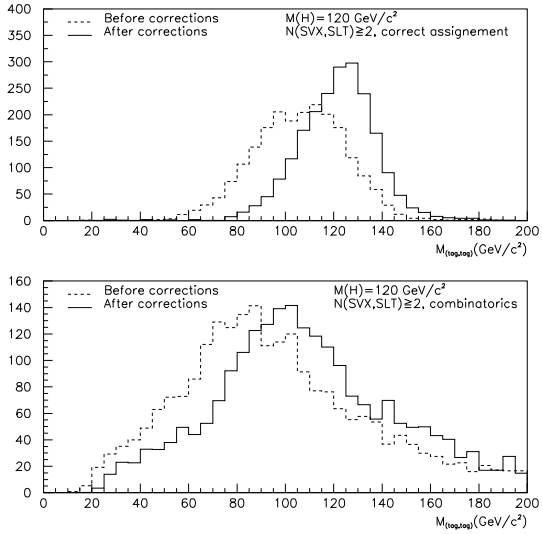

Figure 5.17: *Dijet invariant mass for* $H^0V \to b\bar{b}q\bar{q}^{(\prime)}$ *($M_H = 120\,\text{GeV}/c^2$) after trigger and N_{jet} requirements: N(SVX,SLT)$\geqslant 2$ before and after* SLT*-multijet specific corrections. Top: correct jet combinations. Bottom: all combinations with at least one wrong tag assignment.*

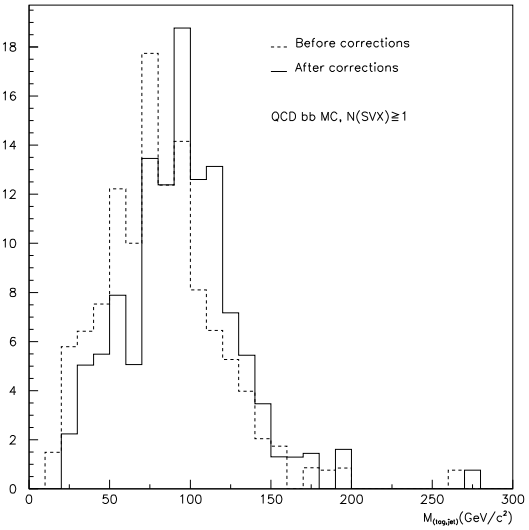

Figure 5.18: *Invariant mass for* QCD $b\bar{b}$ *Monte Carlo after trigger and* N_{jet} *requirements and with N(SVX)$\geqslant 1$ before (top) and after (bottom)* SLT*-multijet specific corrections. All combinations tag-jet have been plotted.*

5.5.3 Comparison with the Higgs Working Group results

Since Higgs physics is one of the main goals for Run II, a Higgs Working Group has been formed at Fermilab in order to study the possibilities offered by the upgraded CDF and D0 detectors [8]. In particular, two independent ways have been followed to obtain a prediction on the achievable limits in the Run II scenario for the multijet final state.

Extrapolation of the CDF Run I analysis. The results obtained in the Run I analysis [2], whose guidelines are reported in chapter 1, have been extrapolated to Run II conditions; the factors that are expected to give a significative contributions are the following:

- ◇ the expected increase in luminosity and total acceptance lead to improved limits by – at least – a factor $1/(\epsilon\sqrt{\mathcal{L}})$, where ϵ and $\mathcal{L}$ here represent the increased acceptance and luminosity factors with respect to Run I;
- ◇ augmented SVX II η coverage will result in a $\sim$80% enhancement in the double tagging efficiency if Run I central b-tagging intrinsic efficiency is assumed;
- ◇ a new trigger design, based upon looser (with respect to Run I) calorimetric requirements and on displaced tracks with large impact parameter (SVT), is expected to produce a factor-2 increase on the signal efficiency without compromising the total trigger rate.

All these factors have been estimated to produce a global factor-4 increase on signal; the predicted limit on $\sigma(p\overline{p}\to H^0V)\cdot\beta(H^0V\to b\overline{b}q\overline{q}^{(\prime)})$ is shown in fig. 5.19.

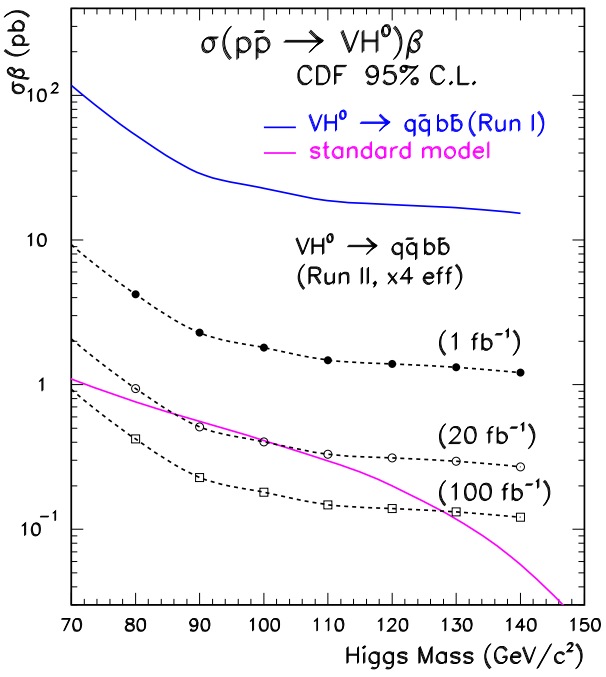

Figure 5.19: *Run II extrapolation of* CDF *Run I Higgs multijet analysis.*

Simulation. A parametrized detector simulation, representing an average situation between CDF and D0, has been used for computing efficiencies and acceptances expected in Run II. Topological and kinematical requirements have then been applied to the generated signal ($H^0V \to b\bar{b}q\bar{q}^{(\prime)}$) and QCD background samples; the results obtained at the end by this approach are reported in tab. 5.5.

M_H [GeV]	$S/\sqrt{B}$
110	0.07
120	0.05
130	0.03

Table 5.5: *Expected $S/\sqrt{B}$ ratio for the $H^0V \to b\bar{b}q\bar{q}^{(\prime)}$ final state at Run II based upon parametrized detector simulations for $\mathcal{L}_{int} = 1\,fb^{-1}$.*

An interesting conclusion that can be drawn from this procedure is concerned with mass resolution; according to the Higgs Working Group results, a factor-2 improvement in mass resolution corresponds to a factor-4 reduction in background, leading to a factor-2 increase in significance.

The simulation procedure, furthermore, performs a combination of the results obtained by considering all final states produced in the decay of the H^0V system and provide a limit on the overall sensitivity to a Higgs signal predicted for Run II (see fig.5.20).

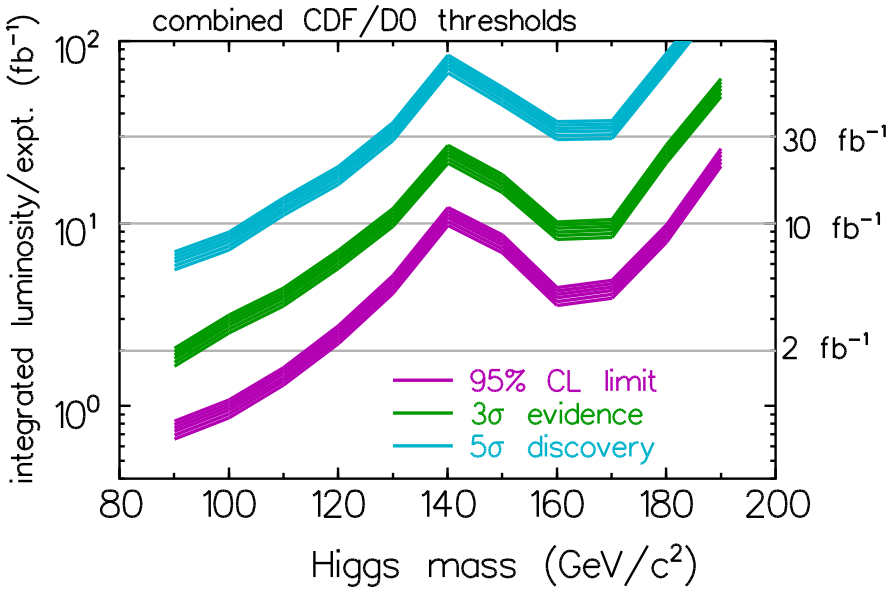

Figure 5.20: *Run II extrapolation from simulation.*

.

A comparison between the results shown in the previous section with what has been obtained by the Higgs Working Group, shows that the results obtained in the two cases (in terms of $S/\sqrt{B}$ ratios) are comparable; for $M_{\mathrm{H}} = 120\,\mathrm{GeV}/c^2$, the simulation predicts $S/\sqrt{B} = 0.05$ (which becomes $S/\sqrt{B} = 0.07$ for $\mathcal{L}_{int} = 2\,\mathrm{fb}^{-1}$), while the procedure described in this work finds $S/\sqrt{B} \simeq 0.03$. It must be noted, however, that this number refers to a situation that involves trigger, $N_{jet} \geqslant 4$ and $N(\mathrm{SVX}) \geqslant 2$ requirements only, while no use has been made of kinematical selection and mass reconstruction information; finally, significance could receive a further increase from specific jet corrections aimed at improving the Higgs mass resolution.

Bibliography

[1] F. Abe *et al.* (The CDF Collaboration), *Phys. Rev.* **D 50**, 2966 (1994).

[2] F. Abe *et al.* (The CDF Collaboration), *"Search for Higgs Bosons Produced in Association with* W *a Vector Boson in* $p\overline{p}$ *Collisions at* $\sqrt{s}=1.8\,\mathrm{TeV}$*"*, *Phys. Rev. Lett.* **81**, 5748 (1998).

[3] T. Dorigo, R. Ribon, M. Scardellato, D. Bisello, G. Busetto, L. Pescara, L. Stanco, *"Jet Corrections for Dijet Systems With a Muon"*, CDF internal note 4527, Mar 1998.

[4] J. Lys, *"Estimating b-Jet Energy in the Presence of a Soft Lepton"*, CDF internal note 5407, Aug 2000.

[5] A. Bocci, S. Kuhlmann, S. Lami, G. Latino, *"Last Results on the Energy Resolution using Calorimeter, Tracking, and Shower Max Information"*, CDF internal note 5416, Jun 2000.

[6] S. Lami, A. Bocci, S. Kuhlmann, G. Latino, *"Studies of Jet Energy Resolution"*, CDF internal note 5507, Nov 2000.

[7] L. Scodellaro, T. Dorigo, *"Jet Corrections for a Soft Lepton Tag-based Trigger"*, CDF internal note 5517, Dec 2000.

[8] M. Carena, J. S. Conway, H. E. Haber, J. D. Hobbs *et al.* (The Fermilab Higgs Working Group), *"Report of the Tevatron Higgs Working Group"*, HEP-PH/0010338, Oct 2000.

Conclusions

The design of a trigger aimed at selecting the fully hadronic final states emerging from a Higgs boson produced in association with a vector boson has been completed and the results that have been achieved were presented at the Trigger Working Group of CDF. The trigger is expected to be included in the trigger table for Run II and to operate from the beginning of the run, starting in spring 2001.

This tool is a combination of calorimetric and lepton primitives of the CDF three-level trigger architecture. Inadequate background rejection for electrons prevents the possibility of lepton tagging before Level 3; however, a Level 2 rate of 15.4 Hz for $\mathcal{L}_{inst} = 10^{32}\,\mathrm{cm}^{-2}\mathrm{s}^{-1}$, compatible with the trigger budget of 300 Hz, is achievable with only calorimetric requirements.

At Level 3, lepton identification is added to more stringent calorimetric requirements for a total signal efficiency of 16.2% for $M_{\mathrm{H}} = 120\,\mathrm{GeV}/c^2$. This efficiency increases with Higgs mass, varying by 10% for $\Delta M_{\mathrm{H}} = \pm 10\,\mathrm{GeV}/c^2$. The predicted event rate yielded by this trigger is 1.43 Hz for an instantaneous luminosity of $\mathcal{L}_{inst} = 10^{32}\,\mathrm{cm}^{-2}\mathrm{s}^{-1}$, which is fully compatible with the Level 3 bandwidth of 75 Hz.

Even though all rate estimates have been obtained on the basis of extrapolations to the Run II detector from real data collected during Run I, only the new data taking period will allow the evaluation of the actual performance of the proposed trigger.

Finally, it has been shown that the sample collected by this trigger can have a significant impact in the search for the Standard Model Higgs boson and, moreover, may be an excellent starting point for the search of supersymmetric signatures involving multijet and heavy flavour production.

List of Figures

List of Tables